



UNIVERSITÀ DEGLI STUDI DI NAPOLI “FEDERICO II”

FACOLTÀ DI INGEGNERIA

**Dottorato di ricerca in “Ingegneria Aerospaziale, Navale e
della Qualità” – XXIV Ciclo**

**Settore scientifico disciplinare ING-IND/05:
Impianti e Sistemi Aerospaziali**

3D space intersection features extraction from Synthetic Aperture Radar images

Ing. Stefano Serva

Tutor:
Ch.mo Prof. Ing. Antonio Moccia

Coordinatore:
Ch.mo Prof. Ing. Antonio Moccia

*“A mio Padre
che ne sarebbe felice ed orgoglioso”*

ABSTRACT

The main purpose of this Thesis is to develop new theoretical models in order to extend the capabilities of SAR images space intersection techniques to generate three dimensional information. Furthermore, the study aims at acquiring new knowledge on SAR image interpretation through the three dimensional comprehension of the scene.

The proposed methodologies allow to extend the known radargrammetric applications to vector data generation, exploiting SAR images acquired with every possible geometries. The considered geometries are points, circles, cylinders and lines. The study assesses the estimation accuracy of the features in terms of absolute and relative position and dimensions, analyzing the nowadays operational SAR sensors with a special focus on the national COSMO-SkyMed system.

The proposed approach is original as it does not require the direct matching between homologous points of different images, which is a necessary step for the classical radargrammetric techniques; points belonging to the same feature, circular or linear, recognized in different images, are matched through specific models in order to estimate the dimensions and the location of the feature itself. This approach is robust with respect to the variation of the viewing angle of the input images and allows to better exploit archive data, acquired with diverse viewing geometries.

The obtained results confirm the validity of the proposed theoretical approach and enable important applicative developments, especially in the Defence domain: (i) introducing original three dimensional measurement tools to support visual image interpretation; (ii) performing an advanced modelling of building counting only on SAR images; (iii) exploiting SAR images as a source for geospatial information and data; (iv) producing geospatial reference information, such as Ground Control Point, without any need for survey on the ground.

Keywords

Synthetic Aperture Radar, COSMO-SkyMed, Radargrammetry, Space Intersection, Building Features Extraction, Ground Control Point, Hyperboloid Space Intersection, pseudo Ground Control Point.

ACKNOWLEDGMENTS

At the end of this thesis work, I feel the need to thank all the people who supported me during this long period.

First of all, I want to thank General Sergio Bisegna who was the first to encourage me in doing the PhD and in suggesting me to analyze an argument of possible interest for the Italian Ministry of Defence. He showed, as usual, his “visionary” thought. On the other hand, I have to thank Colonel Giuseppe D’Amico, my current Director, for supporting me and making my effort become reality: without his unconditioned support, I would never have finished my work.

Obviously, the innovations and the new ideas I have introduced in this work are the results of a strong interaction with all my colleagues inside the Italian Ministry of Defence, especially inside the Centro Interforze Telerilevamento Satellitare. I would like to thank Lt. Col. Nardone for his unprecedented human support, Riccardo for his trust in my capabilities, Andrea, Alessandro and the other friends of the Academy for their overwhelming energy, Emanuele for being a stimulus for deeper and deeper studies, Roberto for introducing me to the world of Imagery Intelligence, and all the other colleagues for supporting me with the most open minded intentions.

A special thank to Prof. Antonio Moccia: he was a constant point of reference for my activity, he was able to support me in difficult moments and, on the other hand, to take a critical look at my studies and proposals. I have a deep debt of gratitude to him.

Having done my effort mainly outside my everyday work, I was obliged to ask a huge sacrifice to my friends and my family, my trio of wonders, my parents-in-law Franca and Aldo, my grandmother Egista, my brother Simone, my mother Anna Rita and especially to my beloved wife Silvia. It was hard to renounce to the pleasure of staying with them but it was necessary to carry on my research and now, at the very end of my work, I can only say to them that they deserve all my gratitude. To my wife Silvia, who is my never-ending source of inspiration, my “Muse”, I can only say that I love her so much!

INDEX

ABSTRACT	3
ACKNOWLEDGMENTS	4
INDEX.....	5
List of Acronyms	8
INTRODUCTION	10
Aim of the Study	11
State-of-art techniques for 3D information extraction	12
Original contribution of this work.....	13
Organization of the work.....	14
CHAPTER 1 - Operative scenario and Inputs	15
1.1 Interactions with operative users	15
1.2 Example of imagery interpretation	15
1.3 Survey of commercial applications and software	17
1.4 Needs for Imagery Interpretation.....	18
CHAPTER 2 - SAR Systems and Data	19
2.1 Remote sensing	19
2.1.1 Active Remote sensing	19
2.2 Synthetic Aperture Radar sensors	20
2.2.1 Principles	20
2.2.2 Geometry	30
2.2.3 RADAR image properties	37
2.2.4 Scattering effects	41
2.3 COSMO-SkyMed	45
2.3.1 The System	45
2.3.2 Products	47
2.3.3 Applications and exploitation.....	50
2.3.4 The future: COSMO-SkyMed Second Generation.....	54
CHAPTER 3 - Theory and Implementation	57
3.1 3D Information from earth observation data: Scenario Analysis	57
3.2 Intersection of spaceborne stereo SAR data	58
3.2.1 Range-Doppler approach.....	59

INDEX

3.2.2	Image to ground coordinates transformation.....	59
3.2.3	Rigorous Stereo Method.....	60
3.2.4	Generalized N-images stereo model.....	61
3.2.5	Error Budget of the target position	63
3.3	Multi-aspect Feature based Space Intersection.....	70
3.3.1	Multi-aspect Feature based Space Intersection for Circular features	72
3.3.2	Multi-aspect Feature based Space intersection for Linear features: the “Hyperboloid Space Intersection”	96
3.4	Automation of the 3D features extraction based on Multi-aspect Feature based Space intersection.....	108
3.4.1	A scenario analysis of the state of art techniques for automatic 3D feature extraction	108
3.4.2	An implementation scheme for automatic 3D features extraction	108
CHAPTER 4 - Case studies and Experimental Results.....		111
4.1	“Venice” Case Study	111
4.1.1	Aim of the case study	111
4.1.2	Test site and Dataset.....	111
4.1.3	Phenomenology: confirmation of the proposed model with medium geometric resolution images	113
4.1.4	Phenomenology: confirmation of the proposed model with high geometric resolution images	117
4.1.5	The local terrain influence on triple bounce location	118
4.1.6	Discussion & possible improvements.....	119
4.2	“Naples and Solfatara” Case Study	120
4.2.1	Aim of the case study	120
4.2.2	Test site and Dataset.....	120
4.2.3	Results of multi-aspect space intersection.....	124
4.2.4	Discussion & possible improvements.....	129
4.3	“Palazzo reale” Case Study.....	131
4.3.1	Aim of the case study	131
4.3.2	Test site and Dataset.....	131
4.3.3	Results of Hyperboloid space intersection	132
4.3.4	Discussion and possible improvement	134
4.4	“Basilicata” Case Study	135

INDEX

4.4.1	Aim of the case study	135
4.4.2	Test site and Dataset	135
4.4.3	Results of Hyperboloid space intersection	137
4.4.4	Discussion and possible improvements	141
4.5	“Matera”Case Study	142
4.5.1	Aim of the case study	142
4.5.2	Test site and Dataset	142
4.5.3	Results of the automatic 3D feature extraction technique based on multiaspect space intersection	143
4.5.4	Discussion & possible improvements.....	146
CHAPTER 5 - Practical Applications and Lessons Learned.....		147
5.1	Practical application of the achieved results	147
5.1.1	Supporting image interpretation	147
5.1.2	Creating 3D Geospatial Information	153
5.1.3	Validating open source data	156
5.1.4	Monitoring temporal evolution of man-made activities	157
5.2	Lessons learned.....	158
5.3	Needs for Next Generation systems.....	160
5.3.1	Going towards next generation systems	160
5.3.2	Near future generation systems	160
CONCLUSIONS		161
BIBLIOGRAPHY		164

LIST OF ACRONYMS

AoI	Area of Interest
ASI	Agenzia Spaziale Italiana (Italian Space Agency)
CFAR	Constant False Alarm Rate
CCD	Charge-Coupled Devices
CITS	Centro Interforze Telerilevamento Satellitare (Joint Centre for Satellite Remote Sensing)
COSMO-SkyMed	COntstellatIon of small Satellites for Mediterranean basin Observation
CP	Control Point
CSG	COSMO-SkyMed Second Generation
CSK	Abbreviation of COSMO-SkyMed
DEM	Digital Elevation Model
DSM	Digital Surface Model
DTED	Digital Terrain Elevation Data
ECEF	Earth Centred Earth Fixed
ERS	European Radar Satellite
ESA	European Space Agency
FFT	Fast Fourier Transform
GCP	Ground Control Point
GEOINT	Geospatial Intelligence
GTC	Ground Terrain Corrected
HDF	Hierarchical Data Format
HO	Hyperboloid Oriented

List of Acronyms

IMINT	Imagery Intelligence
LA	Left looking – Ascending orbit
LD	Left looking – Descending orbit
LIDAR	Light Detection And Ranging
MASINT	Measurement and Signature Intelligence
MoD	Ministry of Defence
NGA	National Geospatial-Intelligence Agency
pGCP	pseudo Ground Control Point
PPB	Probabilistic Patch Based
PRF	Pulse Repetition Frequency
RADAR	RAdio Detection And Ranging
RA	Right looking – Ascending orbit
RAR	Real Aperture Radar
RD	Right looking – Descending orbit
RoI	Region of Interest
RPC	Rooted Polynomial Coefficient
SAR	Synthetic Aperture Radar
WGS 84	World Geodetic System 1984

INTRODUCTION

The availability of high resolution SAR images allows the operational exploitation of radar systems, including the national COSMO-SkyMed one, both for military applications and civil protection.

The research, aiming at enhancing the productivity of the SAR Imagery Intelligence (IMINT), is mainly devoted to enhance the techniques capable to support the extraction of information from SAR images. This goal can be achieved by studying at the same time the geometric and radiometric content of the images, as well as the possible ways to limit and overcome the classical SAR drawbacks, such as speckle noise, layover and foreshortening. These needs become even more demanding in man-made scenarios, where the presence of complex geometries and the cumulative interference of the aforementioned effects pose more difficult tasks to Imagery Intelligence analysts and to those who are trying to develop new applications to exploit the data in an automated or semi-automated way.

Fig. 1 shows the explosion of interest in the field during the last 5 years; all these operational programs are now facing the need to translate technical capabilities and opportunities into operative applications: I will conduct this study trying to explain, case by case, the applicative advantages and the possible follow on.

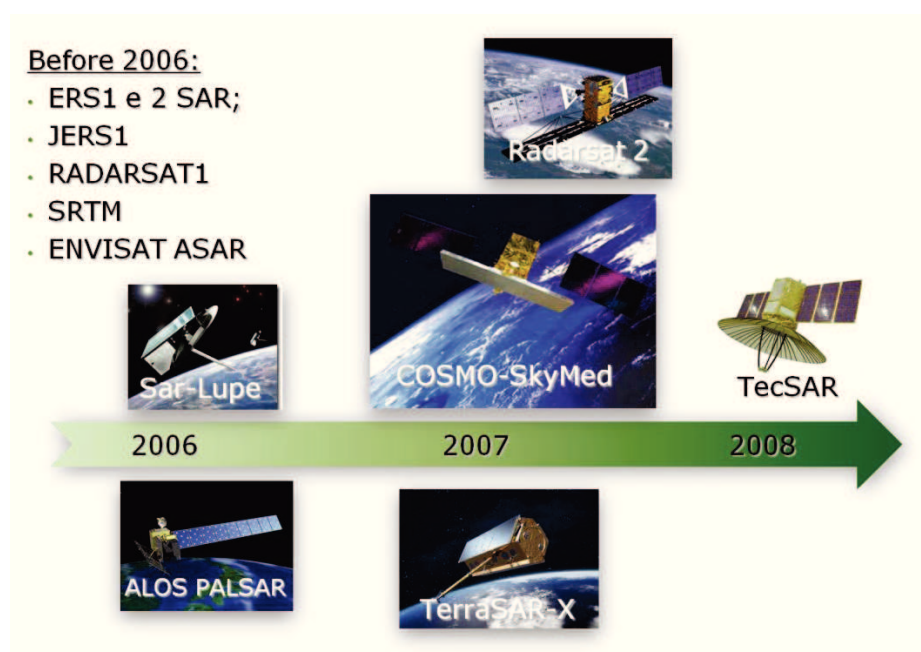


Fig. 1 – The impressive evolution of the SAR remote sensing in the last years

INTRODUCTION

This thesis has been developed working at CITS - *Centro Interforze Telerilevamento Satellitare* (standing for Joint Centre for Satellite Remote Sensing), the national User Ground Segment of both COSMO-SkyMed and Hélios systems. During this period I have worked inside the Centre previously as Chief of COSMO-SkyMed Technical Section and nowadays as Chief of Study Section. The stimulus and motivation of the activities carried on inside the Centre have helped me in defining the research topics and finding the applicative domains of interest.

AIM OF THE STUDY

The aim of this PhD thesis is to investigate the possible techniques for enhancing the extraction of 3D geospatial information from Synthetic Aperture Radar images; this would be useful to allow the interpretation of the images themselves.

For the observer, while the interpretation of electro-optical images is closer to the experience of the outside reality, the interpretation of a SAR image strongly rely on his capability to understand the geometry of the acquisition. Therefore, every single technique allowing the extraction of 3D features and information from the images significantly improves the capability to understand the image itself.

As summarized in Fig. 2, the interpretation of SAR images strongly depends on:

- data preparation, all the pre-processing activities necessary to adapt the visualization of the image for human interpretation and/or processing tasks useful to extract some higher level products from the input image (e.g. coherence map, coherent change detection, etc.);
- data fusion, the correlation of the SAR image with an optical one, which enables a better understanding of the SAR sensing geometry as well as of the observed target geometry and shape;
- geospatial information, all the raster and vector data representing the geographical information of the target environment (e.g. road network, borders, agricultural destination of fields, Digital Elevation Model of the earth surface, etc.).

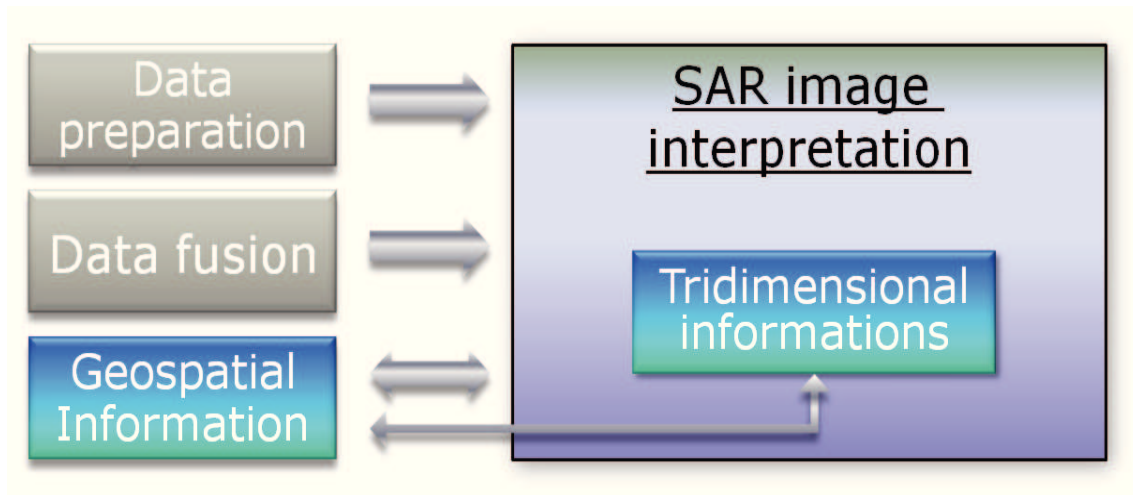


Fig. 2 – Preparing and understanding SAR image

In SAR image interpretation, understanding the geometry of the acquisition is the most complex task: the most useful approach is trying to reconstruct the backscattering phenomenon in order to “ray-trace” the three dimensional path of the electromagnetic radiation. For this reason, geospatial information such as Ground Control Point (GCP) or Digital Surface Model (DSM) could give an immediate support in extracting the basic 3D information and features from an image, allowing a better understanding and interpretation of the image itself.

In the following examples, taken from the real world, I will try to highlight the importance of understanding SAR images in their geometry before trying to interpret them, especially in the case of complex scenarios, such as highly man-made areas.

STATE-OF-ART TECHNIQUES FOR 3D INFORMATION EXTRACTION

The extraction of 3D information from SAR images has been deeply studied in the last decades. Toutin and Gray, (1), give a complete review of the various state-of-art techniques and highlight the main features and perspectives of Interferometry, exploiting the signal phase and Radargrammetry, based on the pixel magnitude.

Radargrammetry, (2), is the radar sensor technique equivalent to the optical stereo case. The sensor configuration could be generally referred to as “same-side” and “opposite-side”. Same side means that the images have been acquired from the same aspect under different viewing angles. On the other hand, opposite-side are images acquired from opposite viewing aspects. If the second configuration is characterized by a major disparity, advantageous for height estimation as it gives a better accuracy in the

INTRODUCTION

estimation, the similarity of images decreases while problems in the matching of image patches increase (3). A good compromise would be acquiring same-side stereo images with a large viewing angle difference, (4). Other studies have focused on the possibility to reconstruct 3D building shape from multi-aspect SAR images, (5).

The aforementioned methods exhibit interesting areas of possible improvement, especially regarding the possibility to combine them with features extraction techniques, usually finalized to 2D information extraction.

ORIGINAL CONTRIBUTION OF THIS WORK

In this work I have tried to fulfil at the same time two different needs:

- introducing new models and tools to interpret the three dimensional information of a SAR image;
- linking the new models to the applicative domains, trying to keep in mind and answer the everyday needs I face in my activity at CITS.

The theoretical innovations of my work inside the SAR remote sensing field are:

- new multi-aspect “feature based” space intersection methods, allowing to fuse information that come from several different views of a target through its geometric model (characterized by shapes and virtual points, e.g. a circle and its central point for a cylindrical building). The innovation is the modification of the space intersection problem by means of a geometric model of the target;
- a new linear space intersection method, called “Hyperboloid space intersection” allowing to recognize linear features in a set of images (without any need to recognize homologous points) and to extract their 3D coordinates solving an innovative space intersection problem based on hyperboloids;
- a new concept of pseudo Ground Control Point (pGCP), generated by means of multi-aspect “feature based” space intersection techniques. These points are no more only related to real features (such as a corner reflector or a dihedral feature) but they can be virtual or mathematical points (such as the centre of a circular pole or building).

A complete end-to-end integration of the proposed technique is also introduced, as well as the assessment of the accuracies obtained, by working with the COSMO-SkyMed system.

ORGANIZATION OF THE WORK

This work is organized into 5 chapters:

- CHAPTER 1 gives a synthetic overview of the imagery analysts' work, trying to explain the major needs in the field of SAR interpretation;
- CHAPTER 2 introduces the general concepts regarding the SAR remote sensing, with a specific focus on the SAR effects which have an impact on the interpretability of the images and on the scattering behaviour of the electromagnetic radiation for the wavelength of interest;
- CHAPTER 3 presents the main theoretical innovation introduced by this thesis work. The proposed mathematical methods are also explained in their possible application chain;
- CHAPTER 4 shows the results of the analyzed test cases, for which a set of not classified COSMO-SkyMed images was exploited working at *Centro Interforze Telerilevamento Satellitare*;
- CHAPTER 5 illustrates possible practical applications of the developed techniques and models, trying to draw at the same time a lessons learned and new requirements to be implemented into the next generations of COSMO-SkyMed SAR satellites.

CHAPTER 1 - OPERATIVE SCENARIO AND INPUTS

1.1 INTERACTIONS WITH OPERATIVE USERS

Having the possibility, as an Air Force Officer working in the field of the military satellite remote sensing, to interact with many Imagery Analysts and operative users, I was able to deeply understand the difficulties and potentialities of the SAR image interpretation process. This is the reason why I will give room, inside this thesis work, to the inputs I received from these actors.

Imagery analysts look at SAR algorithms development with an extremely high interest, mainly for the following reasons/needs:

- the importance of data preparation, especially regarding the speckle filtering and the visualization enhancement;
- the need for data fusion with optical images, used as reference data/information to understand the radar image; usually, it is not necessary to have contemporary SAR/optical data, even old optical data can be exploited;
- the challenges of urban environment interpretation, because of the presence and coexistence of typical radar phenomena such as layover, foreshortening, double and triple bounce reflections;
- the SAR value added products, usually created by exploiting the major SAR advantages, as the phase, the precise georeferencing or the capability to highlight changes (i.e. change detection).

1.2 EXAMPLE OF IMAGERY INTERPRETATION

In this paragraph an elementary imagery interpretation task is described. First of all, the analyst has to understand the main destination and areas of the target. Therefore, a geographical understanding of the target is provided. Then, depending on the task (for example to answer a specific question or to update the knowledge on a specific area of interest), the area is divided into different Regions of Interest (RoI), univocally identified with a specific nomenclature. Fig. 3 shows an example of area classification within a military harbour.

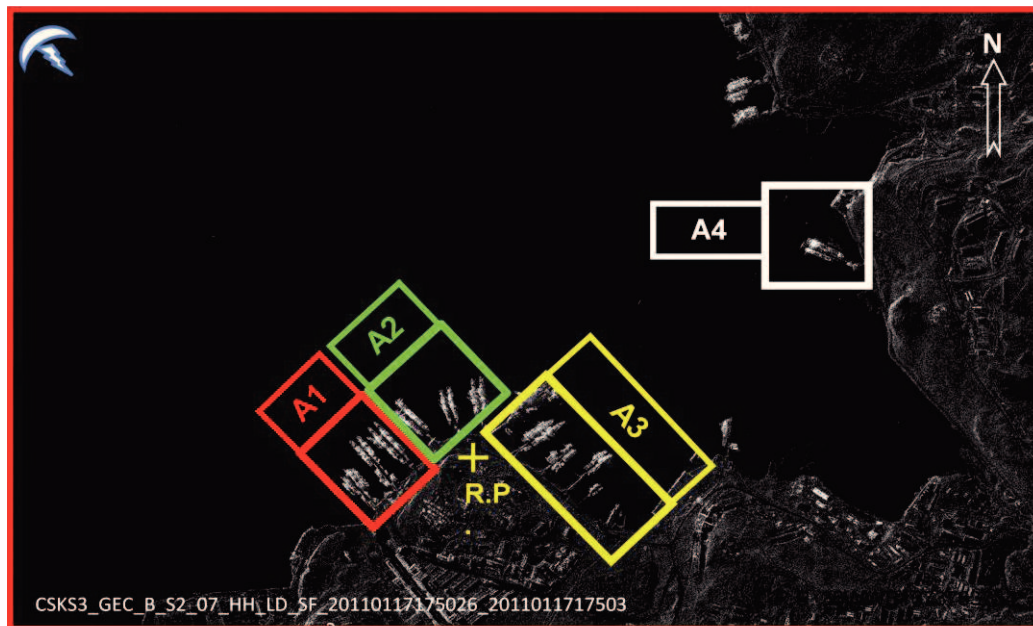


Fig. 3 – The results of the analysis of an Imagery Analyst (part 1)

If the question to answer is the identification of the vessels inside the harbour, the analyst exploits all the information he can derive from the image (e.g. the length of the vessel, the shape, the position of the mast with respect to the prow) in order to select the most appropriate item within a set of possible alternatives.

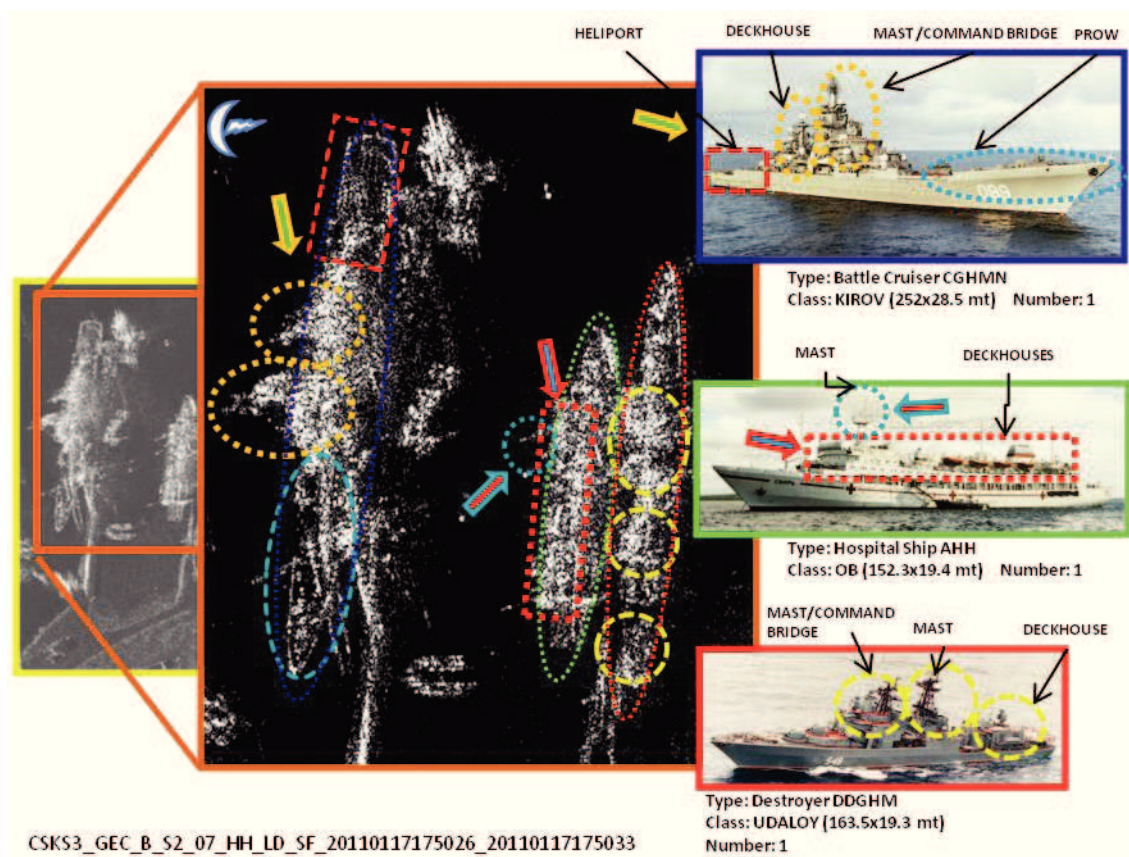


Fig. 4 – The results of the analysis of an Imagery Analyst (part 2)

Obviously, if the requests are more challenging, if they are focused on the understanding of complex geometries, the analysis could be really difficult and require advanced supporting instruments and tools.

As already mentioned, the data fusion with an optical image meaningfully improves the ability to interpret the SAR image. Fig. 5 shows the advantage of the data fusion: while the optical image on the right gives a good general understanding of the scene, in the radar image the electromagnetic radiation penetrates the sun shelters' light coverage, giving an idea of the objects parked inside, showed by the picture taken on the ground.

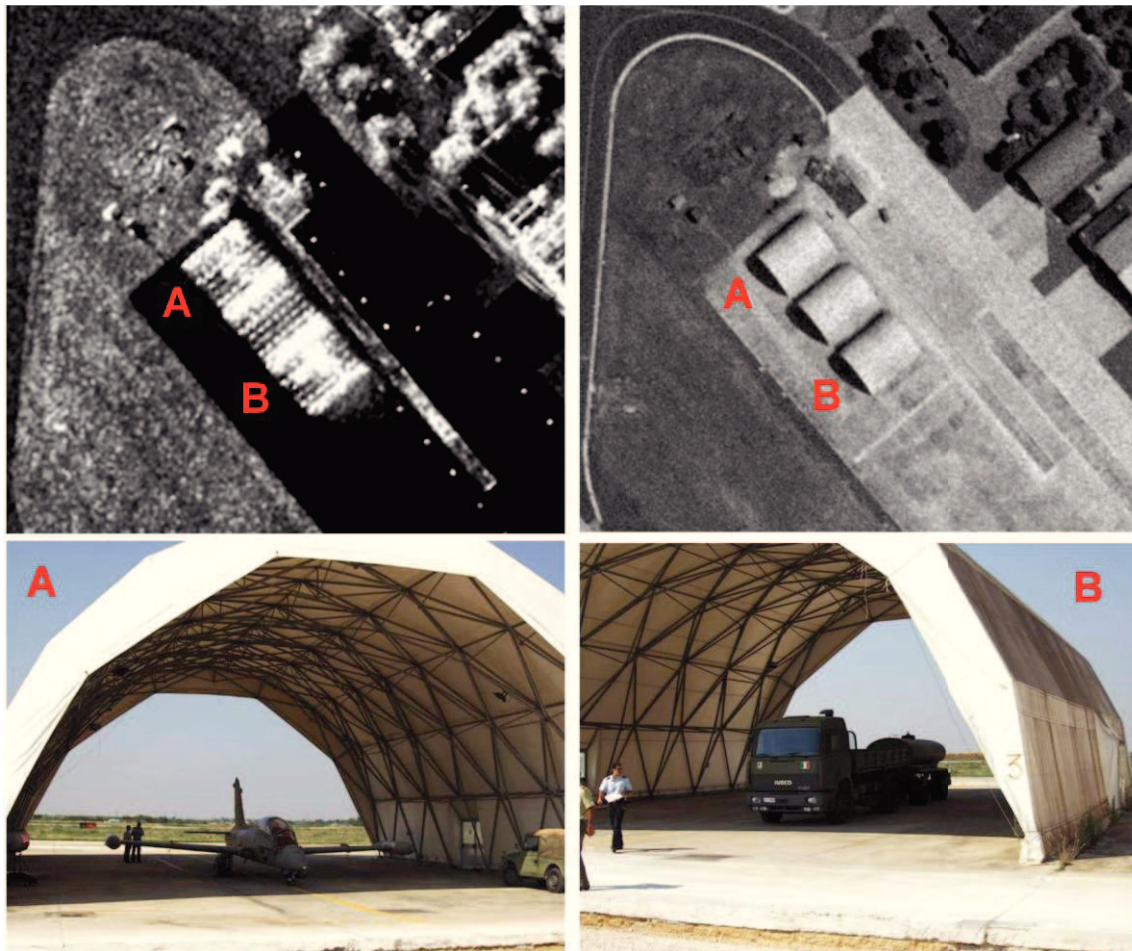


Fig. 5 – SAR/optical data fusion. Different appearance of the sun shelters in the SAR and optical sources

1.3 SURVEY OF COMMERCIAL APPLICATIONS AND SOFTWARE

The major software for imagery interpretation give a set of tools to interpret SAR images for Imagery Intelligence applications. For this thesis work I have analyzed the tools available in these software, with a special focus on ERDAS Radar Mapping Suite

(6), ENVI & SARscape (7), SOCET GXP (8); NEST (9), GEOINT SAR Toolbox (10) and Gamma (11):

- geometric correction and geocoding;
- triangulation;
- interferometric processing for elevation model generation and displacement analysis;
- persistent scatters extraction for displacement analysis and generation of cloud of precise 3D points;
- radargrammetric application for digital elevation model generation;
- change detection, “coherent change detection” and “multitemporal coherence combination “for time evolution monitoring”.

1.4 NEEDS FOR IMAGERY INTERPRETATION

If the previous paragraph shows mature and available SAR applications, a lot of room remains for further developments. In fact, referring to the available COTS software, a lot of capabilities can be further enhanced:

- automation of change detection by means of the definition of regions of interest (RoI). This need requires really high geolocation accuracy or the capability to recognize tie points or features within images acquired with every possible viewing geometries (the classical corner reflector-like tie point is not enough for this need, as I will explain in paragraph 3.3.1.5);
- improvement of 3D targets understanding, interpretation and reconstruction, exploiting full resolution or super-resolution images, without any need to degrade the geometric resolution (many radargrammetric applications require the degradation or they work well with medium resolution data) and with the capability to extract vectors instead of raster;
- capability to extract complex features instead of “clouds of points” (clouds of 3D points are one of the possible outputs of Persistent Scatterers techniques), if possible directly correlated with the image, in order to enhance the interpretability of the image itself.

CHAPTER 2 - SAR SYSTEMS AND DATA

2.1 REMOTE SENSING

A common definition of remote sensing is “the science and art of obtaining useful information about an object, area or phenomenon through the analysis of data acquired by a device that is not in contact with the object, area, or phenomenon under investigation”, (12). In the following, a synthesis of the background theory for SAR remote sensing is provided.

2.1.1 ACTIVE REMOTE SENSING

The sensors for remote sensing could be “passive” or “active”. Passive sensors detect the natural radiation which is emitted or reflected by the object or the observed area . Reflected sunlight is the most common source of radiation measured by passive sensors. Examples of passive remote sensors include film photography, infrared, Charge-Coupled Devices (CCD) and radiometers. Active sensors, on the other hand, emit energy in order to illuminate objects and areas and then detect and measure the radiation reflected or backscattered from the target. RADAR (RAdio Detection And Ranging) and LiDAR (Light Detection And Ranging) are examples of active sensors. They measure the time delay between emission and return and/or the signal intensity, establishing the location and the backscattering behaviour of the target.

Radar is an object-detection system which uses electromagnetic waves, with wavelength of radio waves, in order to determine the range, altitude, direction, or speed of both moving and fixed objects. The radar antenna transmits pulses of radio waves or microwaves which bounce off any object in their path. The object backscatters a tiny part of the wave's energy to a dish or antenna which is usually located at the same side of the transmitter. Synthetic Aperture Radar (SAR) is a form of radar with the peculiar feature to use relative motion between an antenna and its target to create an image, providing time distinctive long-term coherent-signal variations that are exploited to obtain the finer spatial resolution with conventional beam-scanning means. It originated as an advanced form of side-looking airborne radar.

SAR is usually implemented by mounting, on a moving platform such as an aircraft or spacecraft, a single beam-forming antenna from which a target scene is repeatedly illuminated with pulses of radio waves at wavelengths anywhere, from a meter down to millimetres. The many echo waveforms received successively at the different antenna positions are coherently detected and stored and then post-processed together to resolve elements in an image of the target region.

2.2 SYNTHETIC APERTURE RADAR SENSORS

2.2.1 *PRINCIPLES*

As already said, the Synthetic-Aperture Radar is “a coherent radar system generating a narrow cross range impulse response by signal processing (integrating) the amplitude and phase of the received signal over an angular rotation of the radar line of sight with respect to the object (target). Due to the change in line-of-sight direction, a synthetic aperture is produced by the signal processing that has the effect of a longer antenna”. The synthetic array is formed by pointing a real antenna (whose maximum size is restricted by the physical dimensions of the carrier vehicle) broadside to the direction of forward motion of the platform, and coherently processing (summing) the returns from successive pulses. The points at which successive pulses are transmitted can be thought of as the antenna elements of the synthetic array. Synthetic aperture radars, installed aboard aircrafts and space vehicles, are capable of achieving very high angular resolutions, which, when combined with the high range resolution achievable through pulse compression techniques, make the SAR a nearly ideal all-weather terrain or sea surface mapping system. Synthetic Aperture is a method used to improve radar resolution in azimuth or, more precisely, in the direction of the velocity vector of the platform. This resolution can be compared with the one that could be obtained by a very large physical antenna.

In the following the classical theory of Synthetic Aperture Radar, as explained in (13), is summarized.

2.2.1.1 Real Aperture Radar (RAR) system and resolutions

In order to well describe SAR principles, we start to analyze Real Aperture Radar (RAR) remote sensing systems. RADAR systems are designed to measure the strength and round-trip time of the microwave signals emitted by an antenna and reflected on a distant surface or object. A radar antenna allows to transmit and receive a signal at different wavelengths, power and polarization. Echoes are converted to digital data and

passed to a data recorder for further processing and then displayed as an image. This means that the active operating mode allows remote sensing systems to be independent from external sources (i.e. sunlight) and to reduce the impact of weather effect on the obtained images (day and night and all-weather imaging). Operating in the microwaves region allows to penetrate not only clouds, but also soil and vegetation: scientific research can be extended to the study of geometric and dielectric properties of surfaces (soil or ocean), not achievable by means of optical images. The information acquired by satellites have many applications and are used in various sectors, such as the optimization of the production of natural resources, the study of environment, the prediction and monitoring of natural disasters, etc. Remote sensing represents a very effective tool, useful to monitor and keep a check on natural phenomena, because it offers a complete real-time description: for example, it allows to plan and get off the civil protection services. A fundamental parameter of the radar system quality is the geometric resolution, which expresses the ability of the system to distinguish two near objects as separate entities; it is deeply linked to the frequency band and the antenna characteristics. The main active sensor limit is the poor resolution achievable with the operating wavelength of the basic configuration, usually referred to as Real Aperture Radar (RAR): if the sensor is located at a distance of 800 km and the operating frequency is 1 Ghz, we should use a more 10 km long antenna to achieve a 10 meter resolution. The configuration of any imaging radar system is shown in Fig. 6. The antenna is typically mounted on aircraft or satellite platforms at the altitude h and flies at the speed v along the flight direction. The cylindrical coordinates (x, r, γ) are respectively referred to as azimuth, slant range and look angle. This is the coordinates system that naturally matches side-looking radar operation: this configuration is necessary to eliminate right-left ambiguities from two symmetric equidistant points. The platform trajectory, assumed as a straight line, is coincident whit the azimuth axis x ; the antenna is oriented along the range axis r , pointing toward the scene, finally γ is the polar angle in the plane orthogonal to x - and containing the r -axis.

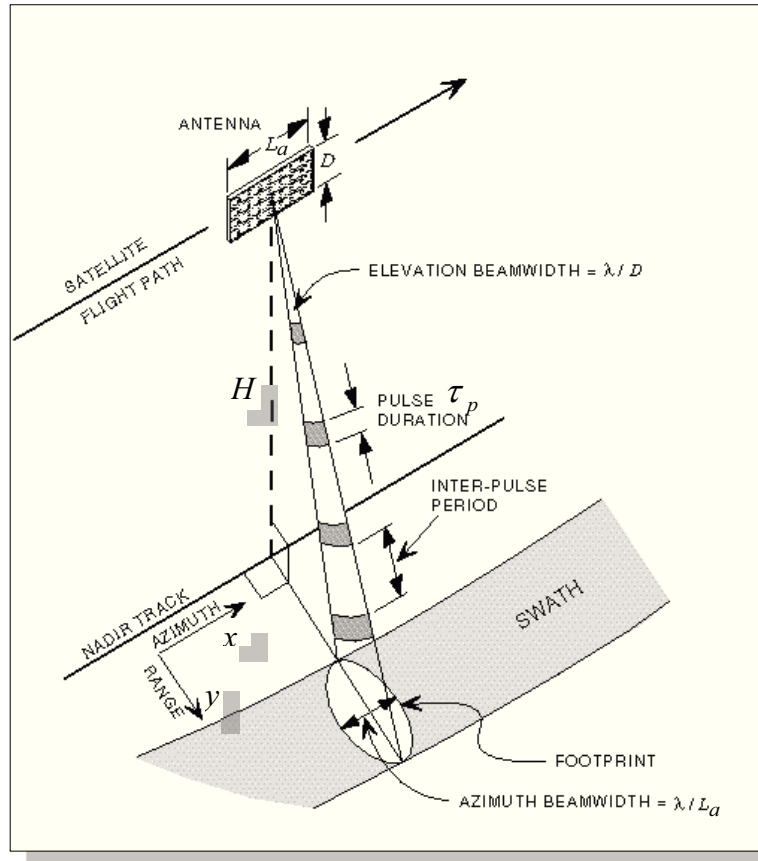


Fig. 6 – Radar imaging geometry

With respect to the flight platform path, the radar antenna illuminates a region of the surface, limited in the across track (*range*), but not in the along-track (*azimuth*) direction. All the points, which belong to the illuminated region and consequently contribute to the backscattered signal, constitute the footprint, which is ellipse-shaped. The sensor transmits and receives impulse with a frequency PRF (Pulse Repetition Frequency) to cover continuously the region of interest. Its inverse, $T = \frac{1}{PRF}$, represents the delay between two following impulses in order to avoid their backscattered echoes to overlap. An impulse can be transmitted from the position vT only if the time $\tau = \frac{2r}{c}$ passed between two pulses, where the factor 2 indicates the round-trip time and c is the speed of propagation. To describe general principles and the limits of the traditional radar imagery, we will try to analyze the geometric resolution, which is the ability of the system to localize nearby objects. To be more precise, the resolution length is the minimum spacing between two objects which are detected as separate entities and therefore resolved.

Scientific literature refers to a resolution cell in two dimensions as the rectangle whose sides are the azimuth (Δz) and the range (Δr) resolution.

The geometric configuration considered to calculate range resolution is shown in Fig. 7.

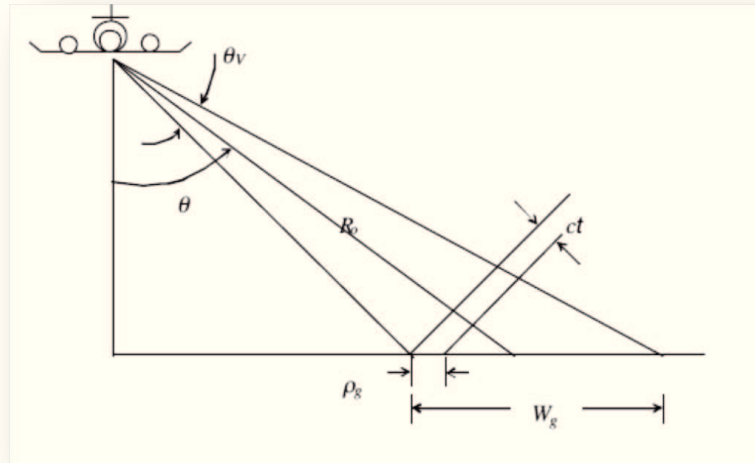


Fig. 7 – Geometry in the range plane

In order to estimate the minimum distance between two objects resolved by the system, it is convenient to consider two points (two point objects) A and B in the illuminated region: r_A and r_B are the respective range distances (radar-object distances). If the transmitted signal is an impulse, whose length is τ , the objects are resolved if the backscattered echoes (whose length is still τ , because of the hypothesis of point objects) do not overlap. If $r_A < r_B$, the signals backscattered by the points A and B are received respectively after a time $\frac{2r_A}{c}$ and $\frac{2r_B}{c}$. The hypothesis of considering backscattered signals separated can be translated in formula such as:

$$\frac{2r_A}{c} + \tau \leq \frac{2r_B}{c} \quad \text{Eq. 1}$$

So, the smallest distance Δr that the system can evaluate, i.e. the range resolution, is:

$$\Delta r = |r_B - r_A| = \frac{c\tau}{2} \quad \text{Eq. 2}$$

As shown in Fig. 8, the distance between two objects on the surface is the projection on the horizontal axis of the range resolution and it is called ground range:

$$X_r = \frac{\Delta r}{\sin(\theta)} = \frac{c\tau}{2\sin(\theta)} \quad \text{Eq. 3}$$

that is a function of θ , equal to the angle of incidence, from θ min to θ max.

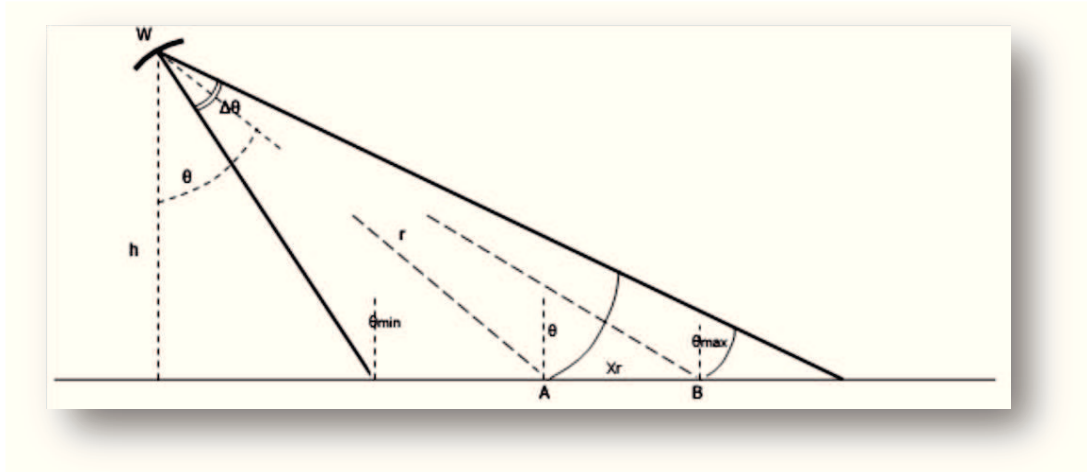


Fig. 8 – Geometry in the range plane, ground range

From Eq. 2 and Eq. 3 it is clear that the smaller θ is, the better range resolution Δ_r and ground range X_r are. At first sight it might be thought to decrease plenty the length of the impulse τ : theoretically, with narrower impulses, even very near objects could be resolved.

The choice of τ is linked to two requirements:

- if $\tau \rightarrow 0$, since $\tau = \frac{1}{B}$, the impulse band (B) increases and there are many problems with the antenna realization. As well, using narrow band signal, in order to avoid leakage effects, with small band lengths it is necessary to use very high values of carrier;
- the energy of an impulse is $E = P\tau$, where P is the transmitting power, and it expresses the sensor capability of detecting: so it is important to transmit an impulse with high energy. Since the maximum power is limited by radar hardware, it is necessary to increase its length τ .

In order to have high detection capability (high E) and high resolution (high B) it is necessary that both τ and B assume a high value, but this condition is impossible with the simple continuous wave impulse considered until now. A way to meet these contrasting requirements is to substitute the short pulse by modulated long ones, provided that they are followed by a processing step (usually referred to as pulse compression). The most popular waveform is the chirp pulse, whose plot is shown in Fig. 9; it is a linearly frequency modulated signal, mathematically expressed as:

$$X(t) = \left(\cos \left(2\pi f_0 t + \frac{\alpha t^2}{2} \right) \text{rect} \left[\frac{t}{\tau} \right] \right) \quad \text{Eq. 4}$$

where f_0 is the carrier frequency and $\alpha = \frac{2\pi}{\tau}B$ is the Linear Frequency Modulation coefficient, called *chirp rate*. Here and in the following the amplitude information, taken unitary, is suppressed, because it does not play any role in the subsequent analysis.

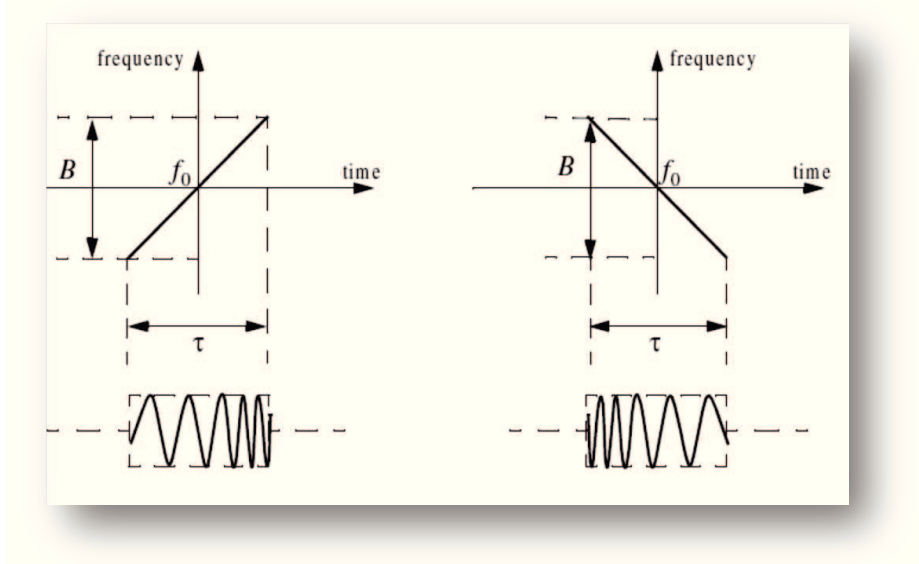


Fig. 9 – Typical LFM waveforms: a) up-chirp, b) down-chirp

The LFM up-chirp instantaneous phase can be expressed by:

$$\psi(t) = 2\pi \left(f_0 t + \frac{\alpha t^2}{2} \right) \quad \text{Eq. 5}$$

Similarly, the up-chirp instantaneous frequency is given by:

$$f(t) = \frac{1}{2\pi} \frac{d}{dt} \psi(t) = f_0 + \alpha t \quad -\frac{\tau}{2} \leq t \leq \frac{\tau}{2} \quad \text{Eq. 6}$$

Differently from a continuous wave impulse, the chirp instant frequency is proportional to time length τ ; in particular it increases if $\alpha > 0$ and decreases otherwise; since $-\frac{\tau}{2} \leq t \leq \frac{\tau}{2}$ and the hypothesis that $\alpha > 0$, the instant frequency varies in the interval:

$$f_0 - \alpha \frac{\tau}{2} \leq f(t) \leq f_0 + \alpha \frac{\tau}{2} \quad \text{Eq. 7}$$

i.e., in the interval considered, the instant frequency variation is:

$$B \cong \Delta f = \alpha \tau \quad \text{Eq. 8}$$

In conclusion, a chirp impulse is characterized by an instant frequency variation proportional to time length and its band can be approximated by this value. So the chirp impulse is important because its band is proportional to its time length. A chirp impulse with a long time length (high energy) can assure high resolution (achievable with a

narrow impulse) as, during the receiving period, the different signal components (each one at a different frequency) are delayed. For this reason, two echoes backscattered from nearby objects are overlapped in the received signal, but the instant frequency $f(t) = (f_0 + \frac{\Delta f}{\tau} t)$ is different for each echo at each instant. So it is possible to separate echoes but they need a subsequent processing in order to obtain again the expression $B = \frac{1}{\tau'}$, where τ' is the time length of the compressed impulse: this is an adaptive filtering of the transmitted signal. Replacing τ with $\frac{1}{B}$, the Eq. 3 can be written:

$$X_r = \frac{c}{2B \sin(\theta)} \quad \text{Eq. 9}$$

i.e. the band of the impulse must be raised in order to improve the resolution. Furthermore, using a chirp signal, if we increase B then τ increases and, consequently, also the transmitted power.

Regarding the azimuth resolution, a RAR can resolve two points only if they are not within the radar beam at the same time, i.e. the distance is greater than the footprint. It implies that the azimuth resolution is independent from the impulse properties, but not from the transmitting system characteristics, as points are not resolved in the footprint. So the azimuth resolution is given by the footprint width (in the azimuth direction):

$$X_a = r \theta_a \cong r \frac{\lambda}{L} \quad \text{Eq. 10}$$

Where L is the seeming dimension of the antenna in the azimuth direction and θ_a is the beam width, in radian, as shown in Fig. 10.

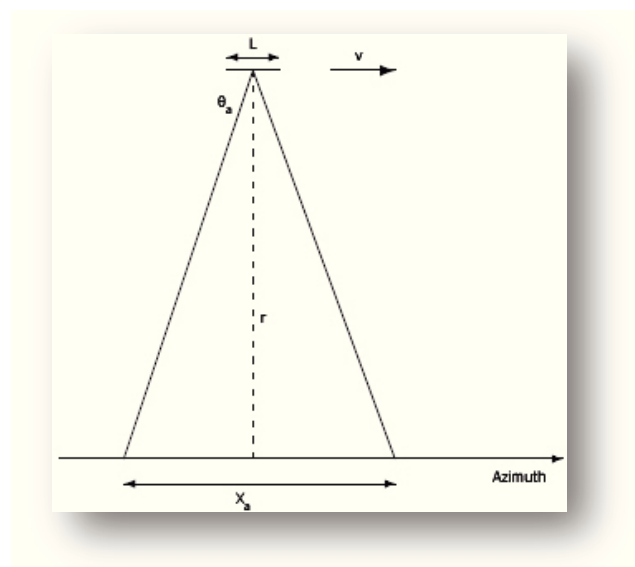


Fig. 10 – Geometry in the azimuth plane

The beam width is expressed by:

$$\theta_a \cong \frac{\lambda}{L} \quad \text{Eq. 11}$$

with the hypothesis that $\theta_a \ll 1$, always valid because of the condition $\lambda \ll L$ necessary for the antenna projection.

It is evident that the RAR system does not assure good resolution in case the radar lies in a shuttle flying on high orbital altitude, aside from its other characteristics. For a RAR system, the azimuth resolution can be improved:

- increasing the antenna dimension
- decreasing the wavelength of the carrier frequency
- decreasing orbital altitude

However, since it is necessary to have high orbital altitude, in order to illuminate an extensive region, microwaves are necessary to penetrate the atmosphere and the antenna size cannot exceed ten meters, it is not possible to improve azimuth resolution of a RAR system.

2.2.1.2 Synthetic Aperture Radar system and resolution

SAR functioning is based on the platform movement along its flight direction: with the hypothesis of constant speed v , a target point on the surface is illuminated while the space covered by the sensor is X . As shown in Fig. 11, calling x_1 the first position (A) and x_n the last position (D) for which the sensor detects the target point, the distance between x_1 and x_n is X .

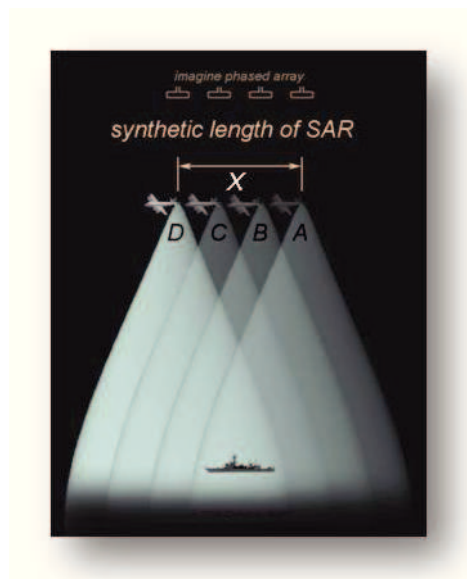


Fig. 11 – SAR system data capture geometry

The antenna is synthesized by moving a small antenna along its track, not continuously, and it can be thought as an antenna array, whose length is X . While the antenna covers a space X , it receives many backscattered echoes from a target point: after processing these echoes the azimuth resolution is improved. It is important to underline that a single echo, backscattered from a target point, changes its wavelength: this effect, called Doppler effect, is used for the image focusing. It concerns the change in frequency and wavelength of a wave for an observer P moving with respect to the source of the waves S . In particular, the frequency transmitted by S increases if the source moves near the observer, and decreases otherwise, as shown in Fig. 12. Backscattered echoes are recorded and the Doppler history, or phase history, is a curve which describes them.

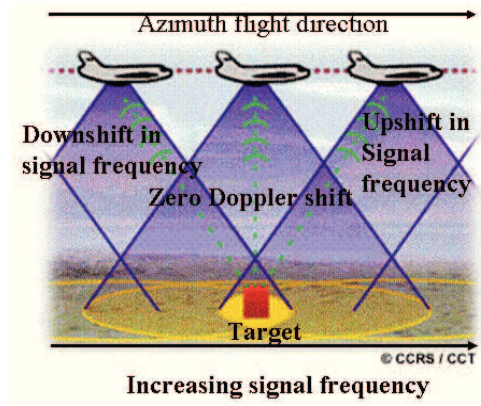


Fig. 12 – Doppler History

For a target point, the received signal is characterized by a quadratic instant phase: it is necessary to consider the effect of range migration. During the synthesizing of the antenna, the range distance varies:

$$r(t) = \sqrt{r_0^2 + x^2} \cong r_0 + \frac{x^2}{2r_0} \quad \text{Eq. 12}$$

The phase difference between the transmitted and received signals, proportional to the sensor-target distance, is expressed as $\varphi(x) = 2\pi f_0 \frac{2r}{c}$, so the phase variation is:

$$\Delta\varphi(x) = \frac{4\varphi f_0}{c} \frac{x^2}{2r_0} = \frac{2\pi x^2}{\lambda r_0} \quad \text{Eq. 13}$$

Since $x = vt$, the azimuth frequency is proportional to t :

$$\Delta f = \frac{1}{2\pi} \frac{d(\Delta\varphi(t))}{dt} = \frac{2v^2 t}{\lambda r_0} \quad \text{Eq. 14}$$

Where Δf is the Doppler frequency, i.e. the difference between the frequency of the transmitted and the received signal, due to the relative movement. The received signal band is:

$$B_a = \frac{2v^2 T_a}{\lambda r_0} = \frac{2v}{L} \quad \text{Eq. 15}$$

The Doppler frequency has the same expression of the chirp band. Therefore, as in the range plane two points are resolved if the time distance is $\Delta t = \frac{1}{B_c}$, in the azimuth they are resolved if $\Delta t = \frac{1}{B_a}$.

Concerning space variables, the distance must be:

$$X_a = v\Delta t = v \frac{1}{B_a} = \frac{L}{2} \quad \text{Eq. 16}$$

Unlike conventional radar systems, the resolution is constant for all the illuminated points of a swath. Moreover the number of received samples and the length of the antenna is function of the range distance: as shown in Fig. 13.

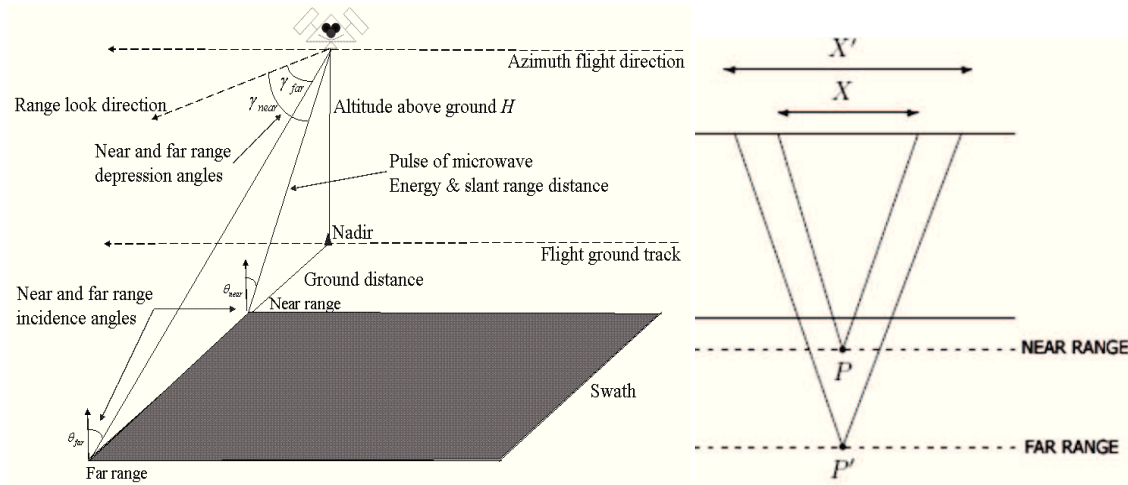


Fig. 13 – Near Range and Far Range

The point P' , in the far range, is illuminated by an antenna longer than in the range case, point P . Consequently the resolution is not function of the distance sensor-target point: if the distance increases, the resolution decreases, but the antenna length increases and it receives more echoes.

Reading Eq. 16, it seems that the resolution can be increased by using a smaller antenna; however, by doing so, there are many energy problems.

2.2.2 GEOMETRY

2.2.2.1 RADAR image distortion

As it happens with all remote sensing systems, the viewing geometry of a radar sensor determines certain geometric distortions on the resultant imagery. However, there are some key features of radar imagery which are due to the side-looking viewing geometry and to the fact that the radar is fundamentally a distance measuring device (i.e. measuring range).

Slant range scale distortion occurs because the radar is measuring the distance to features in slant-range rather than the true horizontal distance along the ground. This results in a varying image scale, moving from near to far range. Although targets are the same size on the ground, their apparent dimensions in slant range are different. This causes targets in the near range to appear compressed relative to the far range. Using trigonometry, ground-range distances can be evaluated from slant range distances and platform altitudes and translated into the proper ground-range format.

Fig. 14 shows a radar image in slant-range display (top) where the fields and the road in the near range on the left side of the image are compressed, and the same image converted to ground-range display (bottom) with the features in their proper geometric shape.

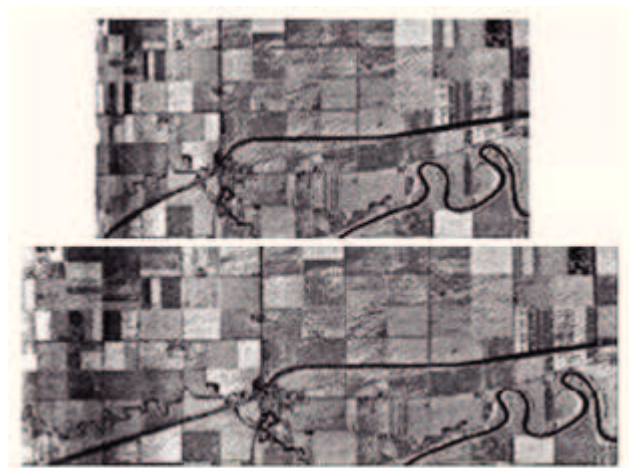


Fig. 14 – Conversion comparison

As cameras and scanners, also radar images are subject to geometric distortions due to relief displacement. This displacement is one-dimensional and occurs perpendicular to the flight path. However, the displacement is reversed with targets displaced towards,

instead of away, from the sensor. Radar foreshortening and layover are two consequences which result from relief displacement, as illustrated in Fig. 15.

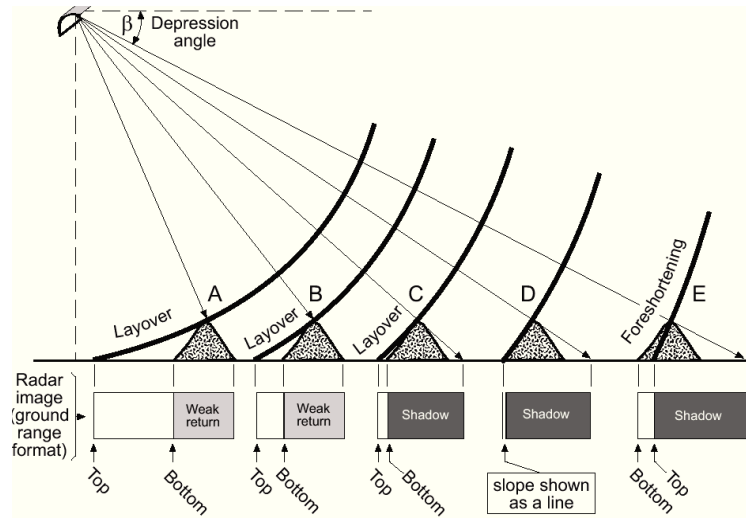


Fig. 15 – Layover and foreshortening effects as a function of the depression angle

Foreshortening

When the radar beam reaches the base of a tall feature tilted towards the radar (e.g. a mountain), before it reaches the top, foreshortening will occur. Again, as the radar measures the distance in slant-range, the slope (with reference to Fig. 16, A to B) will appear compressed and the length of the slope will be represented incorrectly (A' to B'). Depending on the angle of the hillside or mountain slope in relation to the incidence angle of the radar beam, the severity of foreshortening will vary. Maximum foreshortening occurs when the radar beam is perpendicular to the slope so that the slope, the base, and the top are imaged simultaneously (C to D). The length of the slope will be reduced to an effective length of zero in slant range (C'D'). This figure shows a radar image of steep mountainous terrain with severe foreshortening effects. The foreshortened slopes appear as bright features on the image.

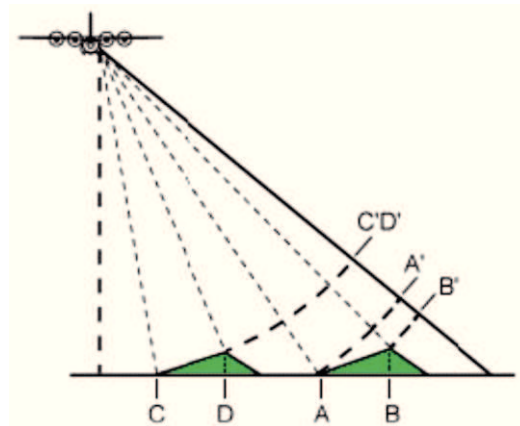


Fig. 16 – Foreshortening effect

Layover

Layover occurs when the radar beam reaches the top of a tall feature (with reference to Fig. 17, B) before it reaches the base (A). The return signal from the top of the feature will be received before the signal from the bottom. As a result, the top of the feature is displaced towards the radar from its true position on the ground, and "lays over" the base of the feature (B' to A'). In case of natural targets, such as mountains or hills, the layover effects on a radar image look very similar to the effects due to foreshortening. As with foreshortening, layover is more severe for small incidence angles, at the near range of a swath, and in mountainous terrain.

Fig. 18 shows an example of the layover effect in presence of man-made objects: the vertex of the pyramid is displaced toward the sensor and appears on the left-side of the image (the slant range of the vertex is shorter than the slant range of the base).

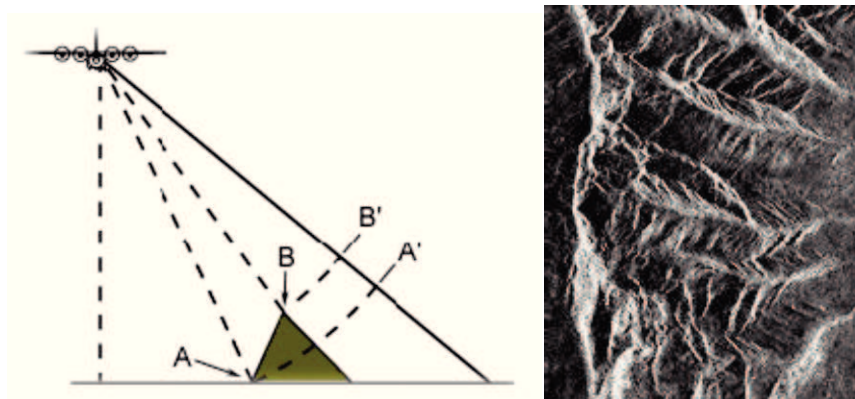


Fig. 17 – Layover effect (left: a schema, right: an example in a mountainous area)

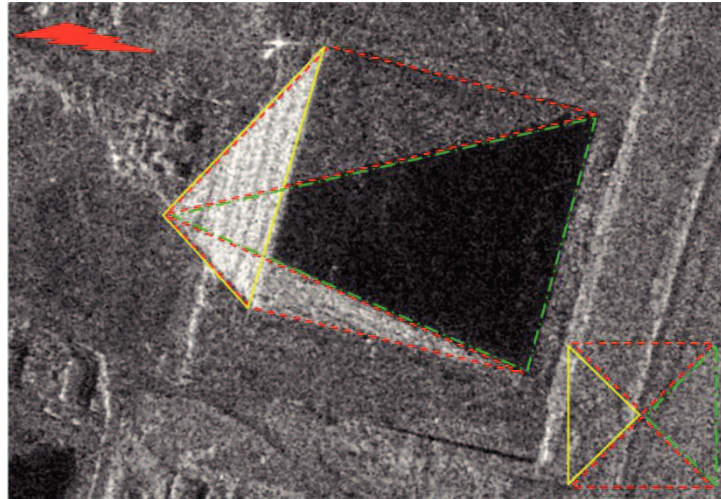


Fig. 18 – Classical example of layover (CSK Spotlight image). The yellow triangle shows the boundary of the Pyramid face illuminated by the sensor

Shadowing

Both foreshortening and layover result in radar shadow. Radar shadow occurs when the radar beam is not able to illuminate the ground surface. Shadows occur in the down range dimension (i.e. towards the far range), behind vertical features or slopes with steep sides. Since the radar beam does not illuminate the surface, shadowed regions will appear dark on an image as no energy is available to be backscattered. Shadow effects increase as a function of the incidence angle, as the radar beam looks more and more obliquely at the surface. This image illustrates radar shadow effects on the right side of the hillsides which are being illuminated from the left.

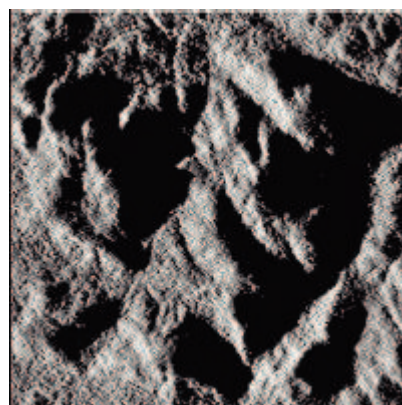


Fig. 19 – Shadowing effect

2.2.2.2 Sensing geometry

Incidence angle and beam

The global incidence angle is the angle between the line of sight and the normal direction with respect to the surface. The incidence angle has a strong influence on the *backscattering* of the target and thus on its identification.

For every image it is possible to define:

- global incidence angle, generally specified at “near range” (pixel closer) or “far range” (pixel farther) with respect to the sensor;
- local incidence angle, comprised between the line of sight and the normal direction with respect to the terrain or the target.

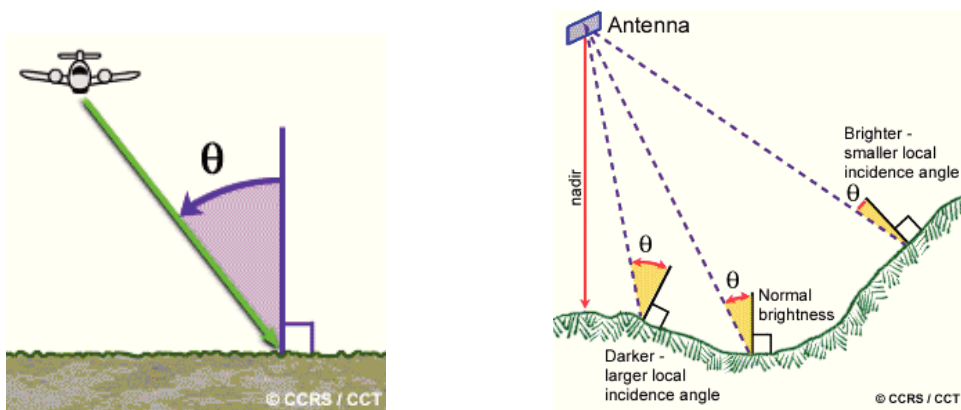


Fig. 20 – On the left an example of global incidence angle; on the right the variation of the local incidence angle in a scene of interest

Generally speaking, for satellite systems which have an electronic beam scanning of the SAR antenna (such as COSMO-SkyMed), the global incidence angle is univocally linked to the sensing beam. Therefore, the satellite has the capability to sense inside the access region exploiting a set of pre-defined beams, partially overlapping to allow the acquisition of regions which are in the middle (see Fig. 21). Depending on the orbital period and repetition cycle, the sensor will have only a set of possible pre-defined viewing geometries.

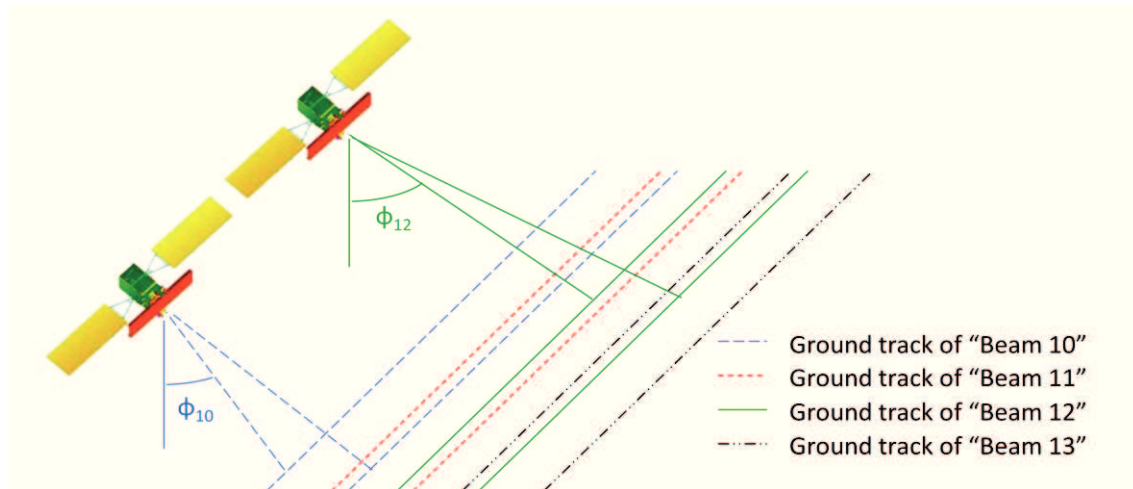


Fig. 21 – Schema of the sensing beams. The look angle ϕ increase as the number of beams

Look side & orbit direction

The acquisitions are usually classified on the bases of:

- the “half” orbit in which they are acquired, generally called *ascending* (in correspondence of the “*dawn*” for sun-synchronous 6am-6pm orbit) and *descending* (“*dusk*”);
- the look side, Right or Left, because the nadir acquisition are not possible for side looking radar;
- sensing time; for a sun-synchronous system as COSMO-SkyMed the morning time window is centred around 6 am local time and lasts less than 2 hours; the afternoon one has the same length and is centred around 6pm local time.

A synthesis of this classification method is given in Fig. 22.

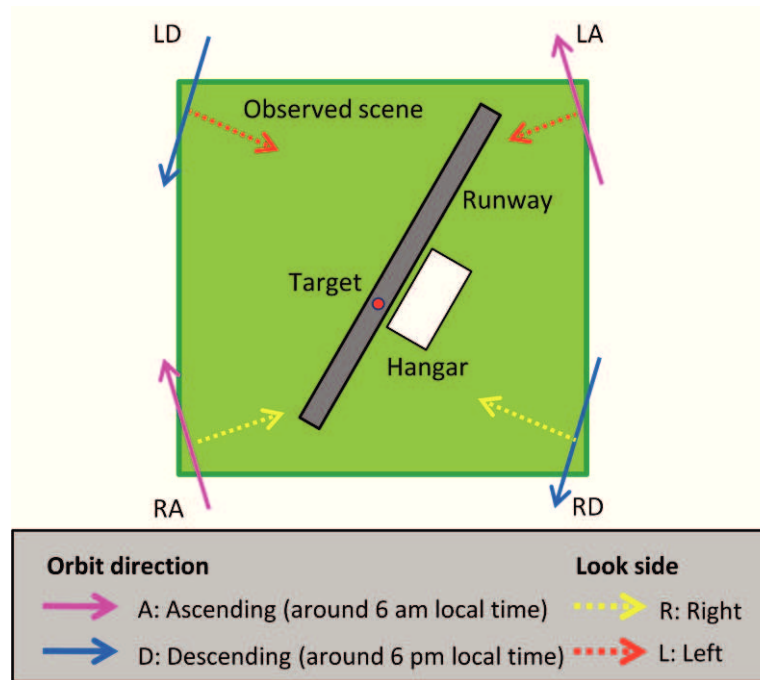


Fig. 22 – Sensing acquisition geometries

2.2.2.3 SAR images geocoding

Geocoding means the conversion of SAR images into a map coordinate system (e.g. cartographic reference system). A particular case of geocoding is orthorectification, that encompasses all the corrections needed to precisely align an image with a map, accounting for actual topography.

SAR standard products are usually geocoded following 2 different approaches, (14):

- Ellipsoidal Geocoding, when this process is performed using an ellipsoid surface as the reference one (e.g. World Geodetic System 84 – WGS 84);
- Ground Terrain Geocoding, when this process is performed with the use of a DEM.

In both cases, the needed parameters are:

- orbital parameters (positions and velocities of the sensor);
- auxiliary info (pixel spacing, range delay for SAR images);
- Digital Elevation Model.

If a really high geolocation accuracy is required, it is possible to improve the geocoding process by means of Ground Control Points (GCPs). In this case, the necessary ancillary data are:

- orbital parameters (positions and velocities of the sensor);

- auxiliary info (pixel spacing, range delay for SAR images);
- Digital Elevation Model;
- Ground Control Points (at least 1 GCP).

In the case of the COSMO-SkyMed system, the Ground Terrain Corrected (GTC) images could achieve high geolocation accuracy even without the use of GCPs, thanks to the high precision of orbital parameters.

In conclusion, as SAR acquisition geometry determine non-linear distortions, especially in case of highly variable terrains, the most appropriate way to geocode SAR data is by applying a range-doppler approach. In (15), the Rational Polynomial Coefficients (RPC) approach, largely adopted in the case of optical images, has been extended to the SAR case, proving to have achieved good result. In any case, considered the necessity to approach the problem in the most general and rigorous way, in the following only the rigorous range-doppler approach will be exploited.

2.2.3 RADAR IMAGE PROPERTIES

2.2.3.1 Speckle

All radar images appear with some degree of what we call radar speckle. Speckle appears as a grainy "salt and pepper" texture in an image. This is caused by random constructive and destructive interference from the multiple scattering returns that will occur within each resolution cell. As an example, an homogeneous target, such as a large grass-covered field, without the effects of speckle would generally result in light-toned pixel values on an image (left picture of Fig. 23). However, the reflections from the individual blades of grass within each resolution cell result in pixels sometimes brighter and sometimes darker than the average tone (left picture of Fig. 23), so that the field appears speckled.

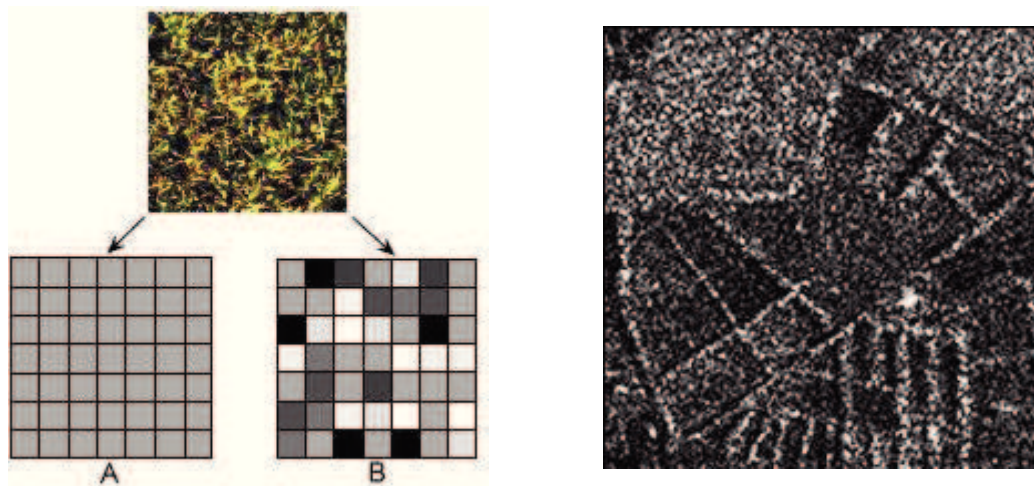


Fig. 23 – Left: the backscattering of a grass field without or with speckle; right: the real speckle noise of a real grass field

Speckle is essentially a form of noise which degrades the quality of an image making its interpretation (visual or digital) more difficult. Thus, it is generally desirable to reduce speckle prior to interpretation and analysis. Speckle reduction can be achieved in two ways:

- multi-look processing;
- spatial filtering.

Multi-look processing refers to the division of the radar beam (A) into several (in this example, five) narrower sub-beams (1 to 5). Each sub-beam provides an independent "look" at the illuminated scene, as the name suggests. Each of these "looks" will also be subject to speckle, but by summing and averaging them together to form the final output image, the amount of speckle will be reduced.

While multi-look processing is usually done during data acquisition, speckle reduction by spatial filtering is performed on the output image in a digital (i.e. computer) image analysis environment. Speckle reduction filtering consists of moving a small window of a few pixels in dimension (e.g. 3x3 or 5x5) over each pixel in the image, applying a mathematical calculation using the pixel values under that window (e.g. calculating the average), and replacing the central pixel with the new value. The window is moved along in both the row and column dimensions one pixel at a time, until the entire image has been covered. By calculating the average of a small window around each pixel, a smoothing effect is achieved and the visual appearance of the speckle is reduced. Fig. 24 shows a radar image before (top) and after (bottom) speckle reduction using an averaging filter. The median (or middle) value of all the pixels underneath the moving

window is also often used to reduce the speckle. Other more complex filtering calculations can be performed to reduce the speckle while minimizing the amount of smoothing taking place.

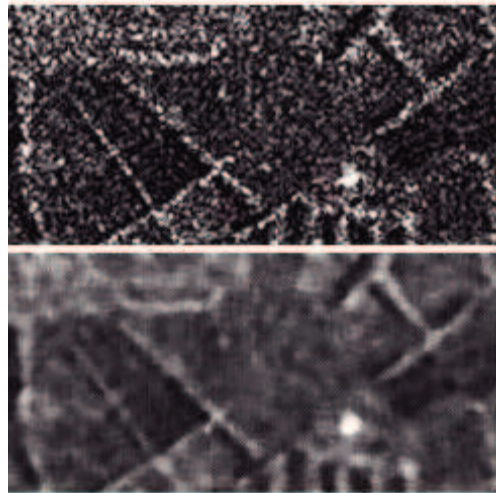


Fig. 24 – A radar image before (top) and after (bottom) speckle reduction using an averaging filter

Both multi-look processing and spatial filtering reduce the speckle at the expense of resolution, since they both essentially smooth the image. Therefore, the amount of the speckle reduction desired must be balanced with the particular application the image is being used for and the amount of detail required. If fine detail and high resolution is required, then little or no multi-look/spatial filtering should be done.

2.2.3.2 Slant - Range Distortion

Another property peculiar to radar images is the slant-range distortion, which was previously discussed in some detail. Features in the near-range are more compressed with respect to features in the far range due to the slant-range scale variability. For most applications, it is desirable to have the radar image in a format correcting this distortion, in order to enable true distance measurements between features. This requires the slant-range image to be converted to 'ground range' display(16). This can be done by the radar processor prior to create an image or after data acquisition by applying a transformation to the slant range image.

2.2.3.3 Antenna pattern

A radar antenna transmits more power in the mid-range portion of the illuminated swath than at the near and far ranges. This effect is known as antenna pattern and results in

stronger returns from the centre portion of the swath than at the edges. Combined with this antenna pattern effect is the fact that the energy returned to the radar decreases dramatically as the range distance increases. Thus, for a given surface, the strength of the returned signal becomes smaller and smaller moving farther across the swath. These effects combine to produce an image which varies in intensity (tone) in the range direction across the image, as shown by Fig. 25. A process known as antenna pattern correction may be applied to produce a uniform average brightness across the imaged swath, to better facilitate visual interpretation.

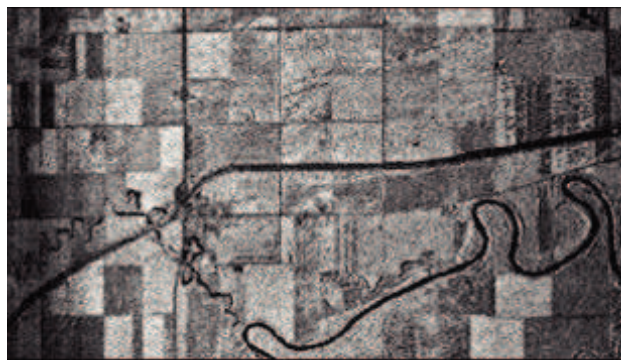


Fig. 25 – A SAR image before the antenna pattern correction

2.2.3.4 Dynamic range

The range of brightness levels that a remote sensing system can differentiate is related to radiometric resolution and is referred to as dynamic range. While optical sensors, for example those carried by satellites such as Landsat and SPOT, typically produce 256 intensity levels, radar systems can differentiate more than 10,000 intensity levels. Since the human eye can only discriminate about 40 intensity levels at one time, this is too much information for visual interpretation, (17).

Most radars record and process the original data as 16 bits (65,536 levels of intensity), which are then further scaled down to 8 bits (256 levels) for visual interpretation and/or digital computer analysis.

2.2.3.5 Calibration

Calibration is a process ensuring that the radar system and the signals it measures are as consistent and accurate as possible. Prior to analysis, most radar images will require relative calibration. Relative calibration corrects for known variations in radar antenna and systems response ensuring that uniform, repeatable measurements can be made over time. This allows relative comparisons between the response of features within a single

image and separate images to be made with confidence. However, if it is necessary to make accurate quantitative measurements representing the actual energy or power returned from various features or targets for comparative purposes, then absolute calibration is necessary.

Absolute calibration attempts to relate the magnitude of the recorded signal to the actual amount of energy backscattered from each resolution cell. To achieve this, detailed measurements of the radar system properties are required as well as quantitative measurements of the scattering properties of specific targets. The latter are often obtained using ground based scatterometers. Furthermore, transponders may be placed on the ground to calibrate an image. These devices receive the incoming radar signal, amplifying and transmitting a return signal of known strength back to the radar. By knowing the actual strength of this return signal in the image, the responses from other features can be referenced to it.

2.2.4 SCATTERING EFFECTS

2.2.4.1 Superficial and volumetric scattering

The scattering behaviour of a target is strongly influenced by the surface characteristics. If the surface is flat, the backscattering will be mainly specular (Fresnel scattering of Fig. 26). This means that the electromagnetic wave will bounce in the opposite direction with respect to the incidence one. If the surface is rough, the backscattering will have a specific three dimensional pattern (see Fig. 26). Part of the transmitted energy will come back to the sensor: this effect is called surface scattering or “single bounce” scattering.

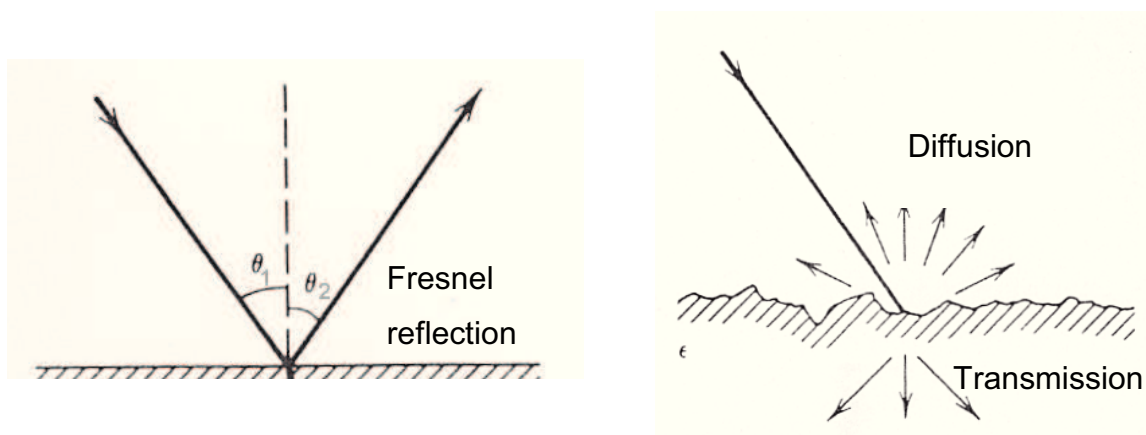


Fig. 26 – left: Fresnel scattering; right: surface or “single bounce” scattering

If the target is made of elements whose dimension is comparable with the wavelength (for the CSK system of 3 cm), e.g. the leaves of a tree (example of Fig. 27), the incident

electromagnetic radiation interacts with a part of the volume of the leaves; in this case the scattering is called “volume scattering”. A classical example of volume scattering is represented by a forest composed by trees similar to the one of Fig. 27.

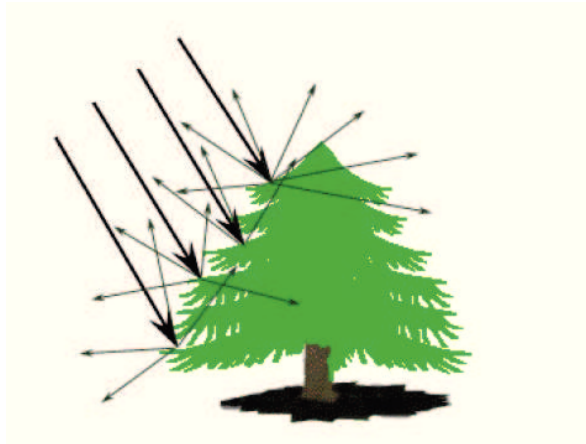


Fig. 27 – Example of “volume scattering”

2.2.4.2 Dihedral or point scatterers

In case of a target geometry characterized by two incident planes creating a dihedral angle (the wall and the ground of Fig. 28), all the electromagnetic paths that experience a double reflection (every path is marked with a specific colour in Fig. 28) – or double bounce – have the same length of the single bounce path illuminating the intersection line (path A of Fig. 28).

This scattering mechanism causes a strong scattering in correspondence with the intersection line between the two incident planes because all the energy impinging on the wall and on the ground is concentrated in a single line.

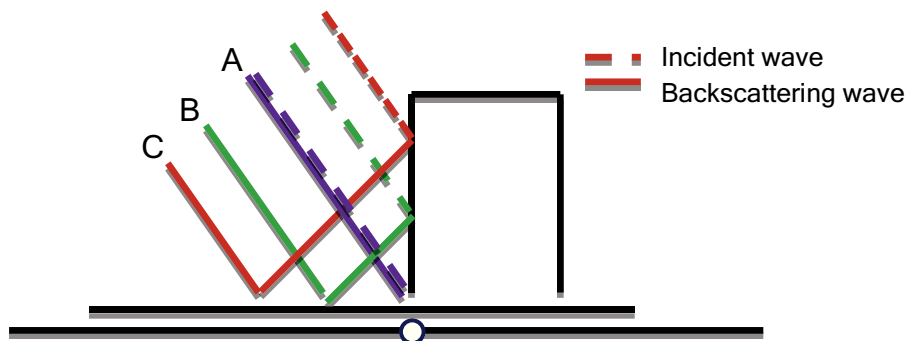


Fig. 28 – Dihedral or “double bounce” scattering mechanism (B and C paths have the same length of the “single bounce” path A)

2.2.4.3 Multipath

For peculiar geometries, a special phenomenon called multipath can be experienced: in these cases, the electromagnetic signal experiences more than 2 bounces before coming back to the sensor. Obviously this kind of backscattering will be more distant with respect to the sensor than the single or double bounce.

As depicted in Fig. 29, in case of a “triple bounce” the backscattering energy coming back from R point experiences a path equivalent to the “single bounce” path of the virtual point V, symmetric of the R point with respect to a symmetry plane coincident with the one of the first and last bounce (in this case the wall of the building).

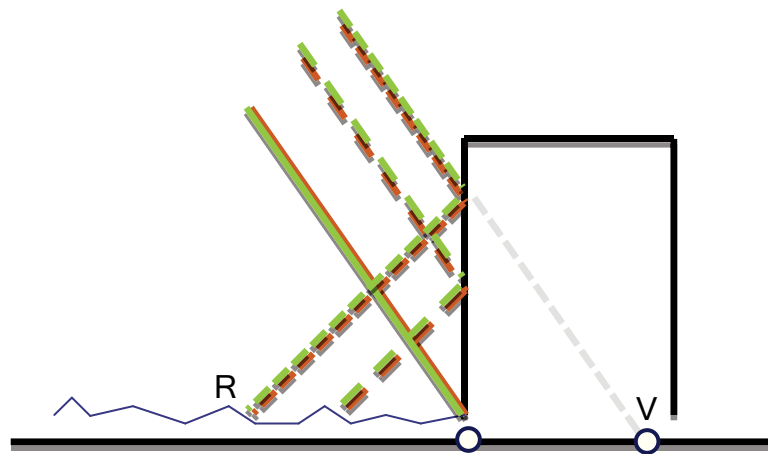


Fig. 29 – Scattering mechanism of a “triple bounce” phenomenon

Examples of multipath that can be experienced:

1. in case of bridges over flat water bodies; in this case the *multipath* and/or triple bounce effects are due to the inferior parts of the bridge;
2. electric lines or ropes over specular surfaces;
3. other cases in which the relative position between several flat surfaces determine complex multipath effects (e.g. the centre of a town).

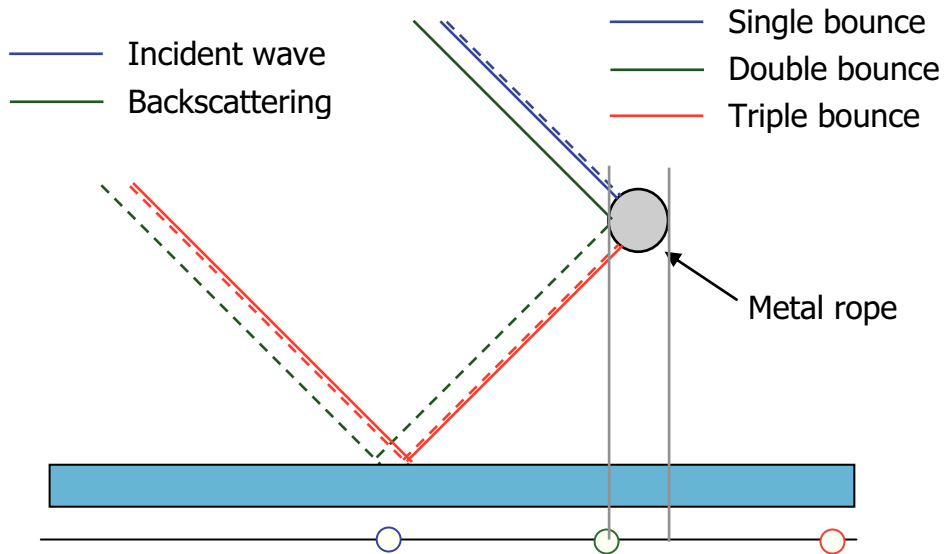


Fig. 30 – Single, double and triple bounce: a rope over a flat water surface

With reference to Fig. 30, it is possible to summarize the following scattering effects:

- one “single bounce” or direct scattering phenomenon, caused by the specular reflection on the upper-left side of the rope, perpendicular to the looking direction, which is recorded in the image closer to the sensor than the other scattering behaviours;
- a “double bounce” effect, caused by the successive reflections on the left side of the rope and on the water, which is recorded in a position corresponding to the intersection of the line tangent to the left side of the rope and the water surface, thus farther from the sensor than the direct scattering;
- a “triple bounce effect”, caused by the three successive specular reflection on the water, on the lower-left side of the rope and again on the water, which is recorded in the farthest position with respect to the other backscattering points.

2.3 COSMO-SKYMED

2.3.1 THE SYSTEM

COSMO-SkyMed is the first example of Dual-Use (civil and military) remote sensing system, conceived and designed in order to create a global service supplying provision of data, products and services compliant with well-established international standards and relevant to a wide range of applications, such as Risk Management, Scientific and Commercial Applications and Defence/Intelligence Applications (18).

This system, funded by ASI (Italian Space Agency) and Italian MoD (Ministry of Defence), consists of a constellation of four mid-sized satellite, in low Earth orbit, each equipped with a multi-mode high-resolution SAR operating at X-band (see Fig. 31). Ground infrastructures are full dedicated for managing the constellation and assure the collection, archiving and distribution of the acquired data.

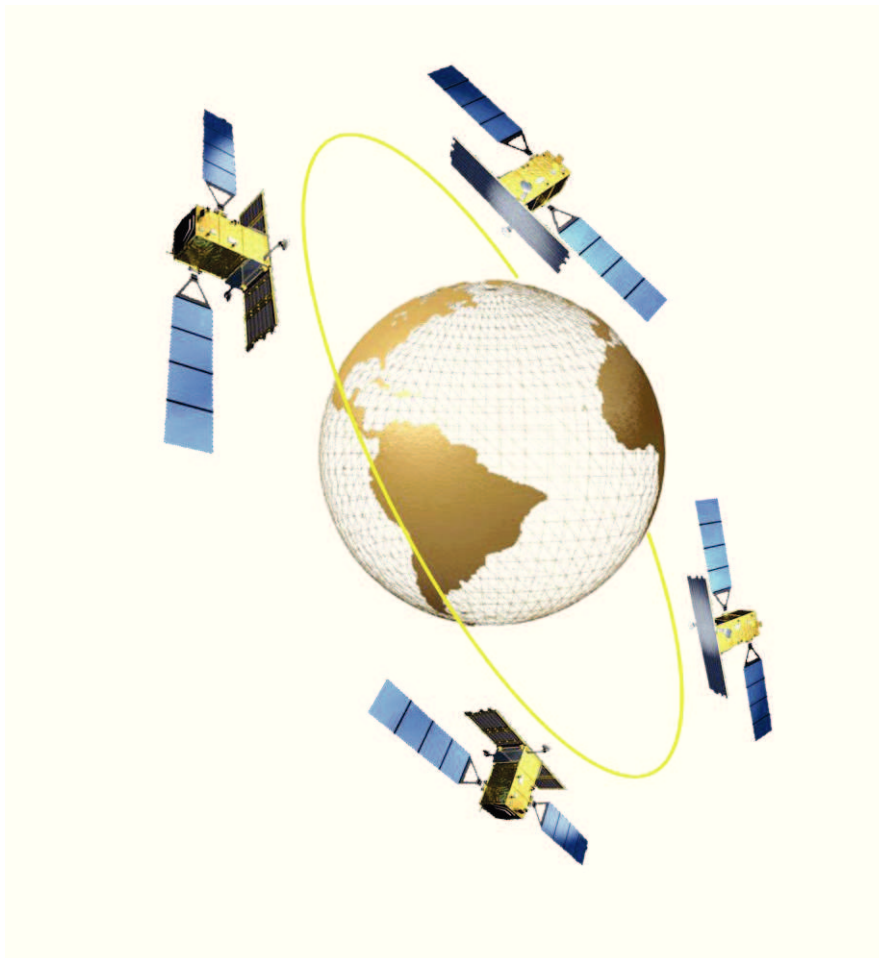


Fig. 31 – The COSMO-SkyMed constellation

The set of requirements imposed at highest level has brought to the following needed performances (18):

- large amount of daily acquired images;
- satellites accessibility worldwide;
- all weather and Day/Night acquisition capabilities;
- very short interval between the finalization of the user request for the acquisition of a certain geographic area and the release of the remote sensing product (System Response Time);
- very fine image quality (e.g. spatial and radiometric resolution);
- possibility of image spatial resolution trade-off with size at the most possible extent and including sub-meter resolution;
- capability to be a cooperating, interoperable, expandable to other EO (Earth Observation) missions, multi-mission borne element providing EO integrated services to large User Communities on a worldwide scale.



Fig. 32 – The COSMO-SkyMed satellite during the manufacturing activities (www.corriere.it)

Since these requirements need many combinations between size and spatial resolution, SAR was chosen as a multimode sensor, as shown in Fig. 33, operating in :

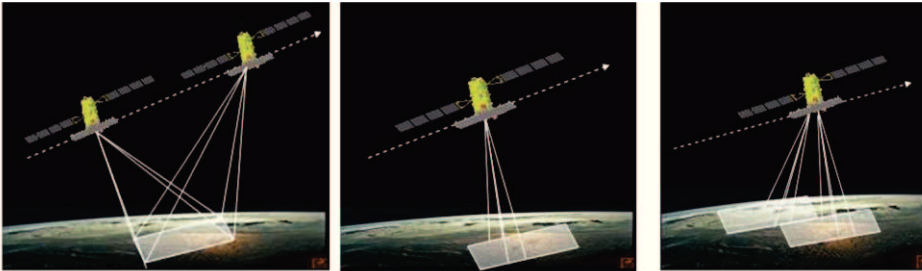
- Spotlight mode, for metric resolutions over small images (10km x 10km). In order to illuminate the scene for a period longer than the one of the standard strip, during the acquisition time the antenna is steered both in the azimuth and in the elevation plane, increasing the length of the synthetic antenna and therefore the azimuth resolution. The acquisition is performed in frame mode

and is limited in the azimuth direction, because of the antenna pointing. There are two CSK Spotlight modes, whose one (Spotlight-2) is only for military operations.

- Stripmap mode, for metric resolutions (3 - 15m) over tenth of km images (40km x 40km). It is the most common imaging mode, obtained by pointing the antenna along a fixed direction with respect to the flight platform path. The antenna footprint covers a strip on the illuminated surfaces as the platform moves and the system operates.

There are two CSK Stripmap modes: the Himage and the PingPong. The latter implements a strip acquisition by alternating a pair of Tx/Rx polarizations across bursts (cross polarization)

- Scansar mode for medium to coarse (100 m) resolution over large swath. There are two different implementations for CSK Scansar mode: WideRegion and HugeRegion, achievable by grouping the acquisition over few sub-swaths.



	Spotlight Smart	Spotlight Enhanced	Stripmap Himage	Ping-Pong	ScanSar Wide	ScanSar Huge
Resolution m x m	-	1 x 1	3 x 3	15 x 15	30 x 30	100 x 100
Swath Km x Km	-	10 x 10	40 X 40	30 X 30	100 X 100	200 X 200
Polarization	-	HH or VV	HH or VV or HV or VH	HH & VV HV & VV VV & VH	HH or VV or HV or VH	HH or VV or HV or VH

Fig. 33 – CSK SAR sensing modes

2.3.2 PRODUCTS

The COSMO-SkyMed products are divided into three classes: Standard products, Higher level products (for mid or even high level remote sensing applications) and Service products (for internal use only).

SAR Standard products are the basic image products of the system. Some examples are shown in Fig. 34 and can be divided into 4 typologies, (19):

- Level 0 RAW data: this data consist of time ordered echo data, obtained after decryption and decompression and after applying internal calibration and error compensation; it include all the auxiliary data required to produce the other basic and intermediate products;
- Level 1A, Single-look Complex Slant product, RAW data focused in slant range-azimuth projection, which is the sensor natural acquisition projection;
- Level 1B, Detected Ground Multi-look product, obtained detecting, multi-looking and projecting the Single-look Complex Slant data onto a regular grid on the ground. It is important to underline that Spotlight Mode products are not multilooked;
- Level 1C/1D, Geocoded product GEC (1C level product) and GTC (1D level product), obtained projecting the 1A product onto a regular grid in a chosen cartographic reference system. In case of Lev 1C, the reference surface is the earth ellipsoid while for Lev 1D a DEM (Digital Elevation Model) is used to approximate the real earth surface. In Lev 1D product is constituted by the backscattering coefficients of the observed scene, multilooked (except for Spotlight Mode), including the annexed Incidence Angles Mask.

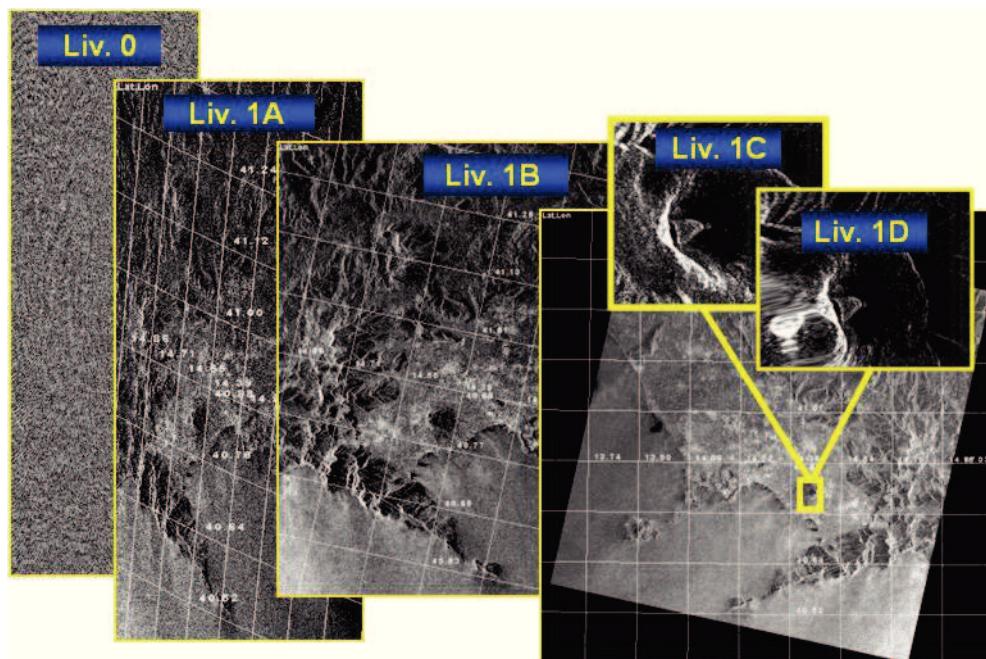


Fig. 34 – COSMO-SkyMed Standard Products

CHAPTER 2 - SAR Systems and Data

For example, in accordance with the image used for this research, the Stripmap Himage product characteristics are those of Tab. 1.

	Lev 0	Lev 1A	Lev 1B	Lev 1C/1D
Swath [km²]	~ 40Km x 40Km			
Incidence angle	~ 20° ÷ 60°			
Polarization	Selectable among HH, HV, VH or VV			
Product size [MB]	500÷1250	1150÷1800	390÷5900	<1118
Eq. number of looks	NA	1	~3	~3
Gr. Range res. [m]	NA	< 3	< 5.0	< 5.0
Az. Resolution [m]	NA	< 3	< 5.0	< 5.0
Geoloc. Acc.	NA	NA	< 25	< 25 < 15

Tab. 1 – Stripmap-Himage product characteristics

For standard use, the format adopted for products distribution is HDF5, which allows to store image layers and ancillary information.

The HDF5 (Hierarchical Data Format) format and software was developed and supported by NCSA (National Centre for Supercomputing Applications University of Illinois) since 1988 and is freely available. It is used worldwide in many fields (including environmental science, the study of neutron scattering, non-destructive testing and aerospace research), in NASA's EO System and in the Department of Energy's Accelerated Strategic Computing Initiative.

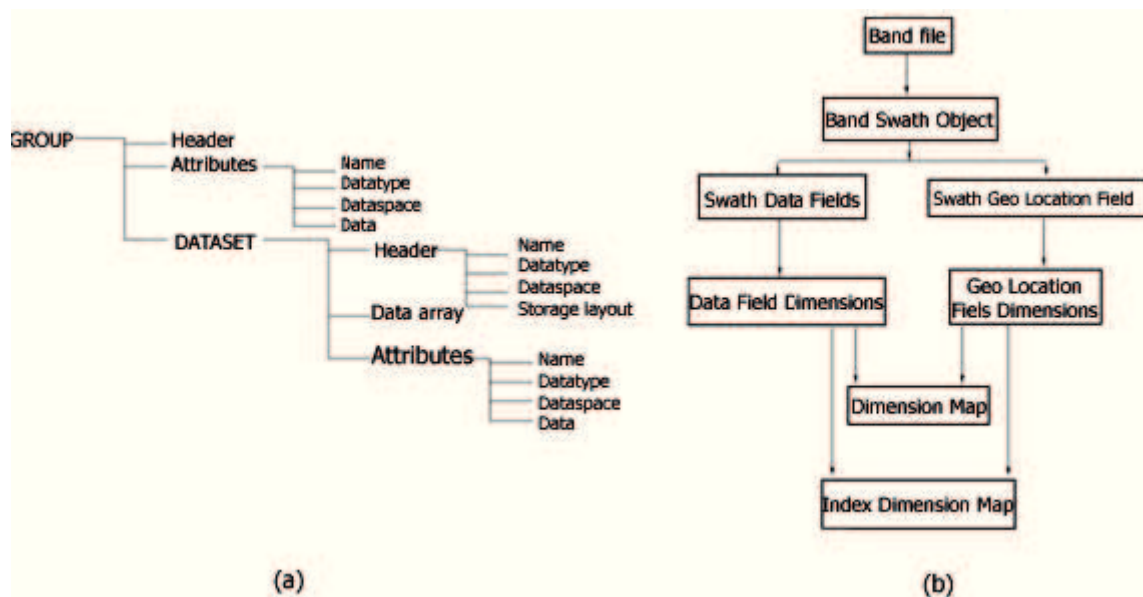


Fig. 35 – HDF5 hierarchical organization and the application of HDF structure to EO image

HDF5 files are organized in a hierarchical structure, as shown in Fig. 35 (a), with two primary structures, groups and datasets.

2.3.3 APPLICATIONS AND EXPLOITATION

Information gathering and rapid mapping based on earth observation images are key services for an effective emergency response. They exploit images acquired by remote sensors for the evaluation of flooded areas, earthquake damage assessment, landslides hazard evaluation, oil spill detection and for other natural and man-made post-event assessment. Time requirements for products' availability are very tight because the value of an information, in such cases, decreases dramatically with time. In this paragraph a synthesis of the main civilian domains of application of the COSMO-SkyMed system, based on the services developed by the Italian Space Agency and the e-GEOS society, (18) and (20).



Fig. 36 – A pictorial of the main application of the COSMO-SkyMed system (courtesy of e-GEOS)

2.3.3.1 Earthquake & Volcanoes monitoring and disaster management

Earthquakes are one of the most serious natural events affecting large areas world-wide, often causing destruction and massive loss of life. Services include pre and post disaster mapping through data analysis and satellites data integration with other available geospatial information. Different kinds of data from different sources concur to the

CHAPTER 2 - SAR Systems and Data

creation of damage assessment analysis, trafficability analysis, pollution risk evaluation, oil spill detection map, fire detection map and others.

During a crisis, Differential Interferometry (D-InSAR) displacement maps can be analysed and integrated with in-situ data. SAR data are also used for damage assessment, both with traditional methods and integrated with medium and high resolution optical satellite data. In the prevention phase, important information are provided by historical terrain displacements obtained by multi-temporal SAR interferometry.

To facilitate volcano risk management, during the prevention and crisis phase, a continuous monitoring of terrain movements by means of differential interferometric analysis of SAR data allows the evaluation of the uprisings associated with volcanic activity.

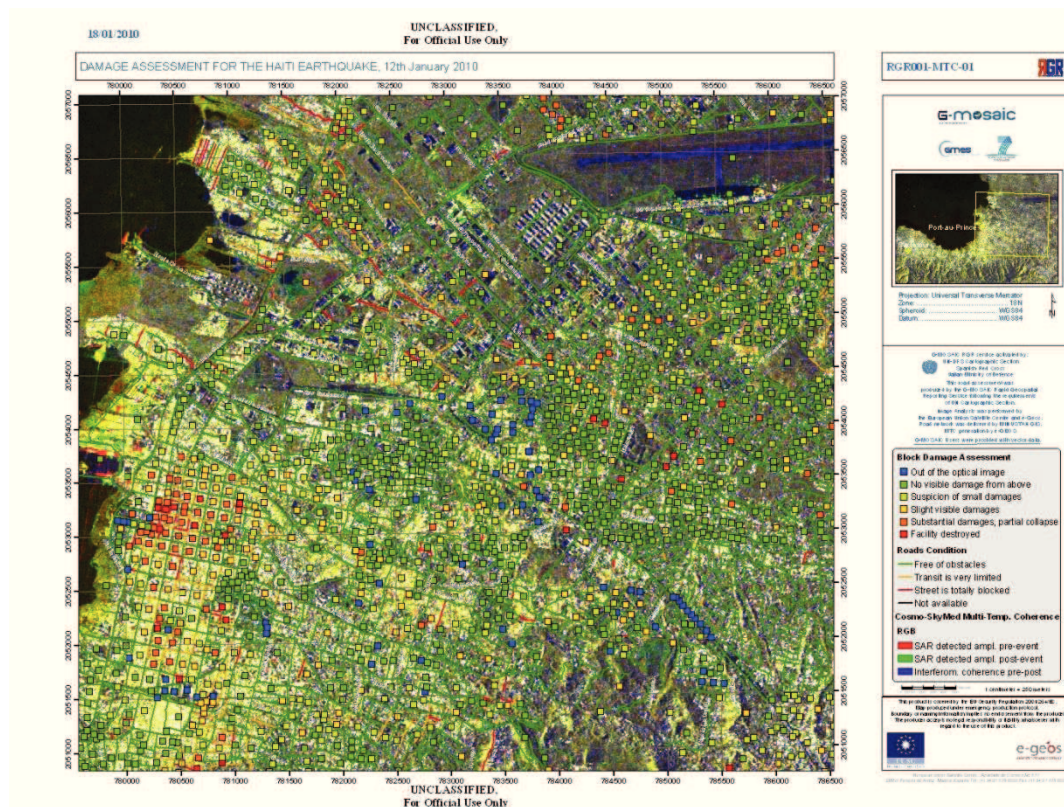


Fig. 37 – COSMO-SkyMed Interferometric Land Use- Port-au-Prince, Haiti, post earthquake, (21)

2.3.3.2 Floods relief management

SAR reflectivity data are used in hydrology for flooded areas detection. The advantage of using SAR data compared to optical data is mainly the all-weather capability of SAR, considering that typically flooded areas remain cloudy for many hours after an event.

COSMO-SkyMed SAR images allow an improvement of flooding management applications because of the optimal response and revisit time of the overall system.



Fig. 38 – The successful launch of the four COSMO-SkyMed satellites makes it the largest constellation of SAR satellite to fulfil operational remote sensing needs

2.3.3.3 Maritime surveillance

Satellite borne SAR instruments can provide an efficient way of ship detection in the open sea and measuring, through wake and Doppler displacements and their speed and direction. Repeated observations can contribute to a maritime surveillance system, complementing the information on routes from coastal radars and shipboard Automatic Identification Systems (AIS). COSMO-SkyMed constellation significantly improves the role of SAR in this application because of its high revisit frequency. High spatial resolution observing modes can provide ship characterization / classification.

Oil spills down capillary waves on the sea surface. The SAR instrument can easily detect oil slicks as areas of lower back-scattered signal, provided that the sea is not too calm or too rough. The applications of oil slick detection encompass disasters (sinking tankers), illegal activities (tank washing) and oil exploration (natural seepage).

2.3.3.4 Subsidence monitoring

Detailed maps of the areas exposed to landslide risk are needed for prevention and emergency activities and for mitigation works planning. This need requires to classify areas according to risk indexes, evaluating the territorial and environmental factors of propensity for landslide risk.

CHAPTER 2 - SAR Systems and Data

Risk Maps can be produced by means of Differential Interferometric applications (D-InSAR). New techniques, exploiting punctual permanent scatterers interferometry (PS-InSAR), are now available to cope with this task.

2.3.4 THE FUTURE: COSMO-SKYMED SECOND GENERATION

“COSMO-SkyMed Seconda Generazione” (CSG) has been conceived according to the requirements stated by the Italian Space Agency and the Italian Ministry of Defence, at the twofold need of ensuring operational continuity to the currently operating “first generation” COSMO-SkyMed constellation, while achieving a step ahead in terms of functionality and performances, also by capitalizing the “Lesson learned” from the first generation, (22).

CSG is a very high performance, reliable and highly autonomous system. In order to guarantee the operational continuity with CSK, CSG space segment is composed by 2 SAR satellites placed in the same orbital plane of the first generation constellation: a down-dusk sun-synchronous orbit @ 620 Km altitude and with a 06:00 am Local Time at Ascending Node. The quasi-polar orbit grants global Earth coverage, while the SAR sensor allows to achieve all-weather, night-and-day sensing capability.

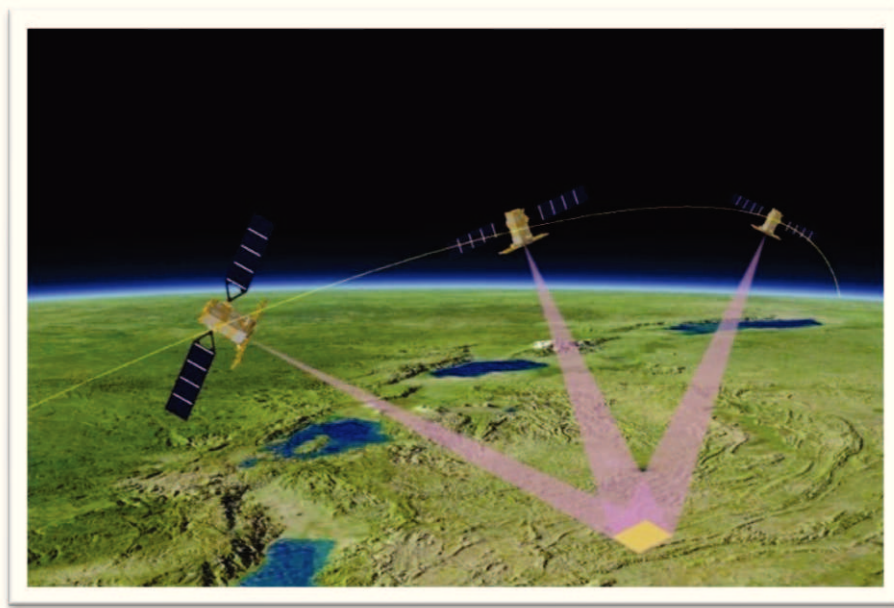


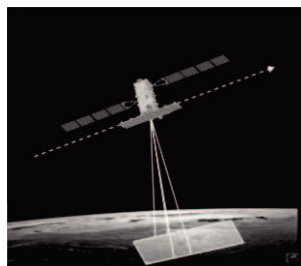
Fig. 39 – A pictorial view of the improved agility of the CSG system

The satellite represents the state of the art of LEO spacecraft medium size technology and is based on a modular architecture whose main features are:

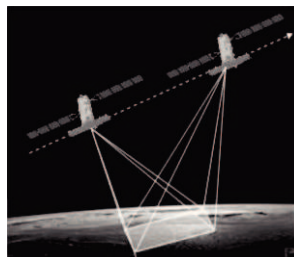
- a side looking SAR payload capable to access both right and left with respect to the flight direction with a capability to access area with $20^\circ \div 60^\circ$ incidence angle corresponding to an on-ground access area of about 2×650 Km;

CHAPTER 2 - SAR Systems and Data

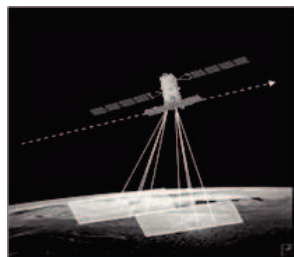
- a Payload Data Handling and Transmission (PDHT) comprising all the functions necessary for the real-time acquisition, storage and handling of SAR data generated by the payload, and for their transmission to the ground station;
- a 3 axis stabilization system, with Sun and Stars sensors, a set of 4 reaction wheels, a Control Moment Gyro Assembly and 3 torque-rods as actuators, with steering capabilities on each axis, high pointing accuracy and knowledge and real time orbit determination;
- a Mil-1553 command bus as computer, avionic and satellite communication back-bone and Leon 3 processor architecture;
- 2 solar array wings will provide energy to be stored in a modular battery;
- a monopropellant propulsion system with 150 kg of hydrazine and dual branch with 6 thrusters.



Stripmap (with single, dual and quad-pole capability) and Ping Pong (with four polarization capability in burst mode)



Spotlight (with single and dual polarization capability)



ScanSAR (with single and dual polarization capability)

Fig. 40 – CSG imaging modes

CSG satellites are composed by the following main architectural components:

- PRIMA Platform;
- Synthetic Aperture Radar (SAR);
- Payload Data Handling and Transmission (PDHT).

CHAPTER 2 - SAR Systems and Data

The Spacecraft is capable to largely simplify ground operations by providing on board a powerful commanding tool and a large capability for command storing in order to achieve up to 24 hours of operational autonomy. Tab. 2 reports the main features of the satellite.

In Fig. 41, 2 sketches of the stowed and deployed satellite are reported.

Wet Mass @ Launch	≤ 2161 Kg (Current estimation)
Operational Lifetime	7 years
Launcher Compatibility	Delta II, Falcon 9, Soyuz
Orbit Injection Type	Direct into target SSO
Operative Autonomy	24 h
Attitude Stabilization	3 axes
Navigation and Time Reference	GPS
SAR Payload	X-Band (9.6 GHz)
Imaging Capability	Multimode with electronic steering
Data Down Link Rate	2X260 Mbps
On-Board Storage Memory	1500 Gbit

Tab. 2 – Main satellite bus and payloads characteristics.

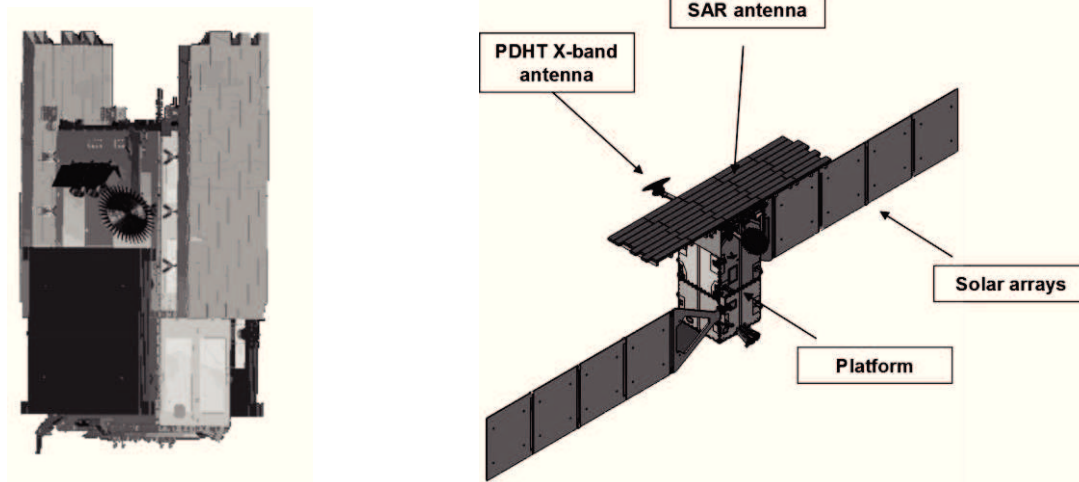


Fig. 41 – Satellite architectural sketch.

CHAPTER 3 - THEORY AND IMPLEMENTATION

3.1 3D INFORMATION FROM EARTH OBSERVATION DATA: SCENARIO ANALYSIS

SAR images have been demonstrated to be a precious source of 3D information, especially regarding:

- Digital Elevation Model of the earth terrain or surface;
- Vector data (points, vectors), representing simple features of more complex objects;
- simple shape (e.g. cuboids, circle, etc), mainly to model buildings and roads.

Digital Elevation coverage represents the first and most investigated 3D information derived from SAR data. SAR Interferometry (InSAR) has proven to be the most suitable technique to generate elevation data since the first experiments with the European Radar Satellite (ERS) mission, (23),(24) and(25), therefore further developments guided to the conduction of a specific mission: the Shuttle Radar Topography Mission, (26). Nowadays, the two major programs in the field of radar remote sensing which both have the capability to conduct interferometric acquisitions for Digital Elevation Model generation are:

- COSMO-SkyMed, that has a specific orbital configuration named “Tandem” mode, in which an interferometric couple is acquired with 20” decorrelation time, (18),(27) and(28);
- TanDEM-X, that is an earth observation mission devoted to DEM production, working in conjunction with TerraSAR-X satellite (29).

An extension of the InSAR technique is represented by the Permanent Scatterers (PS-InSAR) one. Firstly developed to monitor subsidence, the PS-InSAR has shown interesting results when applied to DEM generation and urban environment modelling, (30), and allows the generation of an high density cloud of 3D points corresponding to the permanent scatterers itself. The PS relative positioning accuracy has been demonstrated to be in the order of 1 m in the three dimensions and precise measures of the height of urban scatterers can be achieved.

On the other hand, stereo SAR techniques, also called radargrammetric techniques, have been investigated for the production of DEM starting from data acquired in a proper bistatic geometry, (2) and (3). Aiming at studying the potentialities of a bistatic system, especially regarding the radargrammetry performance for DEM production, the SABRINA mission has been proposed to flight in conjunction with the COSMO-SkyMed one, (31). New researches in the field of radar electromagnetic propagation and Earth tide compensation will extremely improve the ranging accuracy, going towards centimetre accuracy, (32), thus giving to the radargrammetric technique more appeal and perspectives for the future.

If DEM coverage is the most investigated 3D application of SAR data, it is not the unique. In fact, other research activities have been carried out to extract discrete 3D information such as 3D points, vectors and shape.

A comprehensive approach in reconstruction of buildings from multi-aspect SAR images is provided in (5), in which simple building objects are modelled as cuboids and an approach for automatic 3D reconstruction of objects from multi-aspect metric-resolution SAR images is developed. Other studies work with interferometric techniques to extract the buildings features from SAR data, (33).

Obviously, data fusion of SAR data with optical images enhance the perspective of features extraction, due to the complementary information that can be derived from the two sources, (34).

A further step towards 3D information extraction is represented by tomographic applications, aiming at focusing the SAR image in the true three dimensions, (35) and (36). This technique has important implications for future developments of SAR system, when constellations of satellites or new technologies will better support the necessities in terms of numbers of images and geometry of acquisition.

These results pave the way to high resolution 3D modelling of the target of interest.

3.2 INTERSECTION OF SPACEBORNE STEREO SAR DATA

This paragraph will give a complete review of the state-of-art theory regarding SAR space intersection, explaining the concepts which are at the base of the innovations proposed by my thesis work .

3.2.1 RANGE-DOPPLER APPROACH

The removal of geometric distortions requires a high precision geocoding of the image. The geometric correction has to consider the sensor and processor characteristics, therefore a rigorous Range-Doppler approach surely fits the need. For each pixel the following two relations must be fulfilled.

The first equation, known as the Range equation (the radar measures distances and the single slant-range pixel has a measured distance from the platform):

$$R_{sr} = |\vec{R}_s - \vec{R}_t| \quad \text{Eq. 17}$$

and the Doppler equation (each slant-range pixel experiences a measured Doppler frequency):

$$f_D = \frac{2}{\lambda R_{sr}} (\vec{R}_s - \vec{R}_t) \cdot (\vec{V}_s - \vec{V}_t) \quad \text{Eq. 18}$$

where

- R_{sr} = slant range;
- \vec{R}_s, \vec{R}_t = spacecraft and backscatterer element position;
- \vec{V}_s, \vec{V}_t = spacecraft and backscatterer element velocity;
- λ = wavelength;
- f_D = processed Doppler frequency.

Using these equations, the relationship between the sensor, each single backscattering element and their related velocities is calculated. This complete reconstruction of the imaging and processing geometry also takes into account the topographic effects (foreshortening, layover) as well as the influence of Earth rotation and terrain height on the Doppler frequency shift and azimuth geometry.

3.2.2 IMAGE TO GROUND COORDINATES TRANSFORMATION

The location of a generic pixel, expressed in the Earth Centered Earth Fixed (ECEF) reference frame, for a given image frame can be derived from the simultaneous solution of three equations: the Range Equation (Eq. 17), the Doppler Equation (Eq. 18) and the Earth Model Equation, (37). If we assume that the earth model is the WGS84 earth ellipsoid, we obtain the following third condition:

$$\frac{X^2}{a^2} + \frac{Y^2}{a^2} + \frac{Z^2}{b^2} = 1 \quad \text{Eq. 19}$$

CHAPTER 3 - Theory and Implementation

where:

- X, Y, Z represent the target location in a ECEF reference frame;
- a, b, respectively WGS84 semi-major and semi-minor axis.

Assuming that the images are zero doppler processed, we obtain

$$f_D = 0 \quad \text{Eq. 20}$$

Considering a fixed target on the earth, its velocity in a earth rotating reference frame would be:

$$\vec{V}_t = \vec{\omega}_e \times \vec{R}_t = \vec{0} \quad \text{Eq. 21}$$

where $\vec{\omega}_e$ represents the angular earth rotation velocity in a ECEF reference frame.

So we obtain the following system:

$$\begin{cases} \frac{X^2}{a^2} + \frac{Y^2}{a^2} + \frac{Z^2}{b^2} = 1 \\ R_{sr} = |\vec{R}_s - \vec{R}_t| \\ f_D = \frac{2}{\lambda R_{sr}} (\vec{R}_s - \vec{R}_t) \cdot \vec{V}_s = 0 \end{cases} \quad \text{Eq. 22}$$

This system can be solved by means of an iterative algorithm, through the introduction of an objective function.

Satellite position and velocity will be evaluated starting from the knowledge of the azimuth time, that is a function of:

- the pixel line index “i”;
- the zero doppler azimuth first time;
- the Pulse Repetition Frequency (PRF) of the radar sensor.

At the same, slant range is a function of:

- the column index “j”,
- the zero doppler range first time
- the column time interval.

3.2.3 RIGOROUS STEREO METHOD

Two basic equations for each orbit can be treated as observation equations in space intersection, range equation (Eq. 17) and doppler equation (Eq. 18), (38). Thus, the

problem of space intersection could be solved for an unknown ground point using two images to form observation equations, Eq. 23:

$$\begin{cases} F_1 = \frac{2}{\lambda R_{sr_1}} (\vec{R}_{s_1} - \vec{R}_t) \cdot \vec{V}_{s_1} = v_1 \\ F_2 = R_{sr_1} - |\vec{R}_{s_1} - \vec{R}_t| = v_2 \\ F_3 = \frac{2}{\lambda R_{sr_2}} (\vec{R}_{s_2} - \vec{R}_t) \cdot \vec{V}_{s_2} = v_3 \\ F_4 = R_{sr_2} - |\vec{R}_{s_2} - \vec{R}_t| = v_4 \end{cases} \quad \text{Eq. 23}$$

Where

- R_{sr_1}, R_{sr_2} = slant range of the target respectively in the first and the second image
- $\vec{R}_{s_1}, \vec{V}_{s_1}$ = spacecraft position and velocity for the first image;
- $\vec{R}_{s_2}, \vec{V}_{s_2}$ = spacecraft position and velocity for the second image;
- $v_1 \div v_4$ = residuals of the 4 equations.

The equations in Eq. 23 are used to derive the normal equation so that the sum of the squares can be minimized, Eq. 24:

$$\sum_{i=1}^4 v_i^2 \rightarrow \min \quad \text{Eq. 24}$$

Where F_1, \dots, F_4 are the observation equations and v_1, \dots, v_4 are the residuals of each observation equation. All the details in (38).

3.2.4 GENERALIZED N-IMAGES STEREO MODEL

The extension of the rigorous Stereo Method to the exploitation of n-images starts from the basics described at the paragraph 3.2.3. This multi-image space triangulation technique has been proposed in (39) to create a network of control points for calibration purposes.

Considering that the final position accuracy of a point is a function of the:

- satellite position and velocity accuracy;
- Doppler centroid estimation accuracy;
- slant range measurement accuracy;

the advantages that would be experienced exploiting more than 2 couples of observation equations (i.e. more than 2 images) are well clear.

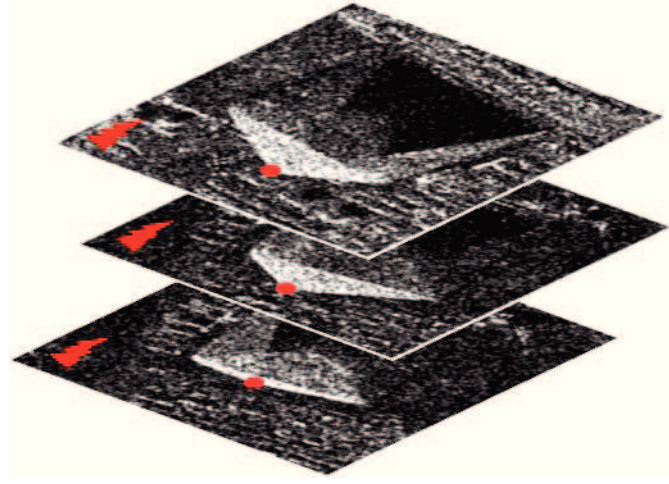


Fig. 42 – Multi-image space triangulation

A larger number of observation equations can reduce the final result uncertainty. Obviously, it would be really important to carefully take into account the process to associate homologous points among different images, especially if different look sides have been chosen: this aspect will be analyzed in the following.

Eq. 25 describes the extended model:

$$\begin{cases} F_1 = \frac{2}{\lambda R_{sr_1}} (\vec{R}_{s_1} - \vec{R}_t) \cdot \vec{V}_{s_1} = v_1 \\ \vdots \\ F_n = \frac{2}{\lambda R_{sr_n}} (\vec{R}_{s_n} - \vec{R}_t) \cdot \vec{V}_{s_n} = v_n \\ F_{n+1} = R_{sr_1} - |\vec{R}_{s_1} - \vec{R}_t| = v_{n+1} \\ \vdots \\ F_{2n} = R_{sr_n} - |\vec{R}_{s_n} - \vec{R}_t| = v_{2n} \end{cases} \quad \text{Eq. 25}$$

where, for the n images:

- R_{sr_i} = is the target slant range measurement;
- \vec{R}_{s_i} = spacecraft position for the i^{th} image;
- \vec{V}_{s_i} = spacecraft velocity for the i^{th} image.

These $2n$ equations of Eq. 25 are used to form the normal equation of Eq. 26; as already said, the sum of the squares must be minimized to obtain the location of the target:

$$\sum_{i=1}^{2n} v_i^2 \rightarrow \min \quad \text{Eq. 26}$$

This problem could be solved by means of a Gauss-Newton approach. Further details about the numerical techniques useful to efficiently solve the problem are in (40).

3.2.5 ERROR BUDGET OF THE TARGET POSITION

Eq. 25 does not provide an explicit formulation of the target position; however the location sensitivities to the input parameters can be evaluated numerically, through a Montecarlo simulation, starting from the equations of the generalized n-images stereo problem.

$$\vec{R}_t = \vec{R}_t(\vec{R}_{s_1}, \dots, \vec{R}_{s_n}, \vec{V}_{s_1}, \dots, \vec{V}_{s_n}, f_{DC_1}, \dots, f_{DC_n}, R_{sr_1}, \dots, R_{sr_n}) \quad \text{Eq. 27}$$

The parameters affected by errors are those reported in Eq. 27. It is reasonable to suppose that, having properly modelled the propagation through the atmosphere, the distribution of each of them will be normal.

In order to properly evaluate the input parameters for the accuracy estimation, the following considerations/assumptions have been taken into account:

- Satellite Position and Velocity Accuracy: nowadays all the major operative SAR satellites have the possibility to work with fast navigation solution orbits and with precise and very precise (also called scientific) orbits. As the data concerning the CSK orbital accuracy cannot be published in this work, the term of reference for the error model will be the TerraSAR-X satellite, of which the system performance are widely published, (32) , (41) and (42);
- Doppler Centroid estimation accuracy: during the processing steps, the doppler centroid is estimated. The accuracy adopted are deduced from the TerraSAR-X case, (32), and therefore they are negligible;
- Atmosphere propagation: in case the atmosphere is not modelled, the measurements would be biased: in fact, the vacuum of space, the ionosphere and the troposphere have different refractive indices causing errors from the path delay of about 2-4 meters (depending on the actual atmospheric conditions and on the length of the path), (41). In this simulation it was assumed that an atmosphere model is adopted, and only a residual of this model remains;
- Ranging errors: the ranging errors are caused by all the possible sources of time delays, including the atmosphere path delay (already analyzed above). If the sensor is properly calibrated, if all the sensor hardware delays are calibrated and if the atmosphere is modelled, the major contributions to ranging errors are due to earth tides, (32). Also numeric approximations lead to small errors (order of magnitude of centimetres).

Tab. 3 summarizes the principal error contributions to the error model, considering a Spotlight sensing mode (for a Stripmap mode, the slant range measurements would be less accurate). Tab. 4 synthesizes the parameters adopted in the Montecarlo simulation.

Parameter	Description	Assumptions	Values [m]
\vec{R}_{si}	Position accuracy, result of the orbit determination	Navigation solution Precise Orbit Determination	Radial (1σ): 0.3 m Along-track (1σ): 0.2 m Cross-track (1σ): 0.2 m Radial (1σ): 0.04 m Along-track (1σ): 0.06 m Cross-track (1σ): 0.05 m
\vec{V}_{si}	Velocity accuracy, result of the orbit determination	Navigation solution Precise Orbit Determination	Radial (1σ): < 0.001 m/s Along-track (1σ): < 1e-5 m/s Cross-track (1σ): < 0.001 m/s Radial (1σ): < 1e-4 m/s Along-track (1σ): < 1e-6 m/s Cross-track (1σ): < 1e-4 m/s
f_{DCi}	Doppler centroid accuracy, result of its estimation	None	Negligible, because of the adopted focusing techniques
R_{sri}	Slant range measurements	Sensor hardware delays calibrated and atmospheric refraction modelled	Ranging errors (1σ): 0.1 ÷ 0.5 m Atmosphere mod. (1σ): 0.1 ÷ 0.3m Numeric errors (1σ): 0.01 ÷ 0.2m

Tab. 3 – Geolocation error contributions for a current operational SAR satellite in case of Spotlight mode acquisition

Parameter	Description	Assumptions	Values [m]
\vec{R}_{si}	Position accuracy, result of the orbit determination	Accurate & fast orbit reconstruction (new generation Satellite GPS)	Radial (1σ): 0.3 m Along-track (1σ): 0.2 m Cross-track (1σ): 0.2 m
\vec{V}_{si}	Velocity accuracy, result of the orbit determination	Navigation solution Precise Orbit Determination	Radial (1σ): 2.2e-4 m/s Along-track (1σ): 1e-6 m/s Cross-track (1σ): 2.2e-4 m/s
f_{DCi}	Doppler centroid accuracy, result of its estimation	None	Negligible, because of the adopted focusing techniques
R_{sri}	Slant range measurements	Sensor hardware delays calibrated and atmospheric refraction modelled	Ranging errors (1σ): 0.3 m Atmosphere mod. (1σ): 0.1m Numeric errors (1σ): 0.02m

Tab. 4 – Geolocation error contributions adopted for the Montecarlo simulation in case of Spotlight mode acquisition

For the Montecarlo simulation, the reference frame of Fig. 43 is introduced. The reference frame is fixed with respect to the target. The y axis is aligned with the sensor velocity (all the velocity vectors have the same direction). The z axis is geocentric, the x axis is chosen to have a positive tern. The orbit of the satellite is locally approximated with a line perpendicular to the xz plane. To conduct a sensitivity analysis, one, two or more satellites (in the example, the two satellites on the left) have a fixed orbit with respect to the reference frame, while one or more satellites have different incidence angles to explore the different possible geometries. The results of the error sensitivity analysis are displayed as a function of this angle, assuming that the height of the satellites is constant.

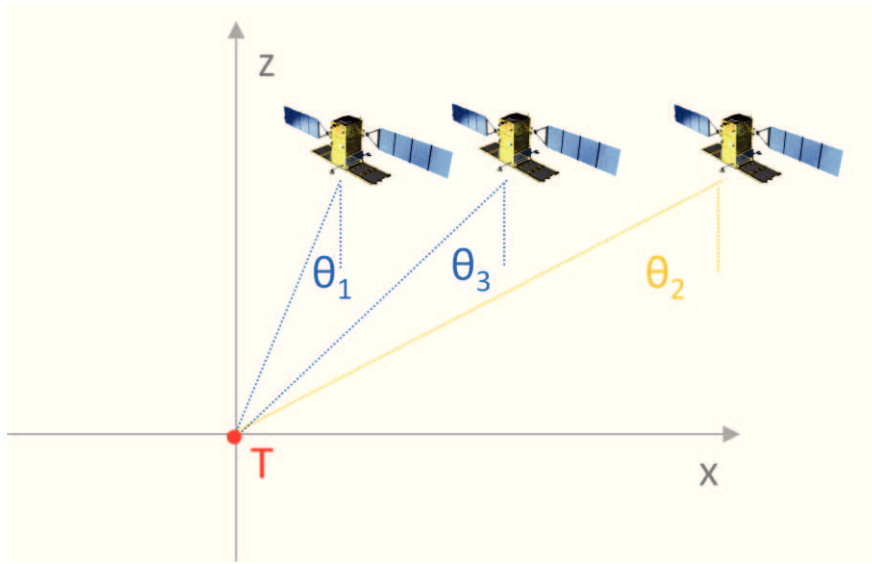


Fig. 43 – The error budget simulation environment: the local reference frame

The technique used to determine the error distribution is the Montecarlo simulation. The error contributions are those explained above, summarized in Tab. 4. The 3D standard deviation error is defined in the following way:

$$\sigma_{err} = \sqrt{\sigma_{err_x}^2 + \sigma_{err_y}^2 + \sigma_{err_z}^2} \quad \text{Eq. 28}$$

with σ_{err_x} , σ_{err_y} , σ_{err_z} the error in the x, y and z directions.

Tab. 5 ÷ Tab. 7 describe the considered cases and geometries. Fig. 44 ÷ Fig. 46 give the schemas of the possible viewing geometries and results in terms of 3D standard deviation of the location error. Considering that the error model does not foresee any bias, the error mean value has been verified to be approximately zero.

Schema	Graph	Description
Left	Solid Red	All the possible combinations of 1 sensing geometry with 20° incidence angle and another one with the incidence angle in the range of $[20^\circ, 50^\circ]$
Left-Central	Dotted Blue	All the possible combinations of 1 sensing geometry with 20° incidence angle and 2 viewing geometries with a constant difference of incidence angle (equal to 5°) and the first one in the range of $[20^\circ, 50^\circ]$
Right-Central	Dashed Black	All the possible combinations of 2 sensing geometries with 20° incidence angle and 2 viewing geometries with the same incidence angle in the range of $[20^\circ, 50^\circ]$
Right	Point Dash Magenta	All the possible combinations of 2 sensing geometries with 20° and 25° incidence angle and 2 viewing geometries with a constant difference of incidence angle (equal to 5°) and the first one in the range of $[20^\circ, 50^\circ]$

Tab. 5 – Input geometries of the Montecarlo simulation of Fig. 44

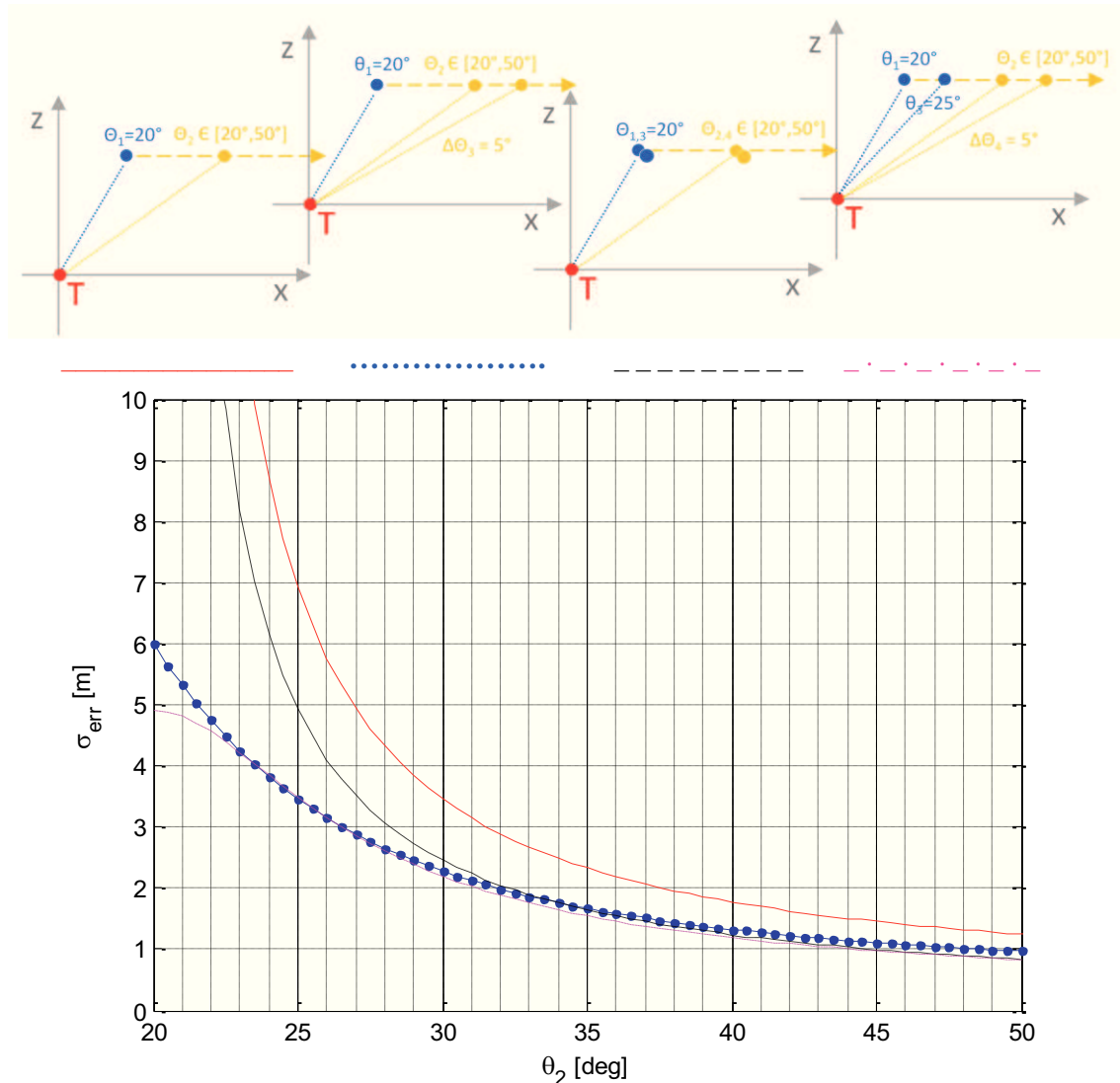


Fig. 44 – Schemas of 4 possible viewing geometries (2 or more observation points) and the relevant standard deviation of the location error

Schema	Graph	Description
Left	Solid Red	All the possible combinations of 1 sensing geometry with 20° incidence angle and one another in the opposite side with the incidence angle in the range of [20°,50°]
Central	Dotted Blue	All the possible combinations of 1 sensing geometry with 20° incidence angle and 2 opposite side viewing geometries with a constant difference of incidence angle (equal to 5°) and the first one in the range of [20°,50°]
Right	Dashed Black	All the possible combinations of 2 sensing geometries with 20° incidence angle and 2 opposite side viewing geometries with the same incidence angle and the first one in the range of [20°,50°]

Tab. 6 – Input geometries of the Montecarlo simulation of Fig. 45

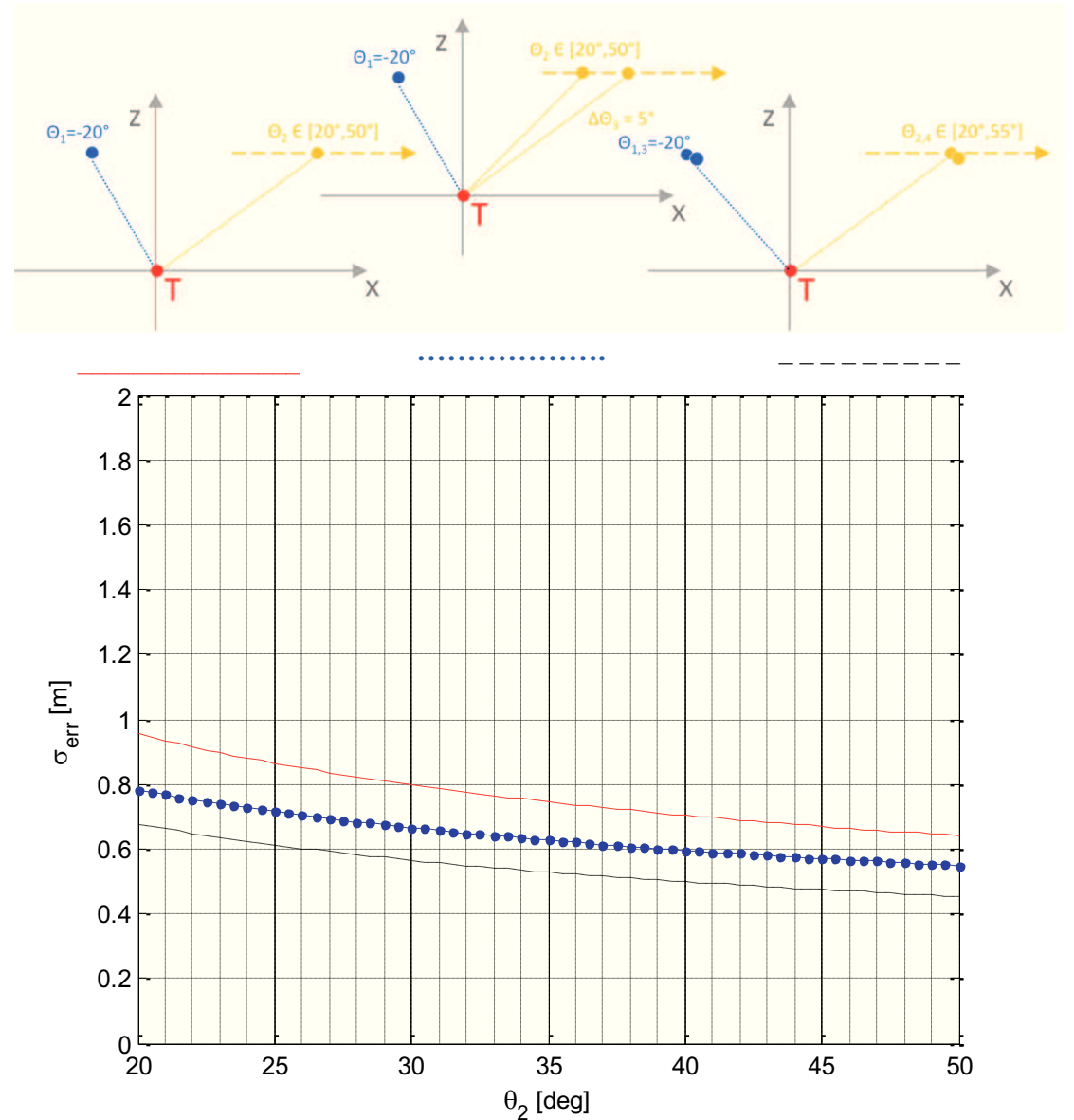


Fig. 45 – Schemas of 3 possible viewing geometries (2 or more observation points) and the relevant standard deviation of the location error

Schema	Graph	Description
Left	Solid Red	All the possible combinations of 1 sensing geometry with 45° incidence angle and one another in the opposite side with the incidence angle in the range of [20°,50°]
Central	Dotted Blue	All the possible combinations of 1 sensing geometry with 45° incidence angle and 2 opposite side viewing geometries with a constant difference of incidence angle (equal to 5°) and the first one in the range of [20°,50°]
Right	Dashed Black	All the possible combinations of 2 sensing geometries with 20° and 45° incidence angles and 1 opposite side viewing geometry with the incidence angle in the range of [20°,55°]

Tab. 7 – Input geometries of the Montecarlo simulation of Fig. 46

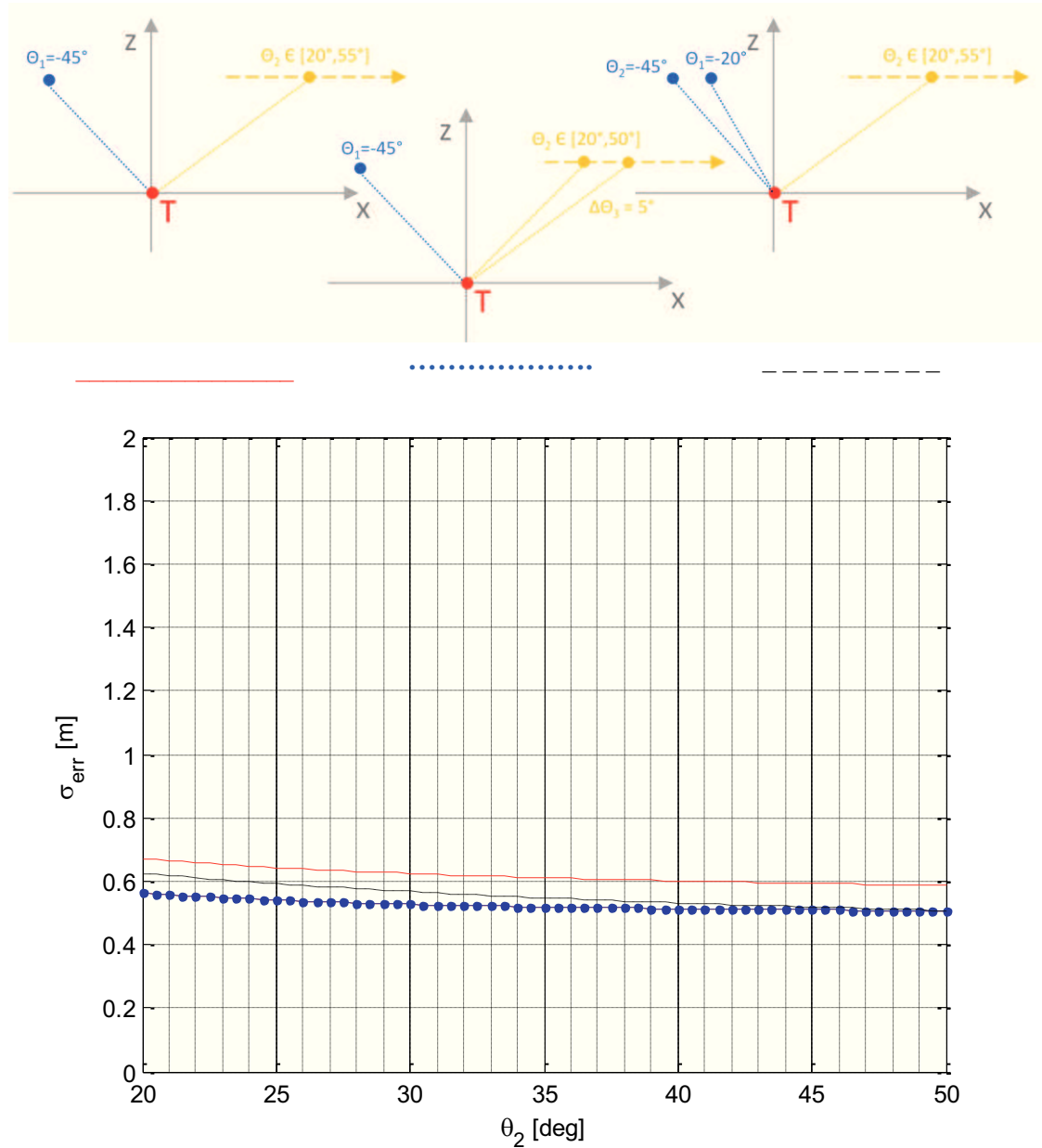


Fig. 46 – Schemas of 3 possible viewing geometries (2 or more observation points) and the relevant standard deviation of the location error

The analysis carried out shows the expected influence of the sensing geometries on the error budget. The following considerations can be stated:

- the simplification of having all the sensing geometries with the same zero doppler plane is consistent with the real space-born sensing condition: in fact, in case of acquisitions performed in the same orbital direction (ascending or descending), the zero doppler planes are almost coincident (even in the case of acquisitions performed in left or right looking conditions, ref. par. 2.2.2.2);
- with respect to the classical radargrammetric technique, if we suppose to exploit the space intersection only in case of deterministic scattering (such as the double bounce scattering), thus avoiding the matching of downgraded patches, the matching problem does not affect meaningfully the results and can be modelled through the error of the ranging measure in each single image; in this case, even for very large incidence angles interval, the results are very good (ref. Fig. 46);
- with reference to Fig. 44, thus considering only the viewing geometries with the same look side, in order to reduce at the maximum extent the error it is necessary to have the maximum separation between the different sensing geometries;
- in order to increase the accuracy for every couple of images available, the comparison of Fig. 45, Fig. 46 and Fig. 48 with respect to Fig. 44 highlights that it would be better to exploit opposite-side geometries. This opportunity requires a more general stereo intersection formulation, in order to be able to exploit the deterministic scattering even in opposite-side geometries. In fact, the deterministic scattering phenomenon, such as the single or double bounce as well as the trihedral backscattering, cannot be seen from opposite-side geometries. These considerations push towards the new approach described in paragraph 3.3;
- in order of magnitude, the location accuracy obtained in the simulations are consistent with the geolocation accuracy of the COSMO-SkyMed and TerraSAR-X systems certified by the National Geospatial-Intelligence Agency (NGA), (43) and (44);
- this method would directly benefit from an increase in accuracy obtained by means of new geolocation models, as explained in (32).

3.3 MULTI-ASPECT FEATURE BASED SPACE INTERSECTION

In the previous paragraph the classical radargrammetric process is explained, as well as the more general model for space intersection (or triangulation) with n-images. Summarizing the most important concepts:

- radargrammetry is a technique that exploits the triangulation principle in order to determine the pixels elevation values, having associated corresponding patches/pixels between the two images; it works when images are acquired with:
 - o the same orbit direction and look side and different incidence angles, (2);
 - o the same orbit direction and opposite-side viewing geometries, through a degradation of the input images in order to allow the matching of analogous patches, (3);
- space intersection (or triangulation) is the general theory that allows to determine the 3D geospatial coordinates of a point having recognized it in a set of images acquired with any viewing geometry.

Theoretically, space intersection allows to exploit any possible viewing geometry of the target; in order to proceed in this way it is necessary to take into account that (i) it is difficult to identify the same features within images acquired with different viewing geometries; (ii) point scatterers are usually dihedral or trihedral features that can only be observed from the same orbit direction and look side (see paragraph 2.2.2 and 2.2.4).

For that reason, it could be interesting trying to extend the radargrammetric and space intersection theory taking into account the approaches existing in literature to extract features from SAR images:

- building reconstruction from multi-aspect SAR images exploiting the layover induced shifts. Buildings are observed as bright parallelograms of varying locations and orientations from four points of view and the Hough transform is used to identify parallel lines, (5);
- radiometric approaches based on a scattering model for the retrieval of the buildings features and height, (45);
- the joint use of high-resolution optical and SAR data for building extraction and 3D reconstruction in large urban areas, (46);

Other interesting approaches in literature show that:

- SAR stereo is not limited to same side and opposite-side images; e.g. the height of a building can be determined by high resolution SAR images taken from orthogonal flight paths, (47);
- taking into account same-side images and considering the building modelled as bright L-shaped angular structures caused by strong dihedral returns, the higher difference of the viewing angle gives smaller mean error in altimetry, but fewer buildings are recognized (48), (4).

The approach I will follow in this thesis will be the extension of the mathematical model of the stereo space intersection, enabling the matching of images based on the same features, seen from different views. Therefore, the matching, instead of being based on a “patch matching”, is “feature based”: it requires the identification, for each image, of point scatterers belonging to the same geometric feature. For example, if we consider the matching of several high resolution images in correspondence with a circular shaped building, radargrammetric state-of-art techniques search for the local matching of small patches extracted from the images. This would be not feasible with opposite-side images and very difficult for same-side images when the viewing angle is too different because of the layover effect (predominant in case of high resolution images). On the other hand, if it is possible to detect points belonging to the dihedral backscattering effect at the base of the external surface (see paragraph 2.2.4.2) and it is possible to model the building as a circle, the matching condition can become the belonging of these dihedral points to the circular geometric model. In this way it is possible to modify the space intersection problem taking into account the geometric model of the matching feature. This example shows how this approach will offer more space intersection opportunities.

Therefore the research will focus on simple geometries, as circular or linear ones, that can be used to model:

- cylindrical buildings;
- simple rectangular-shaped buildings;
- towers.

The first objective will be to develop a specific model for circular geometries.

The proposed approach will be analyzed taking into account the following criteria:

- improvement of complex geometry reconstruction and 3D features extraction;

- increase of interoperability with electro-optical images.

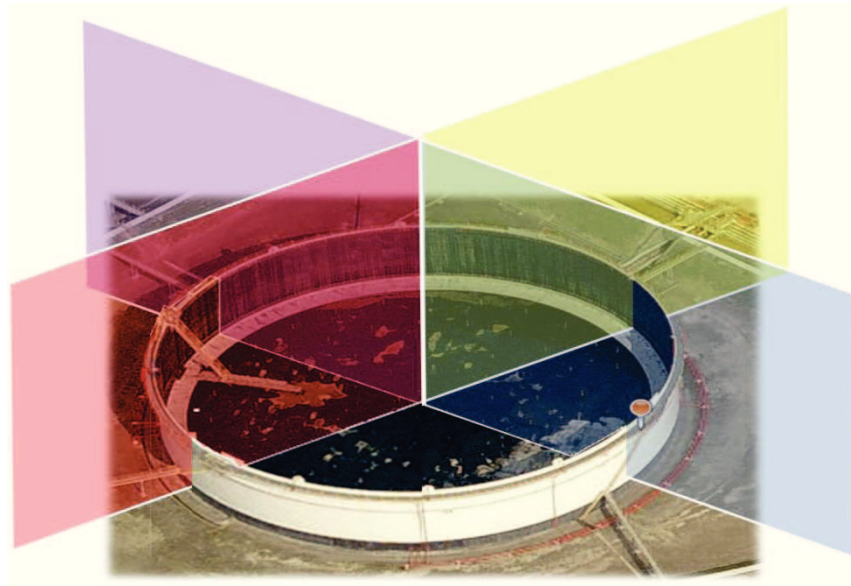


Fig. 47 – Multi-aspect space intersection for circular shape: the 4 planes shows the possible combinations of orbit directions, looks side and look angle

3.3.1 MULTI-ASPECT FEATURE BASED SPACE INTERSECTION FOR CIRCULAR FEATURES

3.3.1.1 A geometric model for circular geometries

First of all, a general model to describe a circular geometry is introduced. The circular shape represents a specific subclass of the more general cylindrical model. This generic model, depicted in Fig. 48, foresees different real features, all derived from a real target (see Fig. 47):

- a cylindrical external surface, with a constant height “ h ” and diameter “ d ”, characterized by an “external double bounce” (or dihedral) scattering point “ B ” at the base of the external surface;
- a “ring” at the top of the cylindrical surface, whose size is “ a ” (a more general model with a ring at a different height can be adopted); this ring determines an “upper single bounce” (or direct) scattering point “ L ” (upper side) and a “triple bounce” (or multipath) scattering point “ V ” (lower side of the ring);
- an inner roof, fixed or floating, whose height is “ t ”, generating with the external surface an “inner double bounce” (or dihedral) scattering point “ T ”;
- the virtual central point “ C ”, representing the centre of the base circle.

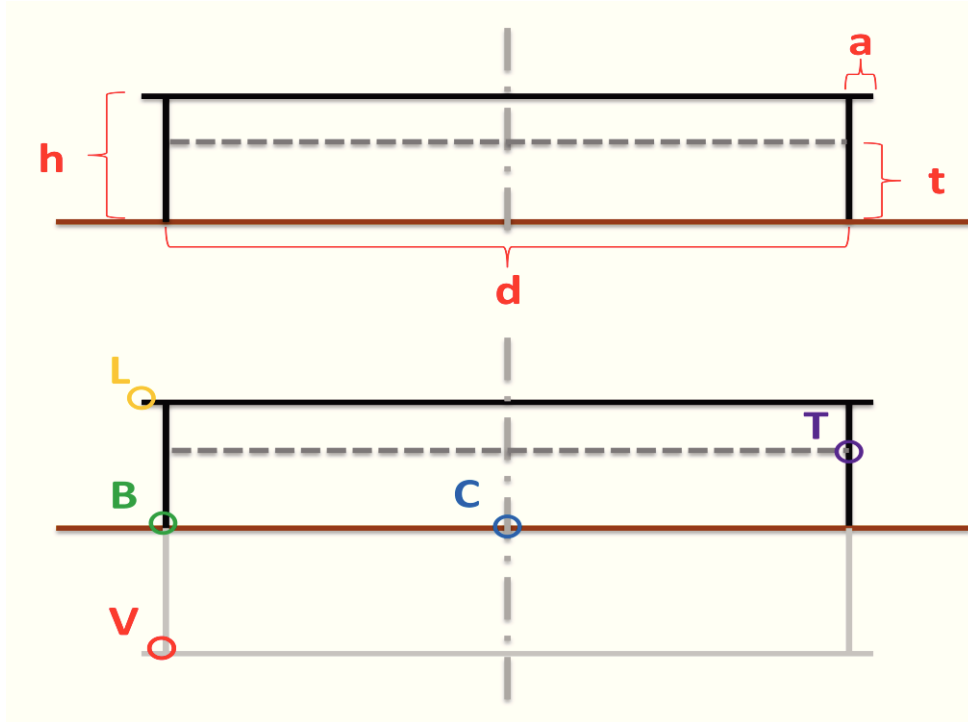


Fig. 48 – General model for a cylindrical/circular geometry

From this model, it is possible to compute the slant range value of the “range equation” (Eq. 17) taking into account that:

- the real points that will be visible in the SAR image would be the L, T & B points;
- there will be a backscattering for the virtual point V;
- the space intersection problem will be addressed for the point C.

In the following, the “slant range” relations linking the different points with the central point C are derived:

1. External Double Bounce scattering point B (real)

The external double bounce point B is linked to the virtual central point C by the following relation, as depicted in Fig. 49:

$$R_C = R_B + \frac{d}{2} \sin \theta \quad \text{Eq. 29}$$

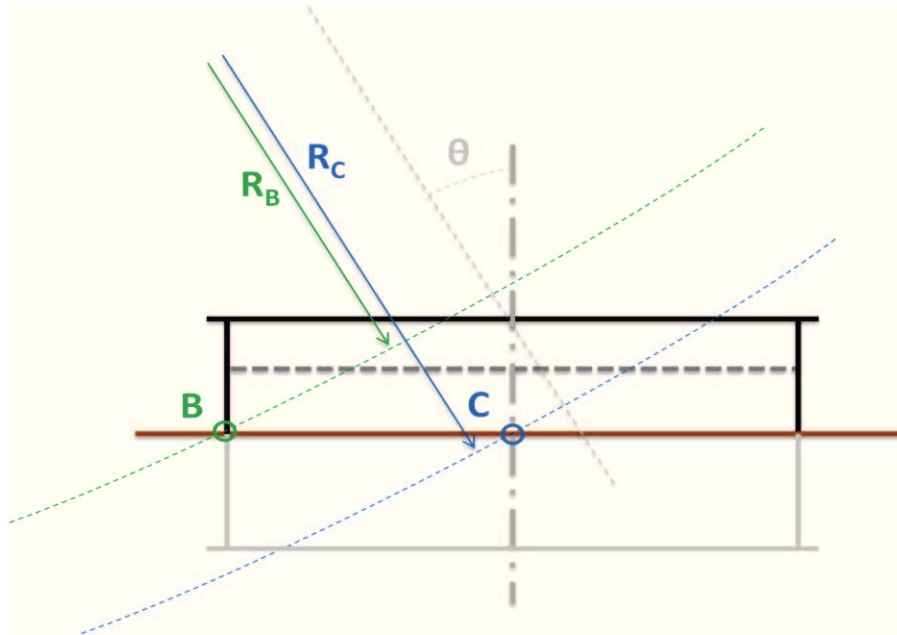


Fig. 49 – Link between the double bounce point B and the virtual central point C

2. Upper Single Bounce scattering point L (real)

The upper single bounce point L is linked to the virtual central point C by the following relation, as depicted in Fig. 50:

$$R_C = R_L + \left(\frac{d}{2} + a \right) \sin \theta + h \cos \theta \quad \text{Eq. 30}$$

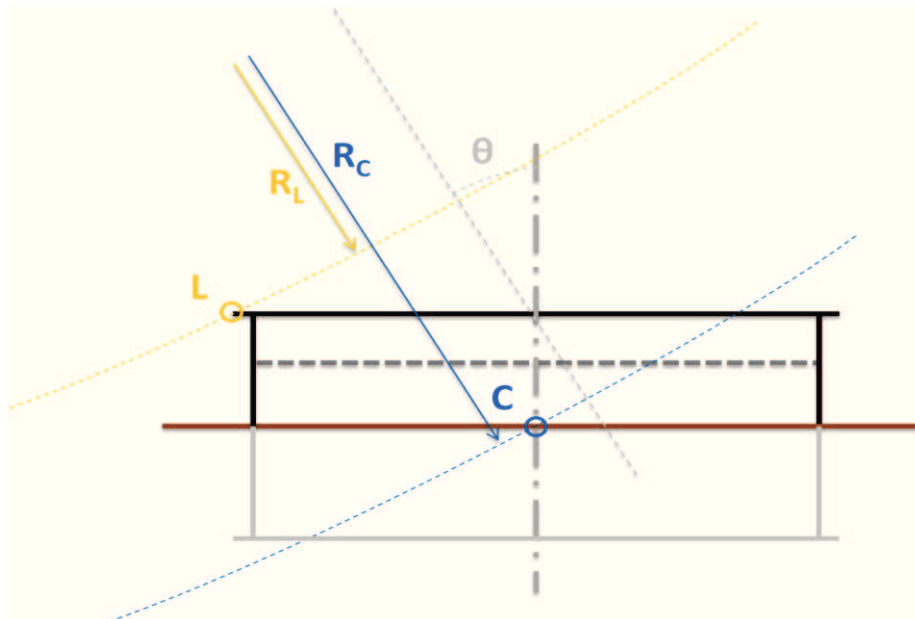


Fig. 50 – Link between the upper single bounce point L and the virtual central point C

3. Triple Bounce scattering point V (virtual)

The virtual triple bounce point V is linked to the virtual central point C by the following relation, as depicted in Fig. 51:

$$R_C = R_V + \frac{d}{2} \sin \theta - h \cos \theta \quad \text{Eq. 31}$$

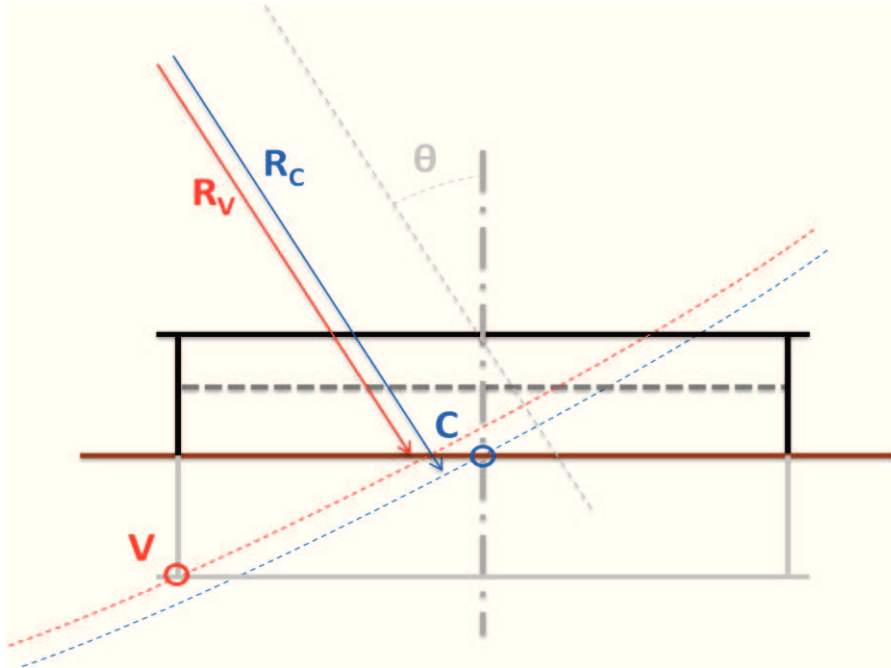


Fig. 51 – Link between the virtual triple bounce point V and the virtual central point C

4. Inner Double Bounce point T (real)

The inner double bounce point T is linked to the virtual central point C by the following relation, as depicted in Fig. 52:

$$R_C = R_T - \frac{d}{2} \sin \theta + t \cos \theta \quad \text{Eq. 32}$$

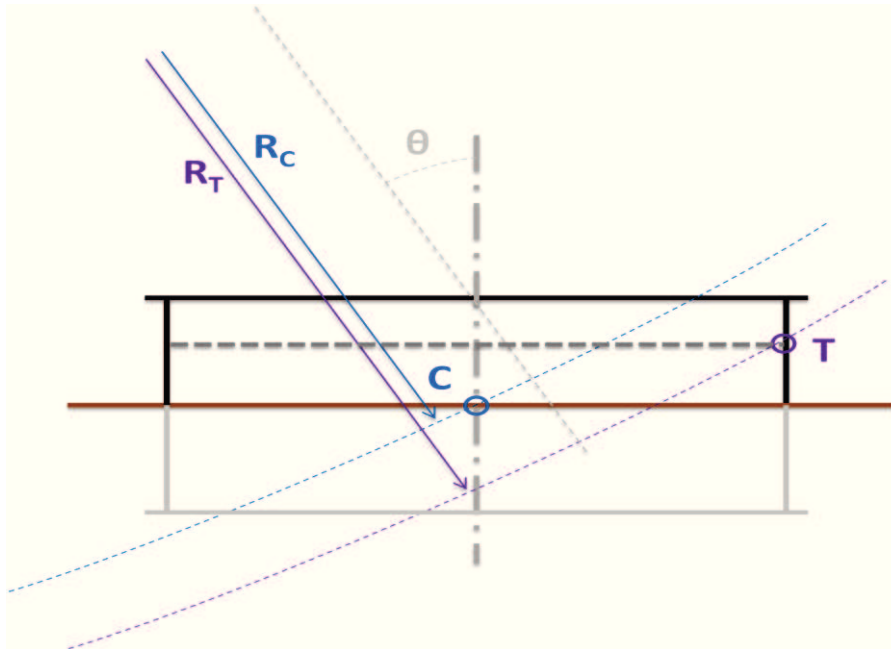


Fig. 52 – link between the inner double bounce point T and the virtual central point C

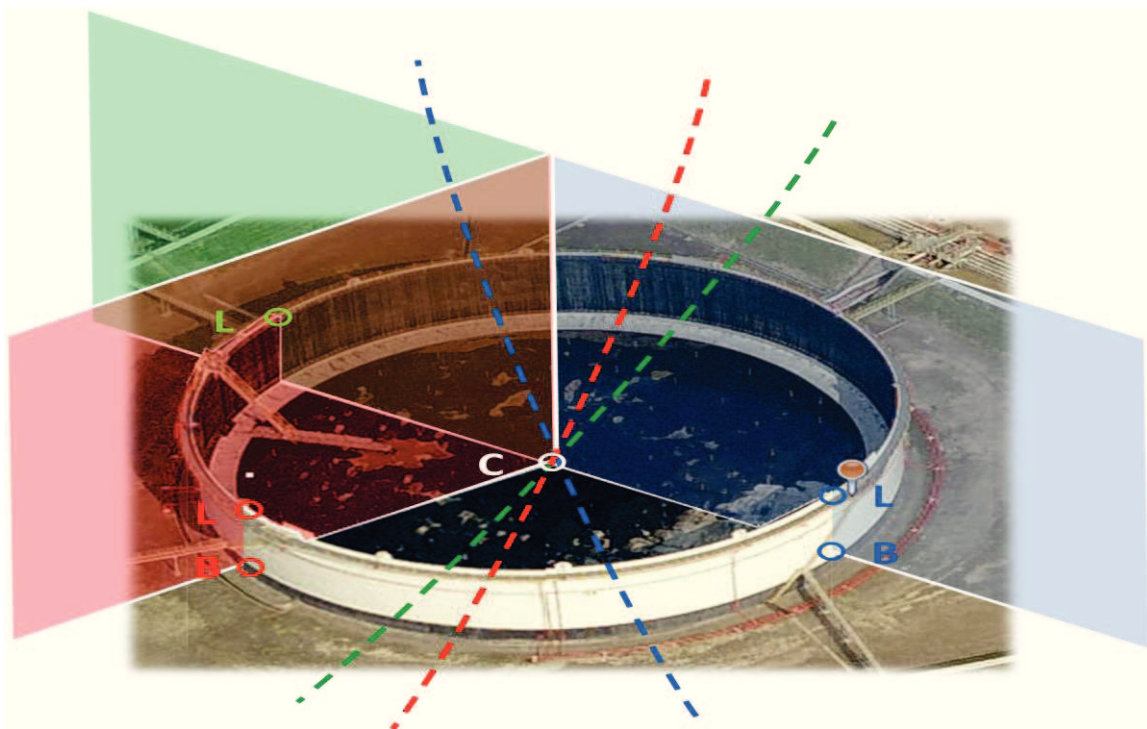


Fig. 53 – The adaptation of the model to the real case presented in Fig. 47

While B, L, V and T point could even be extracted exploiting other state-of-art stereo methods, the virtual point C, that has no real backscattering, is a peculiar result of the feature based space intersection. A complete end-to-end validation of the proposed phenomenology is provided in paragraph 4.2.

3.3.1.2 A space intersection model for circular geometries

In the case of a simple circular model, the following conditions can be considered:

- “doppler equations”: it is possible to impose the belonging of the C point to the same doppler cone/plane of each B point for each image (isodoppler condition);
- “range equations”: the range of the C point is obtained from the range of the B points through Eq. 29;

$$\left\{ \begin{array}{l} F_1 = f_{DC_{B_1}} - \frac{2}{\lambda (R_{sr_{B_1}} + d/2 \sin \theta_{B_1})} (\vec{R}_{s_{B_1}} - \vec{R}_C) \cdot \vec{V}_{s_{B_1}} = v_1 \\ \vdots \\ F_n = f_{DC_{B_n}} - \frac{2}{\lambda (R_{sr_{B_n}} + d/2 \sin \theta_{B_n})} (\vec{R}_{s_{B_n}} - \vec{R}_C) \cdot \vec{V}_{s_{B_n}} = v_n \\ F_{n+1} = R_{sr_{B_1}} + d/2 \sin \theta_{B_1} - |\vec{R}_{s_{B_1}} - \vec{R}_C| = v_{n+1} \\ \vdots \\ F_{2n} = R_{sr_{B_n}} + d/2 \sin \theta_{B_n} - |\vec{R}_{s_{B_n}} - \vec{R}_C| = v_{2n} \end{array} \right. \quad \text{Eq. 33}$$

In order to adopt this model, it is necessary to identify the B point in every image of the dataset.

If a more general approach to model complex objects is necessary or it is not possible to identify the B point in the desired images (see the previous paragraph), the following system of Eq. 34 can be adopted:

$$\left\{ \begin{array}{l} F_1 = f_{DC_{B_1}} - \frac{2}{\lambda (R_{sr_{B_1}} + d/2 \sin \theta_1)} (\vec{R}_{s_1} - \vec{R}_C) \cdot \vec{V}_{s_1} = v_1 \\ \vdots \\ F_n = f_{DC_{B_n}} - \frac{2}{\lambda (R_{sr_{B_n}} + d/2 \sin \theta_n)} (\vec{R}_{s_n} - \vec{R}_C) \cdot \vec{V}_{s_n} = v_n \\ F_{n+1} = R_{sr_{B_1}} + d/2 \sin \theta_1 - |\vec{R}_{s_1} - \vec{R}_C| = v_{n+1} \\ \vdots \\ F_{2n} = R_{sr_{B_n}} + d/2 \sin \theta_n - |\vec{R}_{s_n} - \vec{R}_C| = v_{2n} \\ F_{2n+1} = R_{sr_{L_1}} + (d/2 + a) \sin \theta_1 + h \cos \theta_1 - |\vec{R}_{s_1} - \vec{R}_C| = v_{2n+1} \\ \vdots \\ F_{3n} = R_{sr_{L_n}} + (d/2 + a) \sin \theta_n + h \cos \theta_n - |\vec{R}_{s_n} - \vec{R}_C| = v_{3n} \\ F_{3n+1} = R_{sr_{V_1}} + d/2 \sin \theta_1 - h \cos \theta_1 - |\vec{R}_{s_1} - \vec{R}_C| = v_{3n+1} \\ \vdots \\ F_{4n} = R_{sr_{V_n}} + d/2 \sin \theta_n - h \cos \theta_n - |\vec{R}_{s_n} - \vec{R}_C| = v_{4n} \end{array} \right. \quad \text{Eq. 34}$$

The model contains the following conditions:

- up to $2n$ Range-Doppler equations for the C point based on B points observations (isodoppler + Eq. 29)
- up to $2m$ Range-Doppler equations for the C point based on L points observations (isodoppler + Eq. 30)
- up to $2p$ Range-Doppler equations for the C point based on V points observations (isodoppler + Eq. 31)

The expression “up to” wants to underline that it is not necessary to be able to recognize the single features in each image, having guaranteed the minimum number of conditions necessary to close the problem.

The proposed formulation has many strengths:

- it allows the match between images acquired in any of the available geometries, optimizing the usage of the already acquired images;
- it is possible to exploit, at the same time and in a unique and integrated process, the information coming from different scattering mechanisms (one or more for each geometry);
- the final objective of the study is the total geometry reconstruction of the target in the three dimensional domain;
- large bistatic angles and different viewing geometries give the possibility to acquire the best geometric configuration not to amplify the errors (see paragraph 3.3.1.4).

3.3.1.3 Refinement of the model in case of zero doppler processing

Usually SAR Single Look Complex images, as well as the COSMO-SkyMed ones, are zero doppler focused. When defining the doppler conditions for the C point, it is necessary to take into account that the C point belongs to the doppler cone (the blue line of Fig. 54).

An approximation, that works well in almost every conditions, is to consider the belonging of the C point to the doppler plane of the zero doppler processed images, as the angle between the doppler plane and the doppler cone is negligible. On the other hand, if necessary, the rigorous management of this geometry requires a correction taking into account the real viewing condition adopted during the sensing, therefore it is necessary to consider the doppler cone instead of the zero doppler plane (the zero

doppler azimuth times of the B and C points are different, while the real acquisition times would be the same).

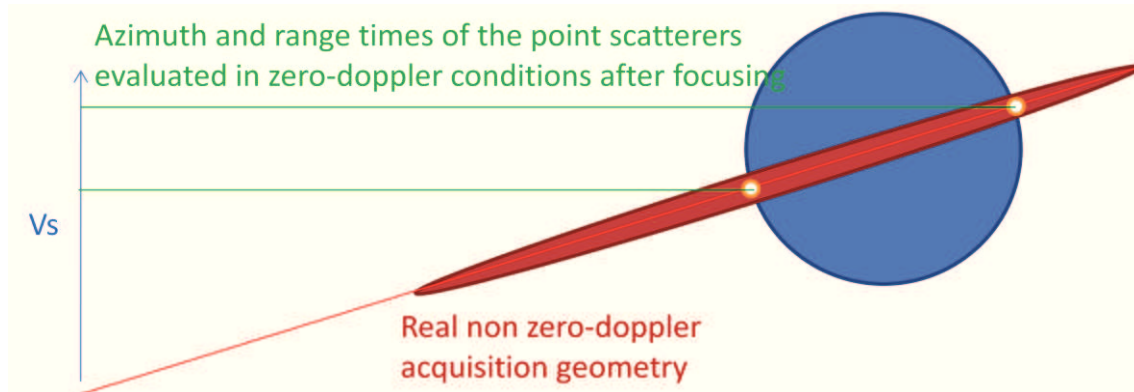


Fig. 54 – The C point belongs to the same doppler cone of the B point

3.3.1.4 Error budget

The error budget presented in this paragraph is an extension of the previous model of paragraph 3.2.5. It has been introduced for two main reasons:

- characterizing and understanding the behaviour of the multi-aspect space intersection;
- giving an instrument to properly choose the best images combination, if more than 2 images are available.

Considering the above aims, two different methodologies are adopted:

- the first one foresees a simplified but meaningful environment of simulation, aiming at understanding both the accuracy level and the best geometries, through a sensitivity analysis;
- the second one, which can be useful before exploiting real images, is based on the real acquisition geometries of the input images.

For the first aim, the reference frame of Fig. 55 is introduced. The reference frame is fixed with respect to the target. The orbit of the satellite is locally approximated with a line. To conduct a sensitivity analysis, one, two or more satellites (in the example, the two satellites on the left) have a fixed orbit with respect to the reference frame, while one or more satellites move around the z axis to explore the different possible geometries. In fact, in function of the latitude of the target, the possible angles among the satellite ground tracks are different. The satellite sensing geometry is defined by means of the incidence angle θ (that in case of flat earth coincide with the look angle)

and the azimuth angle Ω . The results of the error sensitivity analysis are displayed as a function of these angles, assuming that the height of the satellites is constant.

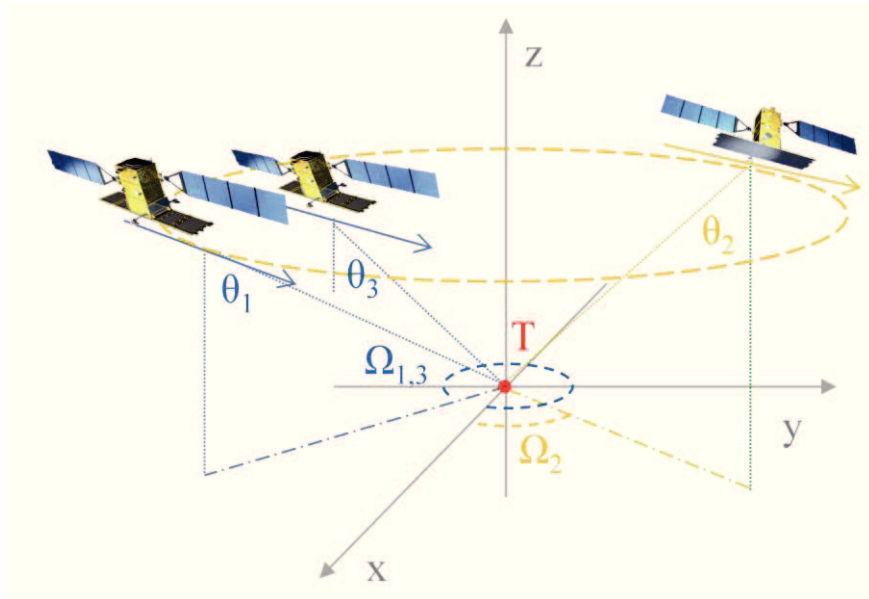


Fig. 55 – The error budget simulation environment: the local reference frame

To properly select significant Ω values for the simulations, it is useful to understand how it varies as a function of the latitude of the target and of the viewing geometry. First of all, it is necessary to link the viewing angle Φ (or look angle) with the angle comprised by the satellite and the target ECEF positions, β (see Fig. 56).

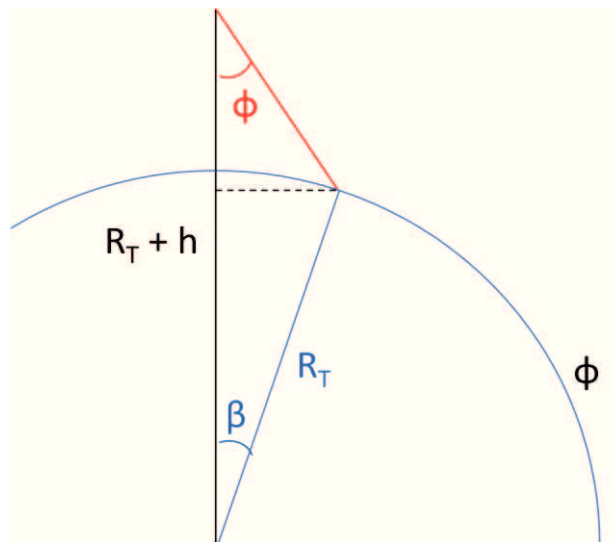


Fig. 56 – Relation between the look angle and the angle comprised by the ECEF satellite and target position vectors

Eq. 35 describes the condition that can be derived from Fig. 56:

$$\sin(\beta + \Phi) = \sin\Phi \frac{R_T + h}{R_T} \quad \text{Eq. 35}$$

where R_T is the earth radius and h is the average height of the satellite.

The previous equation can be rewritten in the following form:

$$\beta = \arcsin\left(\frac{R_T + h}{R_T} \sin\varphi\right) - \varphi \quad \text{Eq. 36}$$

Now, considering Fig. 57, it is possible to analyze two different spherical triangles, depicted using the Nepero mnemonic rule, in order to link the Ω angle with the latitude of the target and the viewing geometries (here represented by the β angle).

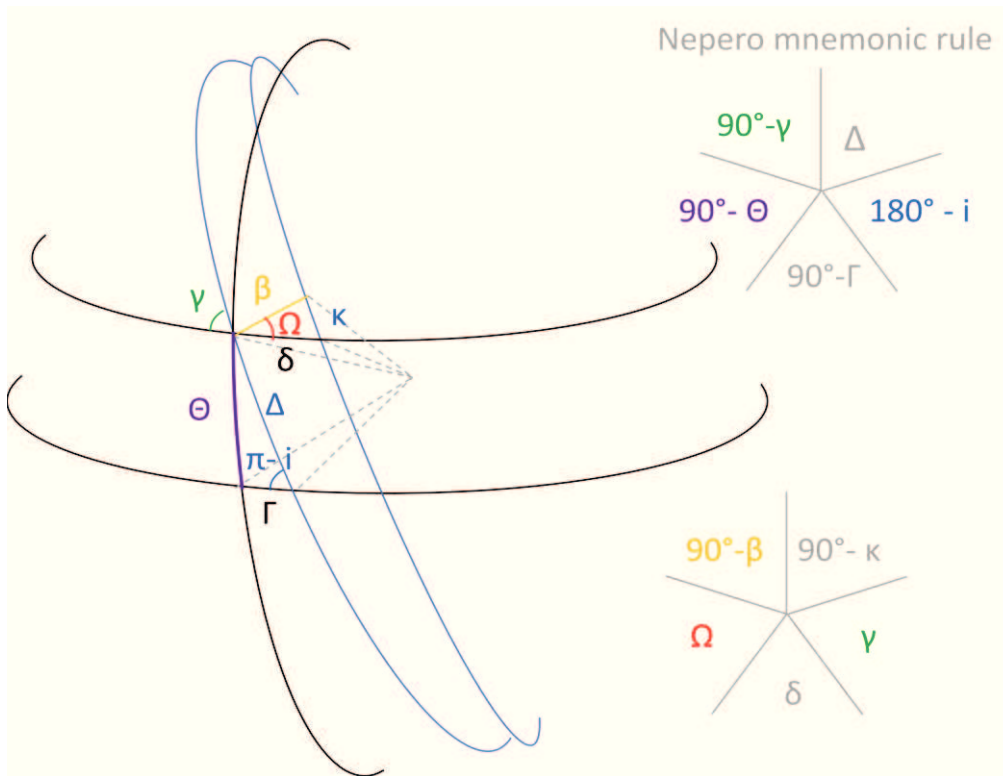


Fig. 57 – Ω in function of the target latitude and the viewing look angle

The first spherical triangle gives the following relation:

$$\cos(\pi - i) = \sin\left(\frac{\pi}{2} - \theta\right) \sin\left(\frac{\pi}{2} - \gamma\right) \quad \text{Eq. 37}$$

where:

CHAPTER 3 - Theory and Implementation

- i represents the inclination of the orbit with respect to the equatorial plane;
- Θ is the target latitude;
- γ represents the inclination of the orbit with respect to the target isolatitude plane.

The above equation can be simplified in the following way:

$$\cos \gamma = \frac{-\cos i}{\cos \Theta} \quad \text{Eq. 38}$$

The second spherical triangle gives the following relation:

$$\cos \gamma = \sin \Omega \sin \left(\frac{\pi}{2} - \beta \right) \quad \text{Eq. 39}$$

Therefore, exploiting both Eq. 38 and Eq. 39, the following equation is obtained:

$$\Omega = \arcsin \left(\frac{-\cos i}{\cos \Theta \cos \beta} \right) \quad \text{Eq. 40}$$

Selecting different viewing angles (that means different β angles), it is possible to plot the Ω angle as a function of the latitude Θ . Fig. 58 shows the variation of Ω as a function of the latitudes for two look angles of 25° and 55° ; Fig. 59 shows the $\Delta\Omega$.

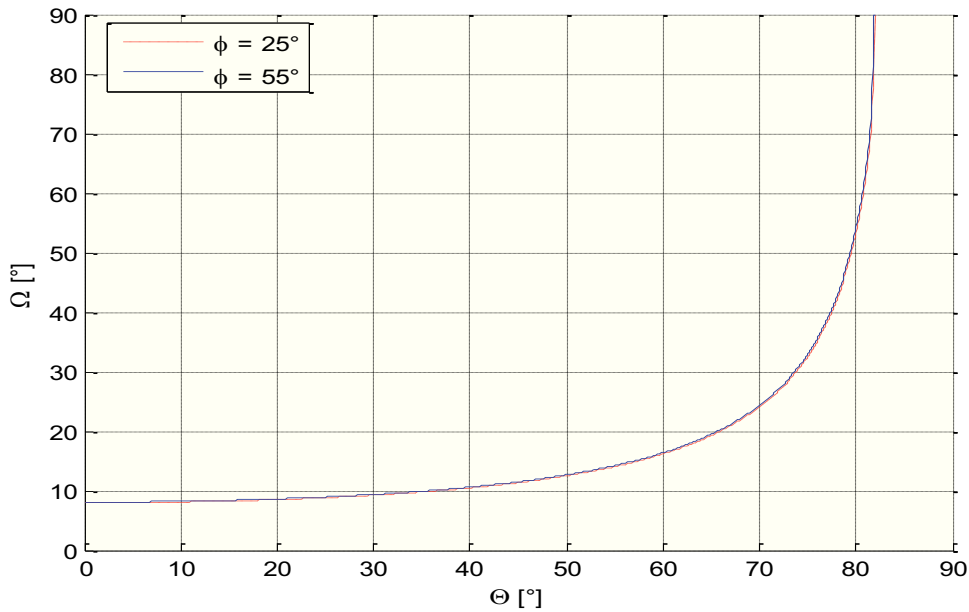


Fig. 58 – Ω in function of the target latitude Θ for Φ equal to 25° and 55°

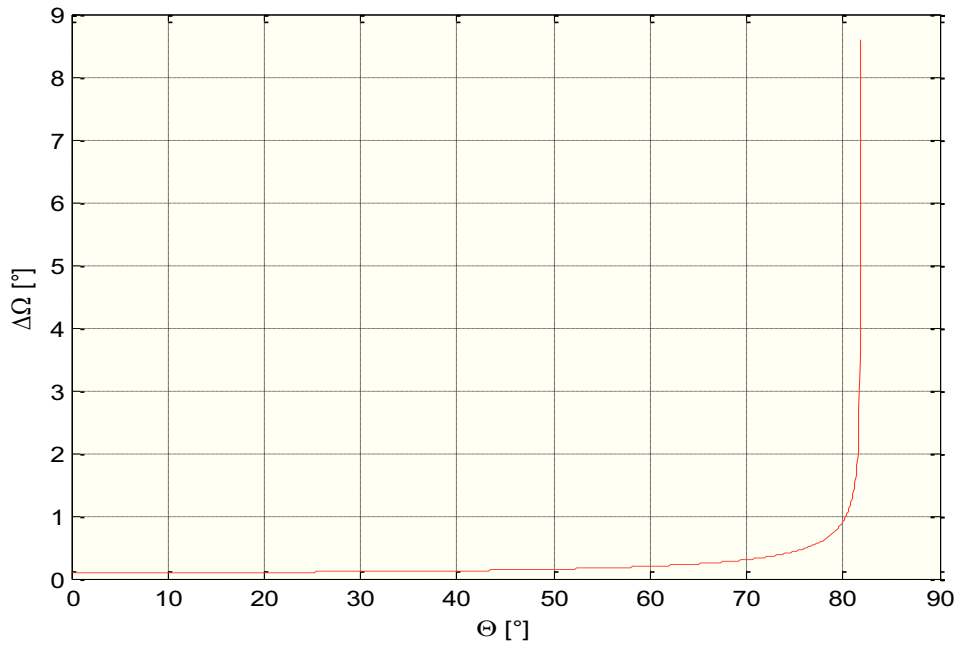


Fig. 59 – $\Delta\Omega$ in function of the target latitude Θ for Φ equal to 25° and 55°

Fig. 58 shows that, for a latitude of interest (e.g. Italy), the average Ω angle is of about 10° (that translated into the four combinations of orbit directions and look sides becomes 10° , 170° , 190° and 350°). On the other hand Fig. 59 gives a confirmation that the approximation of coincident doppler planes for the same viewing aspects (only the view angle varies) is appropriate. In any case I will further discuss the results of the simulation hereinafter.

The technique to determine the error distribution is a Montecarlo simulation, as explained in paragraph 3.2.5. The error contributions are the same of the aforementioned method and the parameters of the error model are those of Tab. 3.

Tab. 8 ÷ Tab. 14 describe the considered cases and geometries. Fig. 60 ÷ Fig. 64 give the schemas of the possible viewing geometries and the results, in terms of 3D standard deviation of the location error. Due to the fact that the error model does not foresee any bias, the error mean value has been verified to be zero.

Schema	Graph	Description
Left	Solid Red	All the possible combinations of 2 sensing geometries both with 25° incidence angle
Central	Dotted Blue	All the possible combinations of 2 sensing geometries having respectively 25° and 45° incidence angle
Right	Dashed Black	All the possible combinations of 2 sensing geometries both with 45° incidence angle

Tab. 8 – Input geometries of the Montecarlo simulation of Fig. 60

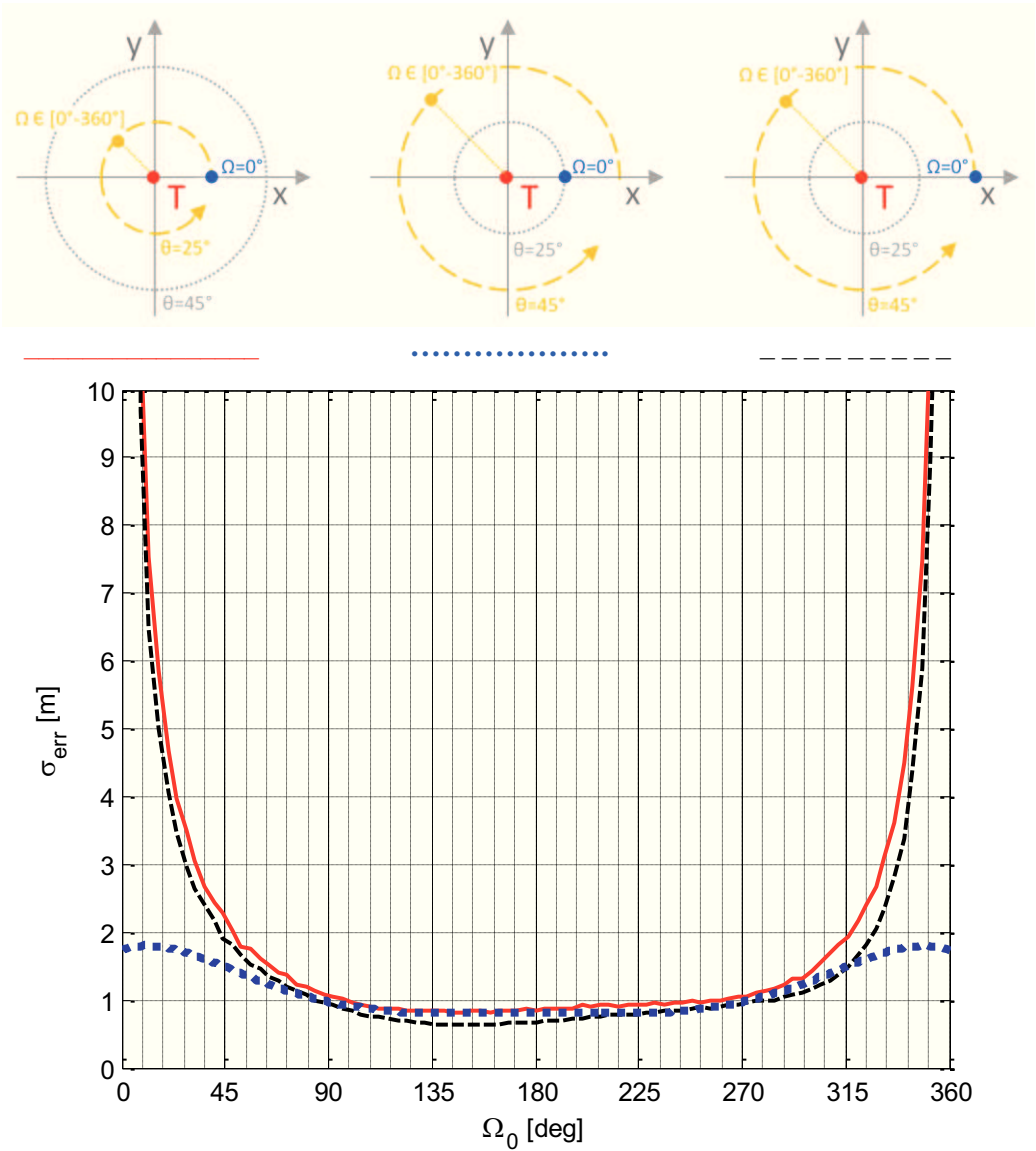


Fig. 60 – Schemas of 3 possible viewing geometries (2 observation points) and the respective standard deviation of the location error

Schema	Graph	Description
Left	Solid Red	All the possible combinations of 2 sensing geometries with the same doppler cone (25° and 45° incidence angle) with respect to a viewing geometry with 45° incidence angle
Central	Dotted Blue	All the possible combinations of 2 sensing geometries with 20° azimuth angle separation (both 25° incidence angle) with respect to a viewing geometry with 45° incidence angle
Right	Dashed Black	All the possible combinations of 2 opposite sensing geometries at 25° incidence angle with respect to a viewing geometry with 45° incidence angle

Tab. 9 – Input geometries of the Montecarlo simulation of Fig. 61

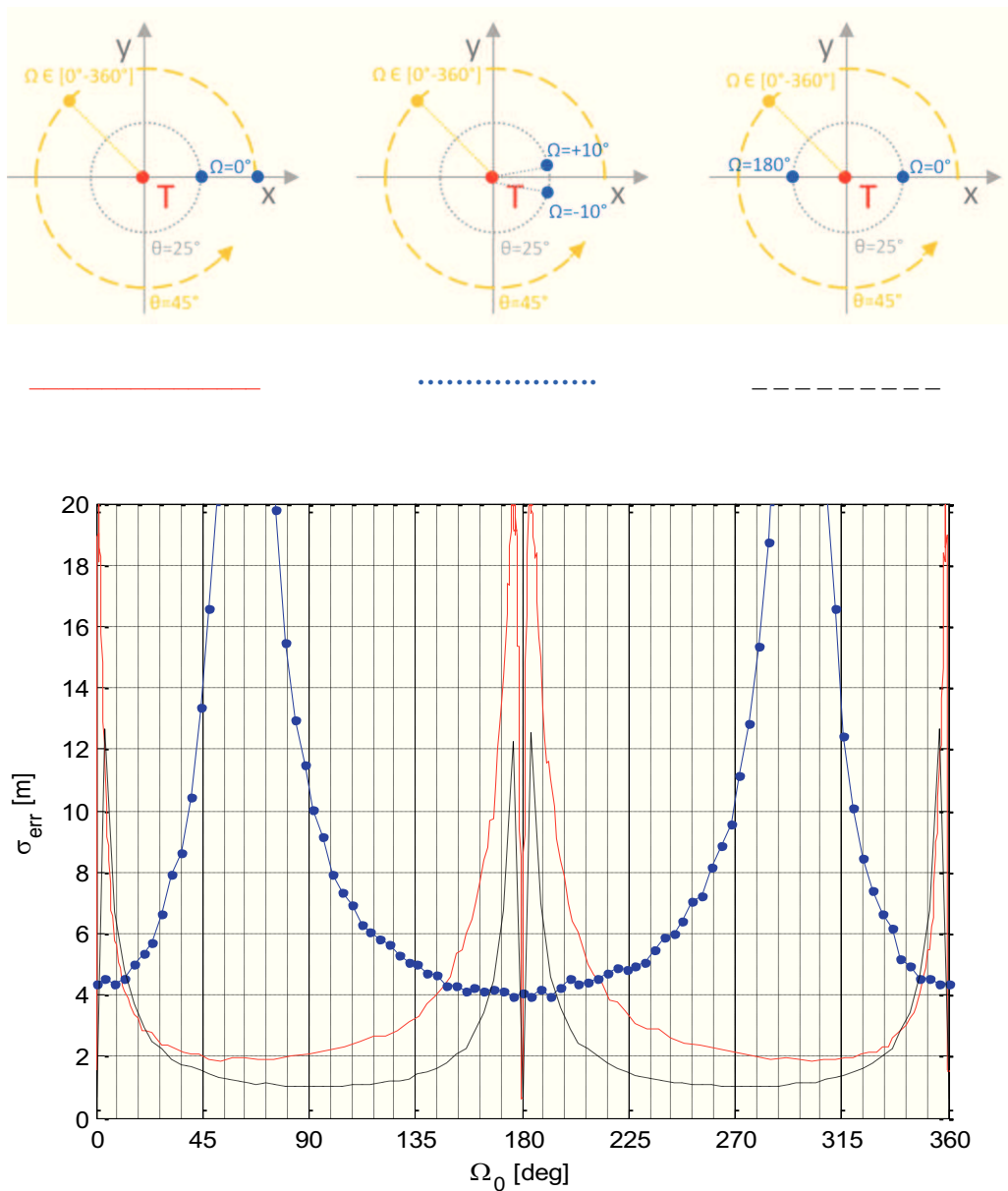


Fig. 61 – Schemas of 3 possible viewing geometries (3 observation points) and the respective standard deviation of the location error

Schema	Graph	Description
Left	Solid Red	All the possible combinations of 2 sensing geometries with same doppler cone (25° and 45° incidence angle) with respect to another sensing geometry with 55° incidence angle
Central	Dotted Blue	All the possible combinations of 2 sensing geometries with 20° azimuth angle separation (one with 25° and one with 45° incidence angle) with respect to another sensing geometry with 55° incidence angle
Right	Dashed Black	All the possible combinations of 2 opposite sensing geometries (one with 25° and one with 45° incidence angle) with respect to another sensing geometry with 55° incidence angle

Tab. 10 – Input geometries of the Montecarlo simulation of Fig. 62

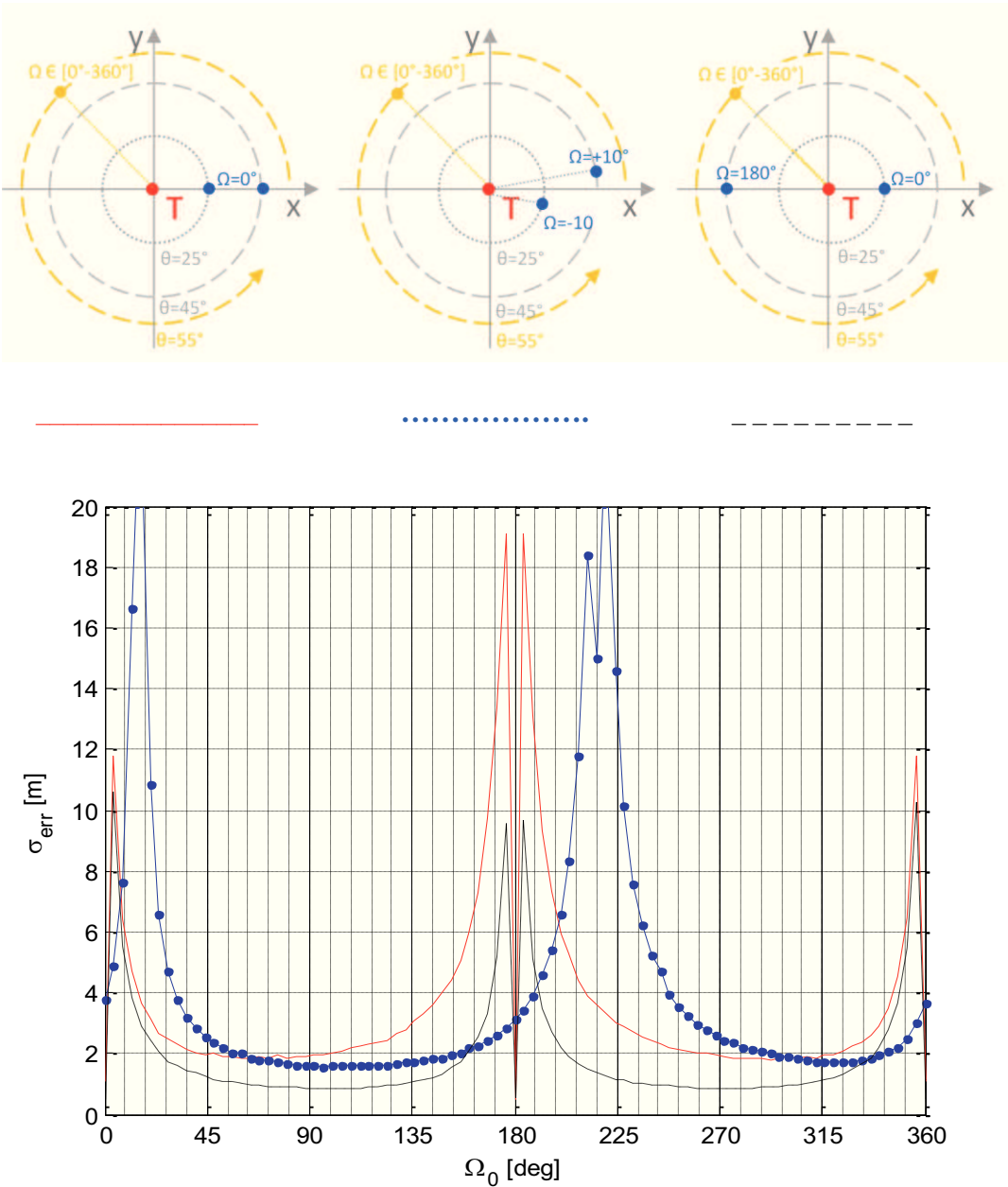


Fig. 62 – Schemas of 3 possible viewing geometries (3 observation points) and the respective standard deviation of the location error

Schema	Graph	Description
Left	Solid Red	All the possible combinations of 2 sensing geometries with same doppler cone (25° and 45° incidence angle) with respect to a other 2 sensing geometries with same doppler cone (25° and 45° incidence angle)
Central	Dotted Blue	All the possible combinations of 2 sensing geometries with 20° azimuth angle separation (both 25° incidence angle) with respect to 2 sensing geometries with the same doppler cone (25° and 45° incidence angle)
Right	Dashed Black	All the possible combinations of 2 opposite sensing geometries at 25° incidence angle with respect to 2 sensing geometries with the same doppler cone (25° and 45° incidence angle)

Tab. 11 – Input geometries of the Montecarlo simulation of Fig. 63

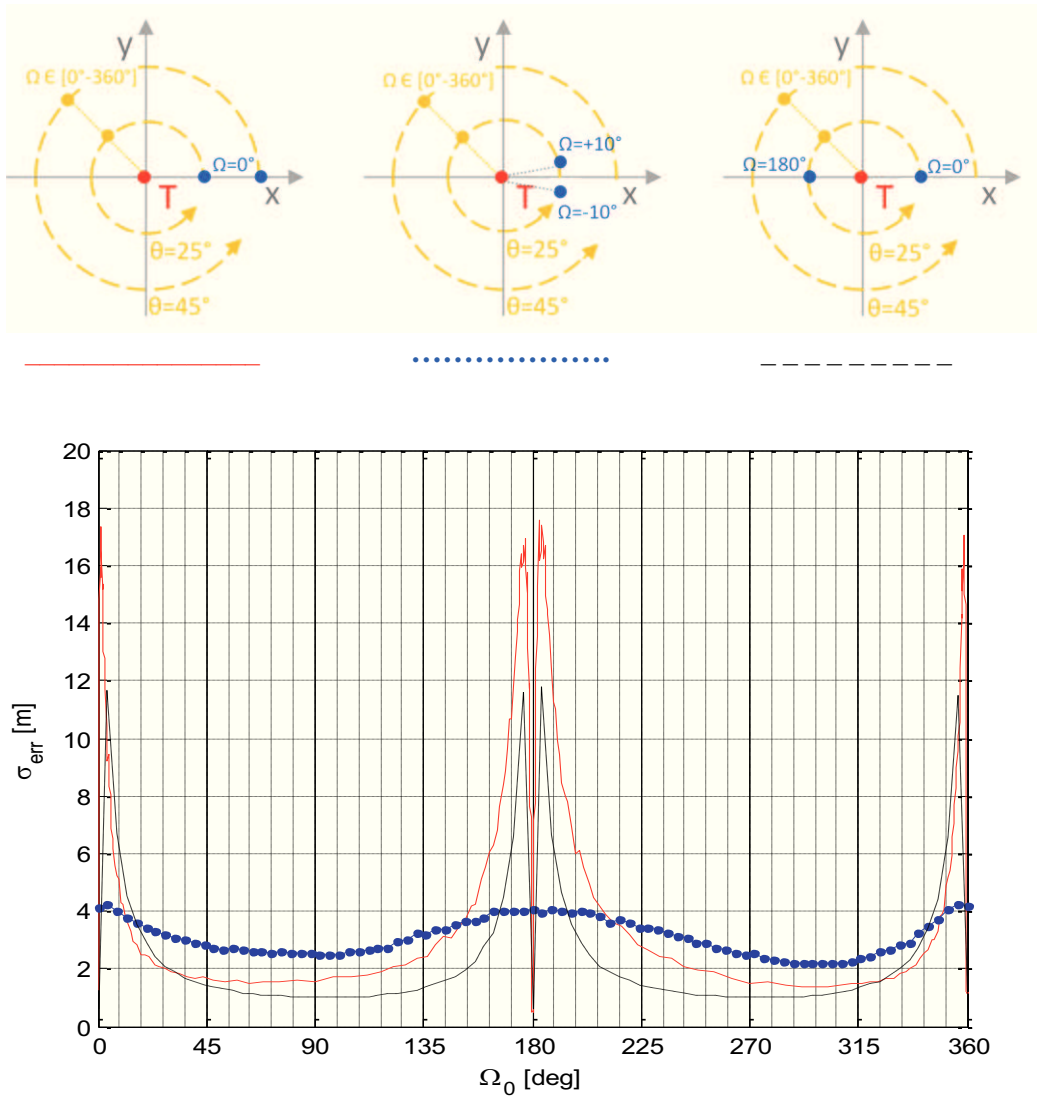


Fig. 63 – Schemas of 3 possible viewing geometries (4 observation points) and the respective standard deviation of the location error

Schema	Graph	Description
Left	Solid Red	All the possible combinations of the same 2 viewing geometries (45° incidence angle) with respect to 2 other sensing geometries (45° incidence angle)
Central	Dotted Blue	All the possible combinations of 2 sensing geometries with 20° azimuth angle separation (one with 25° and one with 45° incidence angle) with respect to 2 sensing geometries with same doppler cone (25° and 45° incidence angle)
Right	Dashed Black	All the possible combinations of 2 opposite sensing geometries (one with 25° and one with 45° incidence angle) with respect to 2 opposite sensing geometries with the same characteristics

Tab. 12 – Input geometries of the Montecarlo simulation of Fig. 64

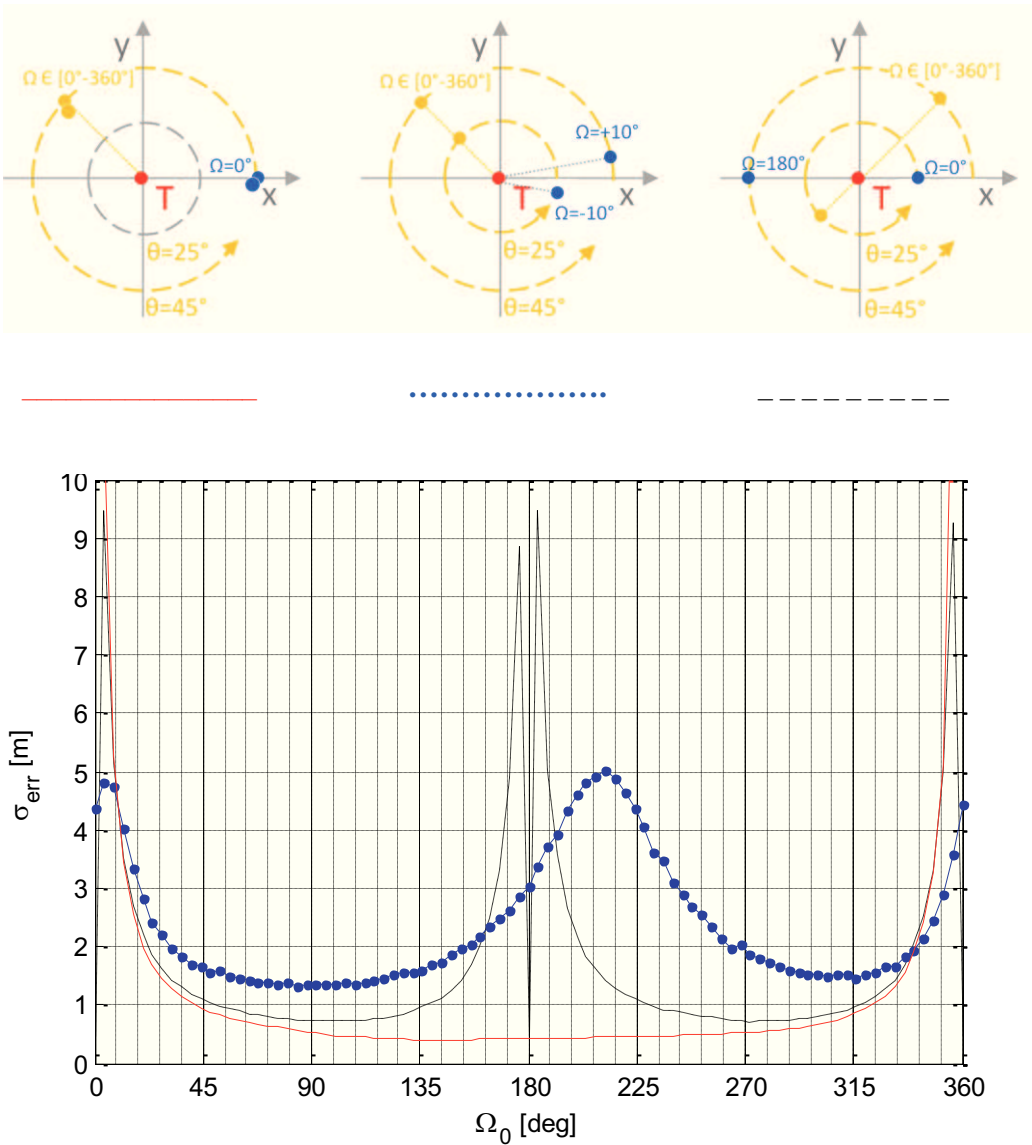


Fig. 64 – Schemas of 3 possible viewing geometries (4 observation points) and the respective standard deviation of the location error

The results obtained in the above simulations confirm the validity of those previously showed at par. 3.2.5, with the following further evidences:

- the optimal conditions are obtained working with images acquired with coincident zero-doppler planes; this is especially evident considering the red and the black dashed cases of Fig. 61, Fig. 62 and Fig. 63. In these charts, it is possible to notice that the worst cases are experienced when there are 2 zero-doppler planes slightly different, while the best performances are obtained for coincident zero-doppler planes. Results less good but more robust can be achieved when the zero-doppler planes are perpendicular one to each other;
- in any case the presence of two sensing geometries with slightly different zero-doppler planes determines a worsening effect. This condition of slightly different zero-doppler planes can be experimented using one image acquired in Left Ascending and one in Right Descending or using one in Right Ascending and one in Left Descending (ref. Fig. 22); this effect decreases at higher latitudes as the separation between the zero-doppler planes increases;
- in case of coincident doppler planes, the considerations drawn at par. 3.2.5 are confirmed;
- Fig. 64 shows that, in case of perpendicular zero-doppler plane (condition possible for high latitudes), the best results are obtained working with images acquired with the largest incidence angle separation;
- making a cross-comparison of all the best performances, it is possible to state that an increase of the number of input images, when all the aforementioned effects are properly taken into account, causes an important improvement of the final location accuracy;
- the very slight asymmetry that can be noticed in some graphs is due to the fact that, for speeding the simulation and having a well conditioned system, the target was not placed at the origin of the reference frame, but moved a little aside (asymmetric condition);
- in case of an existing dataset of images, due to the not easy understanding of the influence of the various imaging geometry parameters (viewing angles, viewing aspects, etc.) on the final results, a Montecarlo simulation based on the real available viewing geometries is a determinant decision support tool for selecting the best combination of inputs.

3.3.1.5 Creating “circular feature-based pGCP”

The name «pseudo Ground Control Point» (pGCP) synthesizes the innovative idea to generate space triangulation points in correspondence of either real or virtual points/features. Therefore the word «pseudo» highlights the fact that these points can be generated by means of multi-aspect feature based space intersection techniques, being a wider set with respect to the ones that can be generated with other state-of-art triangulation methods. Hence, pGCPs could be:

- «real» points, related to direct or dihedral scattering;
- «virtual» points, due to triple (or multiple) scattering;
- «geometric virtual» points, introduced by the aforementioned feature based space intersection methods (e.g. the centre of the base circle of a circular geometry).

GCP and pGCP are useful and therefore interesting to be studied because (from the most obvious to the most challenging and powerful possibility):

- they allow the improvement of the final geolocation/geocoding accuracy of a SAR image;
- they allow the calibration of images and derived products (e.g. for Digital Elevation Model in order to estimate absolute heights);
- they represent the basic feature to be exploited to generate geospatial vector data and therefore to extract full 3D features and produce complete 3D models.

Finally, pGCPs are very interesting because, on the contrary of GCPs created by means of GPS survey, they do not require any inspection or campaign, that would be impossible in certain areas around the globe, and furthermore they represent a viable chance to fully exploit and create added value products from the large amount of data acquired and archived by the COSMO-SkyMed system.

For a practical implementation, creating pGCPs through the approach proposed in paragraph 3.2.4 means reducing the number of the possible viewing geometries, and therefore images, that can be exploited. Ideally it would be necessary to search for points that can be seen from every directions: but while for electro-optical images a cross-road sign on the asphalt can be seen for every roll and pitch angles of the sensor, on the contrary, for a radar image this is not possible, as the signal is backscattered in

presence of trihedral/dihedral angles that cannot be seen from opposite geometries, as for the case of a corner reflector (see Fig. 65).



Fig. 65 – A corner reflector inside the Solfatara crater near Naples (courtesy of ESA)

For the above mentioned reasons, it would be appropriate to exploit the multi-aspect feature based space intersection method, applying it to circular objects, in order to generate “feature based pGCPs”. Therefore a pGCP could be the central point “C” of a circular object, estimated by means of Eq. 33 applied at the backscattering points “B”. In this case the feature based pGCP is a very simple object that can be identified in a set of images acquired with different orbit directions and look angles.

From a practical point of view, a cylindrical “utility pole”, a “streetlamp” or a “cross of walls”, as illustrated in Fig. 66, can be considered optimal features to create a pseudo pGCP, because:

- they are characterized by a strong dihedral backscattering (corresponding to the “B” point of Fig. 48), even in medium resolution images (i.e. COSMO-SkyMed Stripmap images);
- they can be modelled in the easiest way, referring to the space intersection model of Eq. 33;
- the unknown to be estimated are the geospatial coordinates of the centre and the diameter; depending on the requested final accuracy of the pGCP, the diameter can be neglected or considered a known parameter (ideally, the best features are those characterized by the smallest diameter).

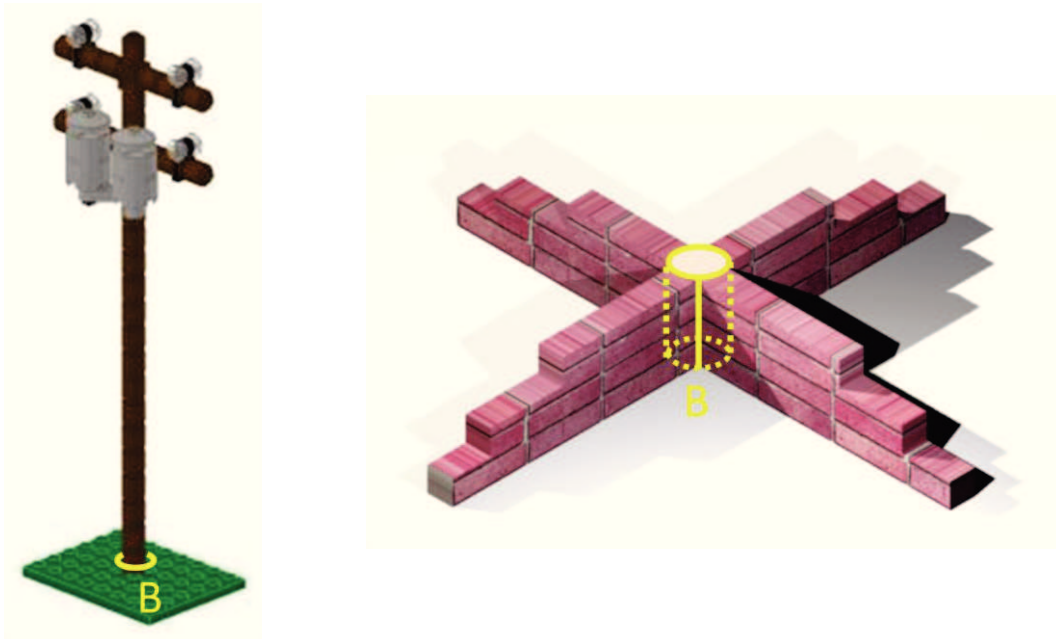


Fig. 66 – An utility pole and a cross of walls could represent a perfect feature to extract a pGCP adopting the circular model. The yellow circle/cylinder represent the adaptation of the circular model to the real case

The proposed method to create pGCP shows the following advantages with respect to the other techniques illustrated in paragraph 3.1:

- all the interferometric techniques strongly rely on the availability of data, not always guaranteed by current operational SAR satellites, such as COSMO-SkyMed or TerraSAR-X, which are programmed to accommodate needs coming from different users. This is especially true for PS-InSAR techniques, the most interesting ones, because it requires at least 40 images acquired in interferometric conditions to correctly estimate the atmospheric mask and thus the position of the point; the same considerations are valid for tomographic applications, that have also complex algorithms and need huge computational resources;
- the national COSMO-SkyMed system, differently with respect to ERS, has a large and heterogeneous database of images acquired all over the world with diversified acquisition geometries. In fact, as shown in paragraph 2.3.1, the system has an high resolution mode (Spotlight) and a medium resolution mode (Stripmap), both suitable for 3D features extraction, that can work:
 - with a look angle in the interval $20^{\circ} \div 55^{\circ}$;
 - in ascending and descending orbits;

- in left and right side viewing geometry.

Fig. 21 and Fig. 22 show these degrees of freedom. Therefore it is highly recommended to adopt techniques allowing the generation of pGCPs from these diversified and heterogeneous datasets;

- in average conditions, the final user finds in the catalogue 3 or more images acquired with heterogeneous geometries and, using them, wants to understand or have a confirmation if a feature/point in one image can geospatially match with a similar/corresponding feature in another image.

3.3.1.6 A practical implementation scheme for circular features extraction

Fig. 67 describes a practical implementation scheme to extract circular features exploiting an heterogeneous dataset of images.

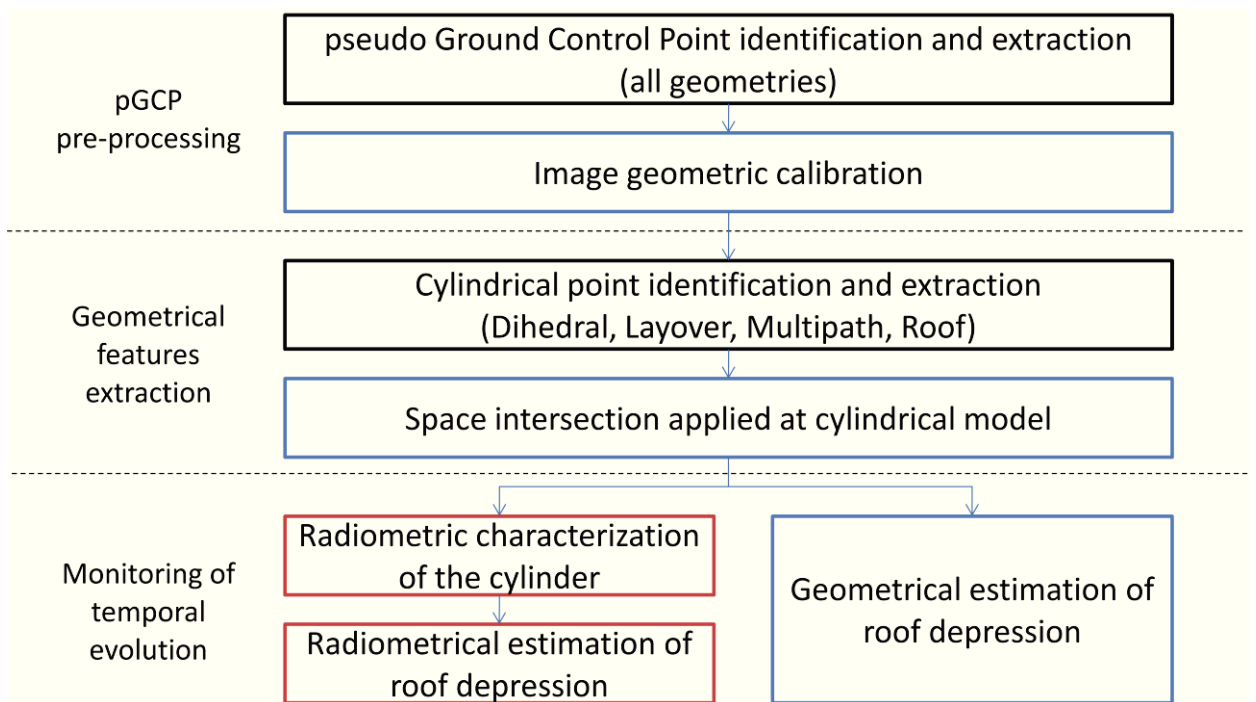


Fig. 67 – A practical implementation scheme for multi-aspect space intersection of cylindrical shape

In the following a detailed description of each step is provided.

1. First of all, an automatic or supervised algorithm performs the identification and extraction of the features that can be recognized as a pGCP:
 - a. it derives the “rough” geospatial coordinates of the centre of the circular object (e.g. pole) from Google Earth (or other open sources);

- b. for each image, a direct geocoding routine translates the “rough” geospatial coordinates into rough pixel coordinates;
 - c. for each images, a routine searches the “fine” subpixel coordinates corresponding to the peak of the “double bounce” scatterer (side of the cylinder) within a search window centred with respect to the rough pixel coordinates, using an FFT interpolation method to achieve subpixel accuracy (1/20 of pixel dimensions);
 - d. the space intersection routine, having in input the “fine” pixel coordinates of the side wall point scatterer (B points) for each image, solves Eq. 33 and gives in output the fine geospatial coordinates of the centre of the cylinder. This coordinates characterizes the pGCP.
2. Geometric calibration of the dataset w.r.t. the pGCP. The pGCP plays a double role: it is used as a matching point among images (usually called “tie point” or “homologous point”) and it can also be used as a GCP to perform the triangulation and to improve the geolocation accuracy of the whole dataset: it means exploiting the final location accuracy of the pGCP, which is better than the geolocation accuracy of the single image. To obtain this goal, a routine modifies the georeferencing parameters of each image (i.e. the range first time and the azimuth first time) in order to obtain zero residuals for the Eq. 33 system applied to the pGCP. The aforementioned procedure is the same of imposing that the range and the azimuth times of each B point corresponds to that deduced from pGCP times:
 - a. the azimuth time of the B point is the same of the pGCP;
 - b. the range time of the B point is linked to that one of the pGCP through Eq. 29.
3. Cylindrical point identification and extraction (Dihedral, Layover, Multipath, Roof). The identification of the coordinates of the scattering points (B, L, V, T) could be:
 - a. manual, through a visual inspection of the images:
 - a post-processing routine determines the fine coordinates of the point scatterer through FFT interpolation of a subset of pixels centred on the rough coordinates;
 - this modality is really useful to take care of all the possible scattering mechanisms, so it is recommended for study purposes;

- b. automatic, having a previous rough knowledge of the building, that allows a rough parameter estimation of the geometrical model (e.g. through visual inspection of an open source image, such as Google Earth). In this case:
 - the geometrical model and the image metadata allow to estimate the rough coordinates of the point scatterers, used as the centre of a search window inside which the point scatterer is searched (and the fine pixel coordinates are estimated);
 - this modality allows an automation of the process.
4. Multi-aspect space intersection for circular model:
 - a. if the side wall scattering point is always detectable, the cylinder parameters (geospatial coordinates of the centre & diameter) are estimated by means of Eq. 33;
 - b. in case there is the opportunity or the need to exploit either L or V points, the space intersection model is described by Eq. 34.

The schema of Fig. 67, being thought for a cylindrical tank with floating roof, foresees specific post-processing and target analysis steps, both described in literature, (49) and (50), taking advantage of the full three dimensional reconstruction of the target:

1. geometrical estimation of roof depression. The roof height can be determined, for each image, using the estimated value of the diameter and the following relation (derived by Eq. 29 and Eq. 32):

$$t = \frac{d \sin \theta - (R_T - R_B)}{\cos \theta} \quad \text{Eq. 41}$$

2. radiometric estimation of roof depression, eventually exploiting an initial estimate of the depression made with the previous method to initialize the radiometric model, whose surface properties (dielectric constant and roughness) are unknown.

A complete end-to-end validation of the proposed schema and a performance analysis is provided in paragraph 4.2.

3.3.2 MULTI-ASPECT FEATURE BASED SPACE INTERSECTION FOR LINEAR FEATURES: THE “HYPERBOLOID SPACE INTERSECTION”

The multi-aspect space intersection theory is suitable to extract many class of features. While in the previous paragraph an application to circular features was introduced, in the following I will introduce a new space intersection model suitable to generate linear features.

In literature, there are other methods conceived to extract linear features based on the matching of:

- homologous points belonging to corresponding linear features for images acquired with the same look side and orbit direction, but with different look angles, (4);
- homologous linear features belonging to images acquired with different viewing geometries, (5).

The weakness of the first approach consists in the fact that, for high resolution images, it is not easy to match corresponding points among images because of the presence of speckle and for the high sensitivity to small changes. As it is difficult to match homologous points, so it is hard to match linear features.

The second method does not foresee any modification of the space intersection problems and is only focused on the local building reconstruction.

3.3.2.1 A geometric model for modelling linear geometries

The approach I propose is based on the assumption that it is always possible to identify at least 2 points per linear feature per image. The matching technique does not impose any constraint on these points nor it is necessary to impose their correspondence, as the matching is only considered at feature level (Fig. 68).

If this condition is satisfied, it would be possible to describe the linear feature as the intersection of two hyperboloids of revolution (or circular hyperboloid), each of them obtained revolving the linear generatrix around the “local” rectilinear trajectory of the satellite. The orbit of the satellite, when observing the two aforementioned points, can be represented with a “local” rectilinear trajectory (therefore the linear feature and the orbit are skew lines), as shown in Fig. 69.

Fig. 70 represents the intersection model, Fig. 71 shows a sketch of the circular hyperboloids obtained revolving the linear feature around the local rectilinear satellite trajectories.

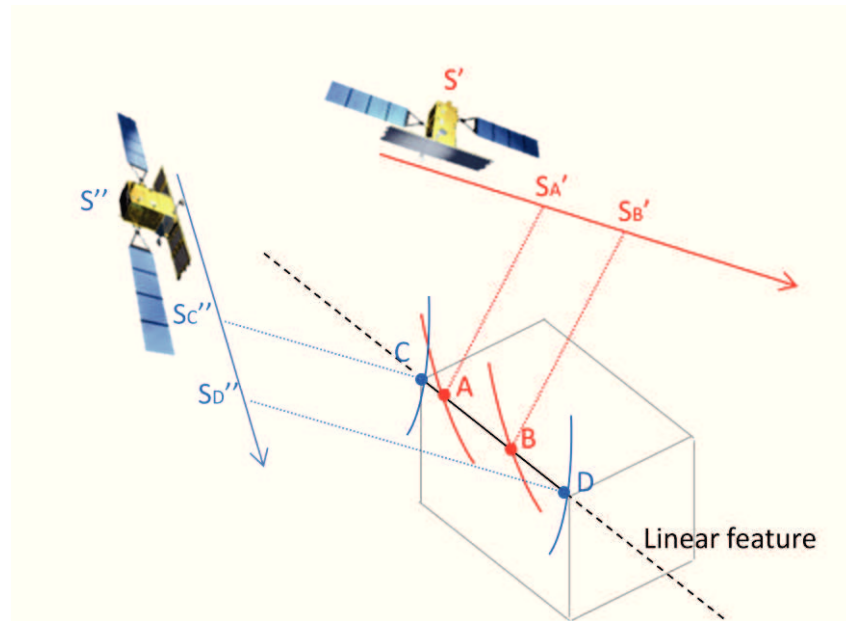


Fig. 68 – Extraction of a linear feature: in each acquisition (i.e. image) it is possible to identify at least 2 different points, without any requirement of matching among them

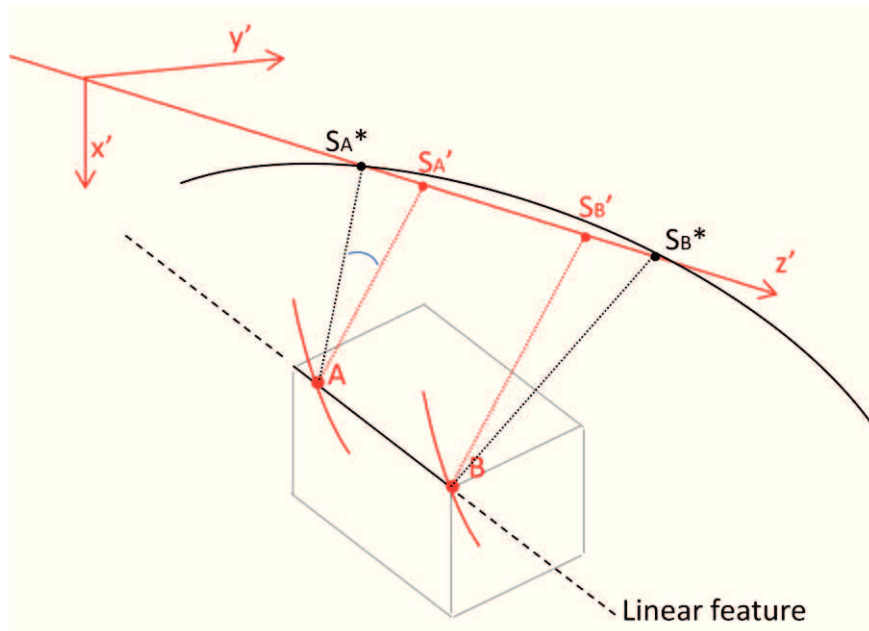


Fig. 69 – “Local” rectilinear trajectory of the satellite

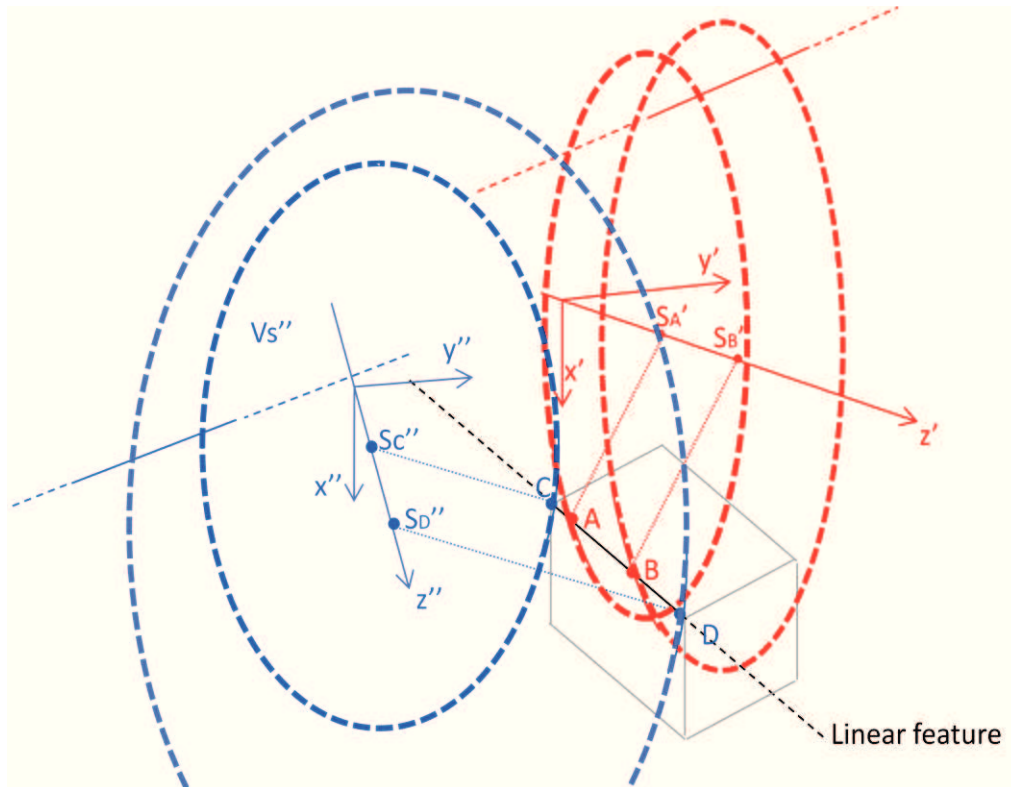


Fig. 70 – A model representing a linear feature seen as the intersection of 2 circular hyperboloids

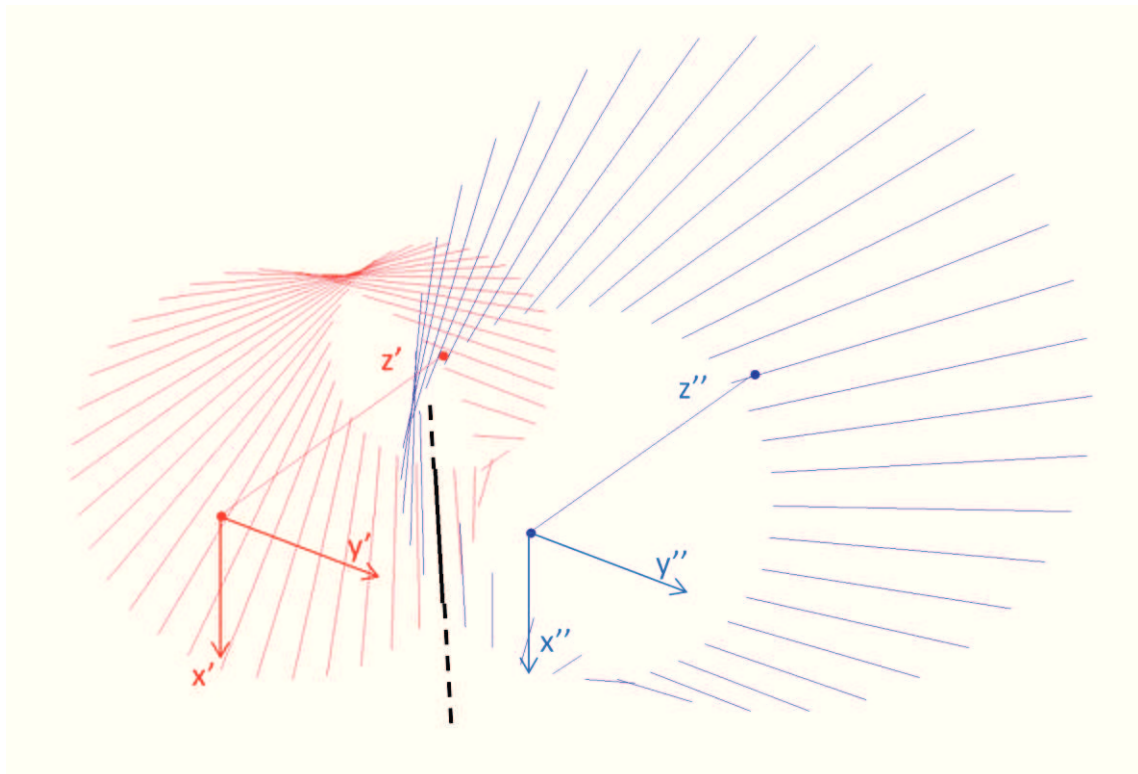


Fig. 71 – The circular hyperboloids are obtained revolving the “black” linear feature, the generatrix, with a circular directrix around the local rectilinear satellite trajectories

The hyperboloid is a quadratic surface that can be described by the general equation:

$$A^{**}x^2 + B^{**}y^2 + C^{**}z^2 + D^{**}xy + E^{**}xz + F^{**}yz + G^{**}x + H^{**}y + I^{**}z + J^{**} = 0 \quad \text{Eq. 42}$$

with A^{**} , B^{**} , C^{**} , D^{**} , E^{**} , F^{**} , G^{**} , H^{**} , I^{**} and J^{**} being fixed real constants and x , y , z being variables.

To simplify the form of Eq. 42, let me introduce a Hyperboloid Oriented (HO) reference frame with the z axis along the “local” rectilinear trajectory (the vector that conjuncts the two satellite positions at the instants of observation), the y axis perpendicular to the orbital plane (the plane comprising the position and the velocity vector of the satellite) and the x axis to have a right-handed orientation.

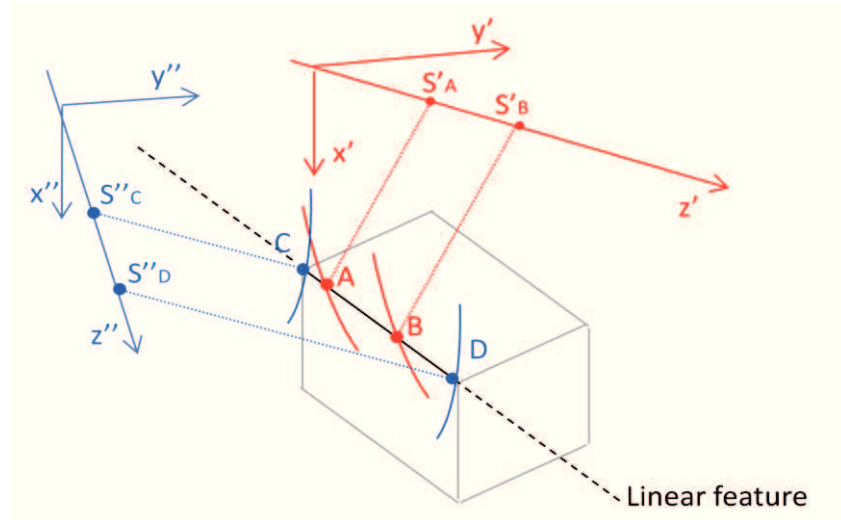


Fig. 72 – The Hyperboloid Oriented (HO) reference frames

Introducing the HO Reference Frame, which is equivalent to define the geometry of the axes of symmetry of the hyperboloid, Eq. 42 becomes:

$$A^*x^2 + B^*y^2 + C^*z^2 + D^*z + E^* = 0 \quad \text{Eq. 43}$$

Taking into account that the directrix is a circle (therefore the hyperboloid is circular), $A^* = B^*$; furthermore, dividing every terms by $-E^*$, it is possible to further simplify Eq. 43:

$$A(x^2 + y^2) + Bz^2 + Cz = 1 \quad \text{Eq. 44}$$

In order to obtain the coefficients of Eq. 44, it is possible to exploit the following conditions:

- the belonging of the points A and B of Fig. 73 to the surface of the hyperboloid;
- the linearity of the generatrix, equivalent to impose the passage of the hyperboloid surface through a third point (point 0 of Fig. 73), belonging to the generatrix.

Imposing the passage of the hyperboloid to points 0, A and B, the following conditions can be exploited:

$$\begin{cases} \text{point 0} \rightarrow A' (x_0'^2 + y_0'^2) + B' z_0'^2 + C' z_0' = 1 \rightarrow A' R_0'^2 + B' z_0'^2 + C' z_0' = 1 \\ \text{point A} \rightarrow A' (x_A'^2 + y_A'^2) + B' z_A'^2 + C' z_A' = 1 \rightarrow A' R_A'^2 + B' z_A'^2 + C' z_A' = 1 \\ \text{point B} \rightarrow A' (x_B'^2 + y_B'^2) + B' z_B'^2 + C' z_B' = 1 \rightarrow A' R_B'^2 + B' z_B'^2 + C' z_B' = 1 \end{cases} \quad \text{Eq. 45}$$

where R'_0 , R'_A and R'_B are the slant range measurements and z'_0 , z'_1 and z'_2 are the observation points' positions in the HO reference frame.

Therefore, to exploit the conditions of Eq. 45, the satellite positions and the slant range measurements have to be transformed into the HO reference frame. Fig. 73 shows this transformation. The satellite positions are determined as the intersection of the z axis and the plane perpendicular to the z axis passing through the observed points A and B. As the ECEF positions of A and B are unknown, they can be determined, in first approximation, as the intersection of the reference ellipsoid with the range-doppler equations of S_A^* and S_B^* (see paragraph 2.2.2.3). Point 0 can be freely chosen as a point of the projected segment AB, even if it could be useful to choose it exactly in the middle between the other 2 points. The position of the satellite during the acquisition of point 0 is determined following the above described procedure.

The slant range measurements R'_0 , R'_A and R'_B are determined as the distance between the aforementioned satellite acquisition positions, in the HO reference frame, and the projections of A, B and 0 points on the ellipsoid.

To further refine these results, after the completion of the intersection procedure, the above calculations can be repeated exploiting the heights of A, B and 0 points obtained from the estimated linear feature.

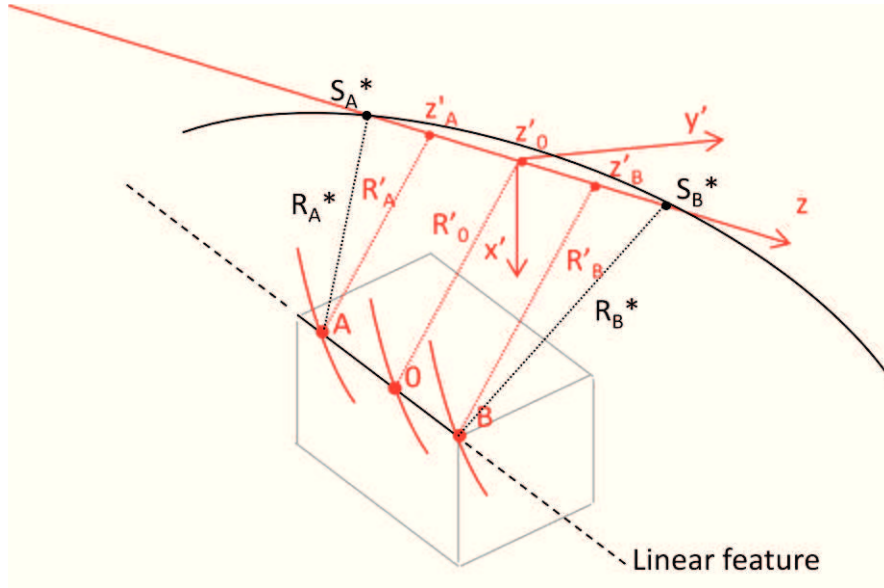


Fig. 73 – The conversion from the ECEF reference frame to the HO reference frame

If the origin of the HO reference frame is moved in the 0 point, the following expressions of the real constant A', B' and C' are obtained:

$$\left\{ \begin{array}{l} A' = \frac{1}{R_0'^2} \\ B' = \frac{1}{z'_A(z'_A - z'_B)} \left(1 - \frac{R_A'^2}{R_0'^2} \right) + \frac{1}{z'_B(z'_B - z'_A)} \left(1 - \frac{R_B'^2}{R_0'^2} \right) \\ C' = \frac{z_B}{z'_A(z'_B - z'_A)} \left(1 - \frac{R_A'^2}{R_0'^2} \right) + \frac{z_A}{z'_B(z'_A - z'_B)} \left(1 - \frac{R_B'^2}{R_0'^2} \right) \end{array} \right. \quad \text{Eq. 46}$$

The Eq. 46 is valid for every position of the origin 0. If it is exactly in the middle between z'_A and z'_B , the expression can be simplified considering $z'_B = -z'_A$.

3.3.2.2 The Hyperboloid Space Intersection

Exploiting the geometric model introduced in the previous paragraph, it is possible to define a linear feature as the intersection of 2 hyperboloids, each defined in its own HO reference frame. Therefore, a coordinate transformation from ECEF to HO reference frame is necessary. The generic point belonging to the modelled line can be parameterized exploiting a third relation, that could be the expression of a plane perpendicular to the z axis of one of the two HO reference frames.

The generic point belonging to the intersection line can be written as:

$$\begin{cases} A'(x'^2 + y'^2) + B'z'^2 + C'z' = 1 \\ A''(x''^2 + y''^2) + B''z''^2 + C''z'' = 1 \\ z' = z'_p \end{cases} \quad \text{Eq. 47}$$

with:

$$\begin{aligned} \begin{bmatrix} x' \\ y' \\ z' \end{bmatrix} &= Mrot' \begin{bmatrix} x - x'_0 \\ y - y'_0 \\ z - z'_0 \end{bmatrix} \\ \begin{bmatrix} x'' \\ y'' \\ z'' \end{bmatrix} &= Mrot'' \begin{bmatrix} x - x''_0 \\ y - y''_0 \\ z - z''_0 \end{bmatrix} \\ z'_p &\in [z'_{pin}; z'_{pfin}] \end{aligned} \quad \text{Eq. 48}$$

where:

- x, y, z are the ECEF coordinates of a point belonging to the linear feature;
- $x', y', z', x'', y'', z''$ are the coordinates of the aforementioned point in the HO reference frame of the first and second hyperboloids (corresponding to the first and second images);
- $Mrot', Mrot''$ are the rotation matrix of the two HO reference frames;
- $[x'_0, y'_0, z'_0]$ and $[x''_0, y''_0, z''_0]$ are the origin of the two reference frames;
- $A', B', C', A'', B'', C''$ are the hyperboloids coefficients of Eq. 46;
- z'_p describes a plane perpendicular to the z' axis in the HO reference frame. Its values are comprised in the interval $[z'_{pin}, z'_{pfin}]$, where z'_{pin} and z'_{pfin} can be established considering the points closer to the extreme of the line.

The equations in Eq. 47 are used to derive the normal equation:

$$\begin{cases} F_1 = A'(x'^2 + y'^2) + B'z'^2 + C'z' - 1 = v_1 \\ F_2 = A''(x''^2 + y''^2) + B''z''^2 + C''z'' - 1 = v_2 \\ F_3 = z' - z'_p = v_3 \end{cases} \quad \text{Eq. 49}$$

so that the sum of the squares can be minimized, Eq. 50:

$$\sum_{i=1}^3 v_i^2 \rightarrow \min \quad \text{Eq. 50}$$

where F_1, \dots, F_3 are the observation equations and v_1, \dots, v_3 are the residuals of each observation equation. A qualitative validation of this approach is provided in par. 4.3.

3.3.2.3 Error budget

The error budget presented in this paragraph is analogous to that one of paragraph 3.3.1.4. It has been introduced for the same reasons and exploits similar simulation modalities. In this case the reference frame is fixed with respect to the satellites. The orbit of the satellite is locally approximated with a line (easing the application of the hyperboloid intersection, which requires the rectilinear trajectory conversion).

To conduct a sensitivity analysis, we have two different domains to explore:

- the possible relative position of one satellite with respect to the other;
- the possible relative position of the linear feature with respect to the satellites.

For these reasons, the two satellites will have fixed orbits with respect to the reference frame, while the linear feature moves around the z axis to explore the different possible geometries. The simulation geometry of Fig. 74 is defined by means of:

- the incidence angle θ (that in case of flat earth coincide with the look angle of the figure);
- the azimuth angle Ω of the satellites with respect to the reference frame
- the azimuth angle Ω_{line} of the linear feature with respect to the reference frame.

The results of the error sensitivity analysis are displayed as a function of these angles, assuming as constant the height of the satellites. Different position of the linear feature with respect to the satellites will be taken into account in order to understand the geometry influence on the estimation accuracy of the line location and to understand the relations with the others, already presented, space intersection techniques.

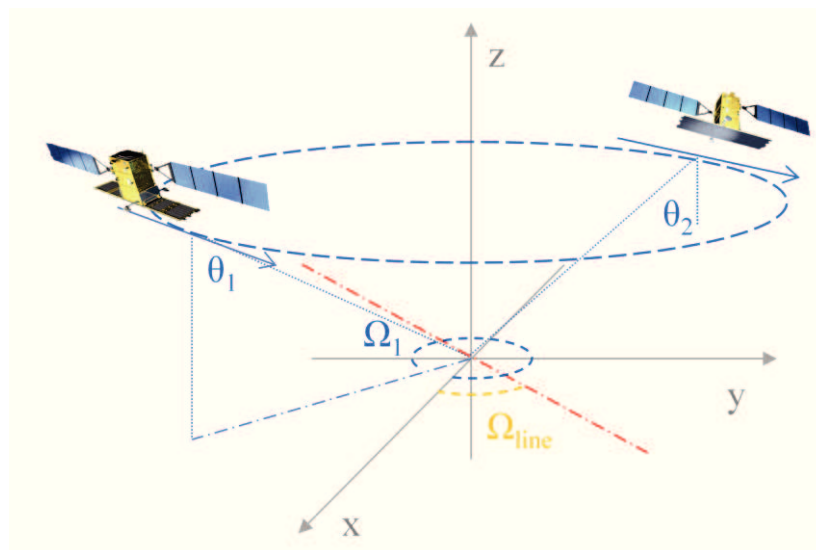


Fig. 74 – The reference frame for the Monte Carlo simulation aiming at assessing the accuracy of the Hyperboloid Space Intersection model

Schema	Graph	Description
Left	Solid Red	All the possible horizontal variations of a line with respect to 2 sensing geometries with the same doppler plane and look side and respectively with 25° and 55° of incidence angle
Left-central	Dotted Blue	All the possible horizontal variations of a line with respect to 2 sensing geometries with the same doppler plane and opposite look side, both with 55° of incidence angle
Right-central	Dashed Black	All the possible horizontal variations of a linear element with respect to 2 sensing geometries with different doppler plane (20° of difference) and same look side, both with 55° incidence angle
Right	Dotted-dashed magenta	All the possible horizontal variations of a linear element with respect to 2 sensing geometries with different doppler plane (20° of difference) and same look side, one with 25° and one with 55° of incidence angle

Tab. 13 – Input geometries of the Montecarlo simulation of Fig. 75

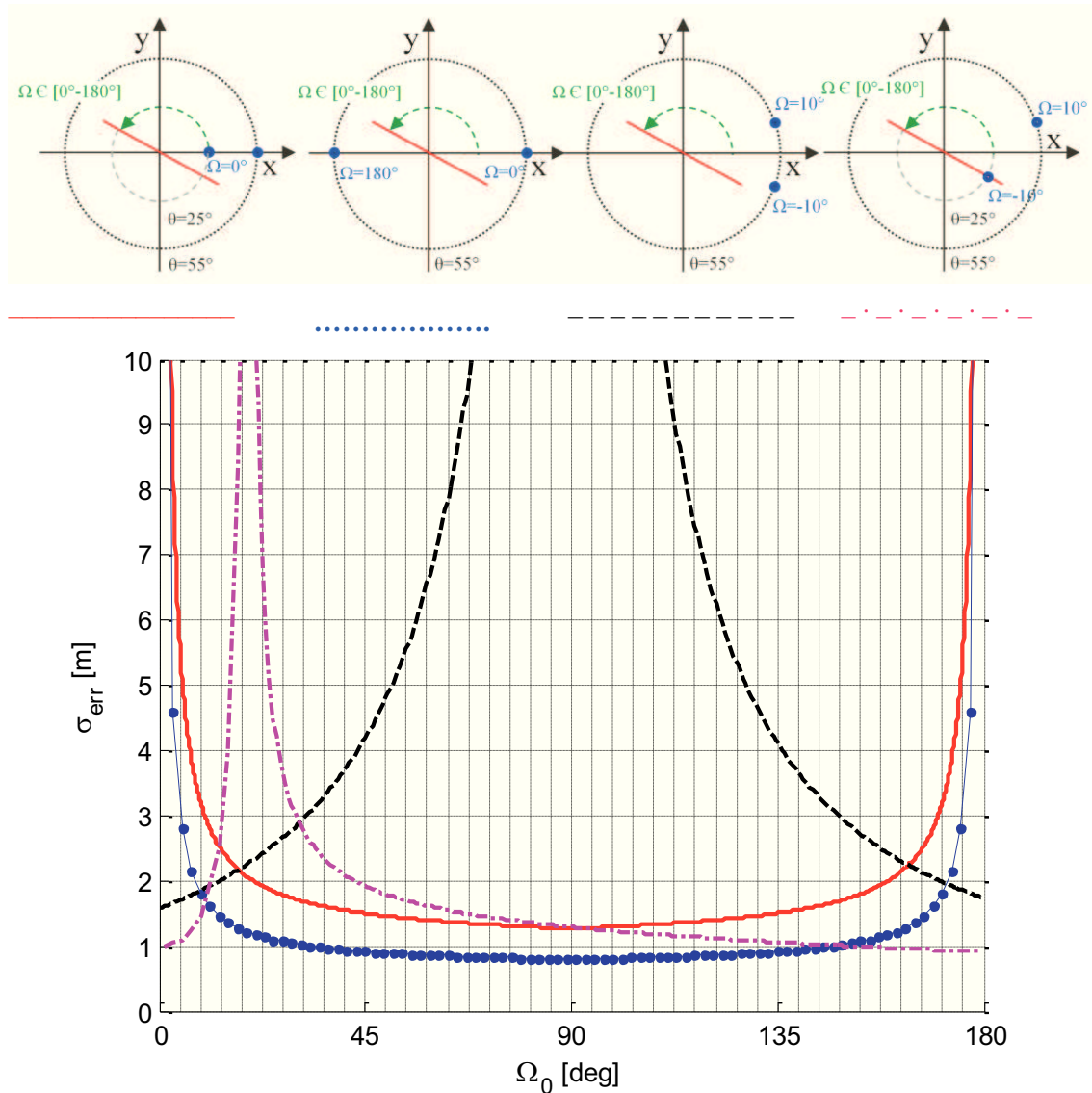


Fig. 75 – Schemas of 4 possible viewing geometries (2 observation points) and the respective standard deviation of the location error

The results obtained in the simulations of Fig. 75 are in accordance with those previously analyzed, with the following further evidences:

- the optimal results are obtained working with images acquired with coincident zero-doppler planes when the line is parallel to the flight path; this is especially evident considering the blue dotted and the red cases;
- it is possible to notice that the worst cases are experienced when the linear feature is parallel to the relative position of the second satellite with respect to the first one (magenta dashed-dotted case confirms this evidence);
- with the availability of at least 4 images (e.g. 1 RA at 25°, 1 RA at 55°, 1 LD at 25° and 1 LD at 55°) it is possible to detect and reconstruct all the possible line directions at the best performances;
- in case of more than 2 input images, having the necessity to select the best combination of inputs, depending on the orientation of the lines of interest, a Montecarlo simulation, based on the real available viewing geometries, can support the selection of the best combination of input images;
- the best performances of the “Hyperboloid Space Intersection” are comparable with those of the other methods, based on the range-doppler model.

3.3.2.4 A practical implementation scheme for linear features extraction

Fig. 76 describes a practical implementation scheme to extract linear features exploiting the hyperboloid space intersection method:

1. identification and extraction of the features that can be recognized as a pGCP: same description of paragraph 3.3.1.6;
2. geometric calibration of the dataset w.r.t. the pGCP: same description of paragraph 3.3.1.6;
3. linear features detection and extraction (dihedral, edge between two non homogeneous regions, shadows). The detection can be fully automated through the implementation of a point scatterers detector or canny filter, (51).
4. supervised line matching implies the availability of an imagery analyst who matches the corresponding features.
5. Hyperboloid space intersection, by means of the model of paragraph 3.3.2.2.

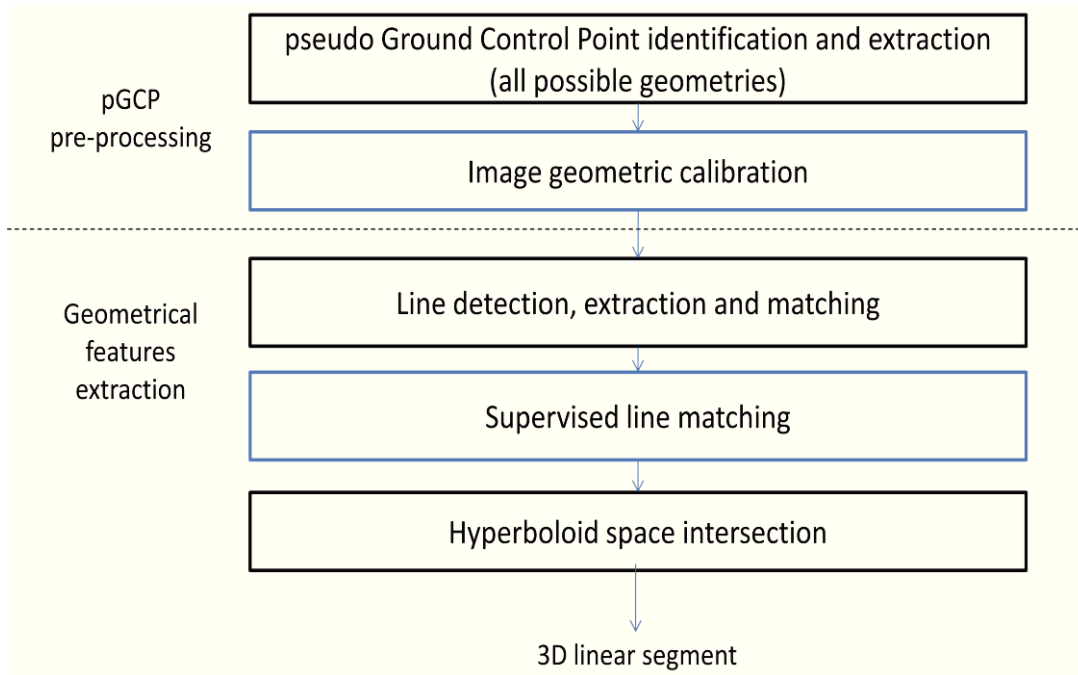


Fig. 76 – A practical supervised implementation scheme for hyperboloids space intersection

The procedure described above can be automated by means of an autonomous matching between the features, as synthesised in Fig. 77.

In this case the differences with respect to the previous approach are:

- the necessity to exploit at least 3 images;
- an unsupervised line matching step makes an initial attempt to match the first image with respect to the second and third one, based on the following rules:
 - similarity of line extension and azimuth with respect to the north;
 - relations with the closer lines;
- the comparison of the 2 resulting 3D linear segments, evaluated in terms of distance between them. Obviously, if the distance exceeds a pre-defined threshold, the matching is not accepted and the matching step has to be re-evaluated. Possible approaches to correct the matching could be to change the correspondence from one line to the closest in one direction, considering the good matching as a reference condition.

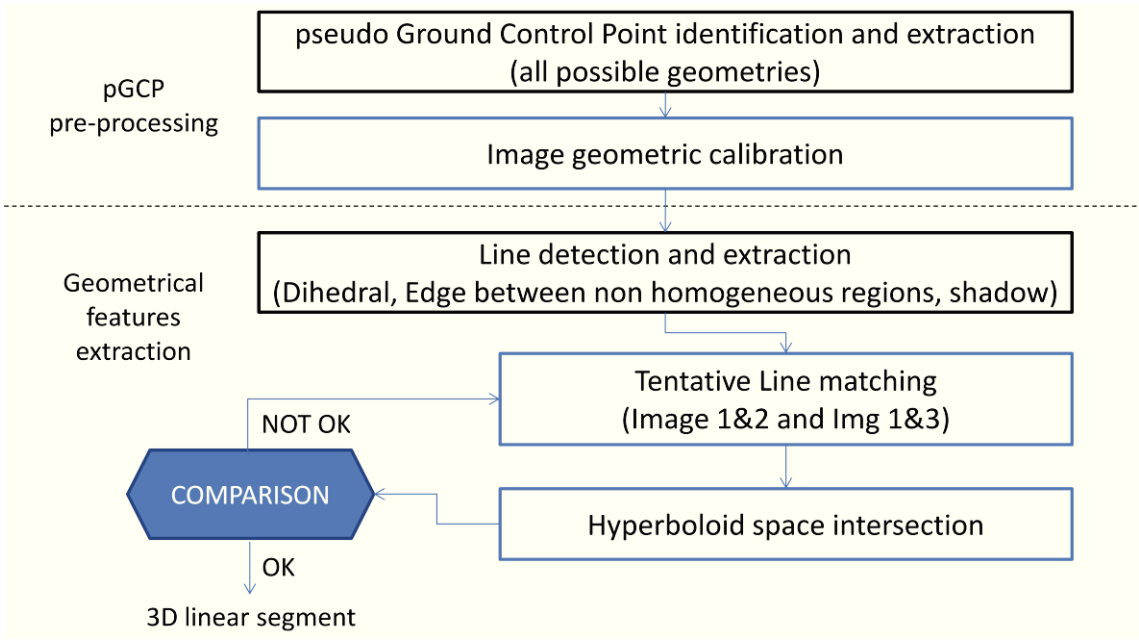


Fig. 77 – A practical unsupervised implementation scheme for hyperboloids space intersection

A complete end-to-end validation of the proposed schema and a performance analysis is provided in paragraph 4.4.

3.4 AUTOMATION OF THE 3D FEATURES EXTRACTION BASED ON MULTI-ASPECT FEATURE BASED SPACE INTERSECTION

3.4.1 A SCENARIO ANALYSIS OF THE STATE OF ART TECHNIQUES FOR AUTOMATIC 3D FEATURE EXTRACTION

The automation of 3D feature extraction, exploiting the proposed approaches, is a complex problem. To solve this kind of problem in case of building features extraction, Xu and Jin defined an interesting and comprehensive proposal, (5), exploiting:

- an edge detector of Constant False Alarm Rate (CFAR);
- a Hough transform technique for parallel line segment pairs in order to extract the parallelogram-like image of the building walls in SAR images;
- an automatic reconstruction algorithm to match object images taken from different aspects and to reconstruct the building objects. Besides, an iterative method is proposed for the coregistration of multi-aspect building images;
- a hybrid priority criterion to evaluate the reliability of the reconstruction result.

Another interesting approach is based on the joint use of high-resolution optical and SAR data for building extraction and 3D reconstruction in large urban areas, (46).

Another interesting goal to fulfill with an autonomous and automatic approach could be trying to exploit the high SAR temporal revisit time to monitor evolving phenomena, such as a the construction of infrastructures or other facilities.

3.4.2 AN IMPLEMENTATION SCHEME FOR AUTOMATIC 3D FEATURES EXTRACTION

Fig. 78 provides a end-to-end implementation scheme for the automation of the 3D features extraction phase:

- Area of Interest extraction: geospatial enabled extraction of the Area of Interest (AoI) or Region of Interest (RoI) through a direct geocoding procedure;
- Despeckling: the edge-detection strongly relies on the capability of the speckle filtering techniques to preserve shape and dihedral backscattering. For this reason, Lee or Frost filtering, (52) and (53), are not adequate. Advanced filtering techniques, such as BM3D (54) and Probabilistic Patch Based (PPB) (55) approaches are needed in order to preserve shape and linear features;
- Edge-detector: the linear features detector can be:

- a CFAR edge detector, (5),
- a Canny filter, (51), especially suitable for the transition between a target and its shadow;
- for bright dihedral returns, an approach based on scale-space ridge detection at a single scale, using a Bayesian classification step to select the ridge points corresponding to bright lines, can be used, (56);

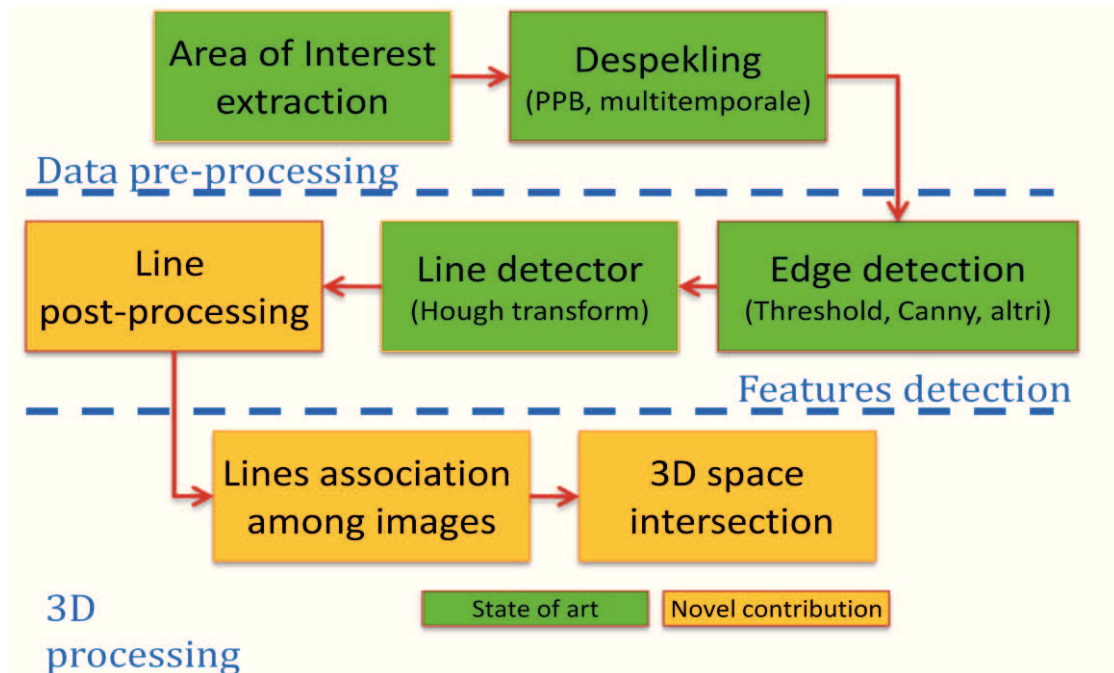


Fig. 78 – A practical scheme for the automatic 3D features extraction

- Line-detector: after having implemented the detection step, linear segments can be extracted by means of an Hough transform, as proposed in (5);
- Line post-processing: the line post processing must simplify the inputs before executing the association of the lines among images. In the proposed approach, the post processing executes a merge of collinear and close segments;
- Line association among images: the lines association is based on a similarity measure of segments. This measure takes into account:
 - the length of the segments;
 - the orientation of the segments;
 - the absolute location of the segments, in first approximation based on a DEM or a local height defined by the user.

When a segment is higher with respect to the local ground reference, the distance operator acts as pre-screening and reinstitutes a subset of the nearer segment to be considered for the matching.

- 3D space intersection: line space intersection is based on the “Hyperboloid space intersection” method proposed in paragraph 3.3.2. The interaction between this step and the previous one, devoted to line association, is the same of the “unsupervised approach” introduced in paragraph 3.3.2.4.

This approach was tested on the “Matera test case”: the relevant experimental results are reported in paragraph 4.5.

CHAPTER 4 - CASE STUDIES AND EXPERIMENTAL RESULTS

4.1 “VENICE” CASE STUDY

4.1.1 AIM OF THE CASE STUDY

The aim of this case study is to:

- experimentally validate the model proposed in paragraph 3.3.1;
- exploit the proposed methodology to understand the scattering mechanism.

4.1.2 TEST SITE AND DATASET

The test site regards the Industrial area of Porto Marghera, close to Venice (the red box of Fig. 79).



Fig. 79 – The test area of Porto Marghera, in the Venice lagoon (Google Earth© image)



Fig. 80 – The target building chosen for the experimental studies (Bing Maps© images)

CHAPTER 4 - Case studies and Experimental Results

For the “Venice” case study, 24 COSMO-SkyMed images, acquired in the nominal Stripmap mode (COSMO-SkyMed Stripmap Himage), were used. All these images exhibit HH polarization.

Their incidence angles are, in average, quite low; the sensing geometries are:

- 16 images in Right looking - Descending orbit (RA);
- 8 images in Right looking - Ascending orbit (RA).

N°	Satellite	Sensor mode	Beam	Pol	Geometry	Date of acquisition
1	COSMO-1	Stripmap	HI_03	HH	RA	2010/09/03 04:55:40
2	COSMO-2	Stripmap	HI_03	HH	RA	2010/09/27 04:55:23
3	COSMO-1	Stripmap	HI_01	HH	RD	2010/09/27 17:28:39
4	COSMO-1	Stripmap	HI_01	HH	RD	2010/10/05 04:55:20
5	COSMO-2	Stripmap	HI_01	HH	RD	2010/10/05 17:28:32
6	COSMO-	Stripmap	HI_01	HH	RD	2010/10/13 17:28:28
7	COSMO-	Stripmap	HI_01	HH	RD	2010/10/21 17:28:21
8	COSMO-	Stripmap	HI_01	HH	RD	2010/09/11 17:28:47
9	COSMO-	Stripmap	HI_01	HH	RD	2010/11/30 17:27:55
10	COSMO-	Stripmap	HI_03	HH	RA	2010/11/06 04:54:57
11	COSMO-	Stripmap	HI_03	HH	RA	2010/11/22 04:54:45
12	COSMO-	Stripmap	HI_05	HH	RD	2010/10/02 17:22:33
13	COSMO-	Stripmap	HI_01	HH	RD	2010/11/22 17:27:59
14	COSMO-	Stripmap	HI_03	HH	RA	2010/09/11 04:55:35
15	COSMO-	Stripmap	HI_03	HH	RA	2010/10/29 04:55:02
16	COSMO-	Stripmap	HI_03	HH	RA	2010/11/14 04:54:50
17	COSMO-	Stripmap	HI_01	HH	RD	2010/09/27 17:28:39
18	COSMO-	Stripmap	HI_05	HH	RD	2010/10/02 17:22:33
19	COSMO-	Stripmap	HI_01	HH	RD	2010/10/05 17:28:32
20	COSMO-	Stripmap	HI_01	HH	RD	2010/10/13 17:28:28
21	COSMO-	Stripmap	HI_01	HH	RD	2010/10/21 17:28:21
22	COSMO-	Stripmap	HI_01	HH	RD	2010/09/11 17:28:47
23	COSMO-	Stripmap	HI_01	HH	RD	2010/11/30 17:27:55
24	COSMO-	Stripmap	HI_01	HH	RD	2010/11/22 17:27:59

Tab. 14 – Dataset of CSK images for the “Venice” test case

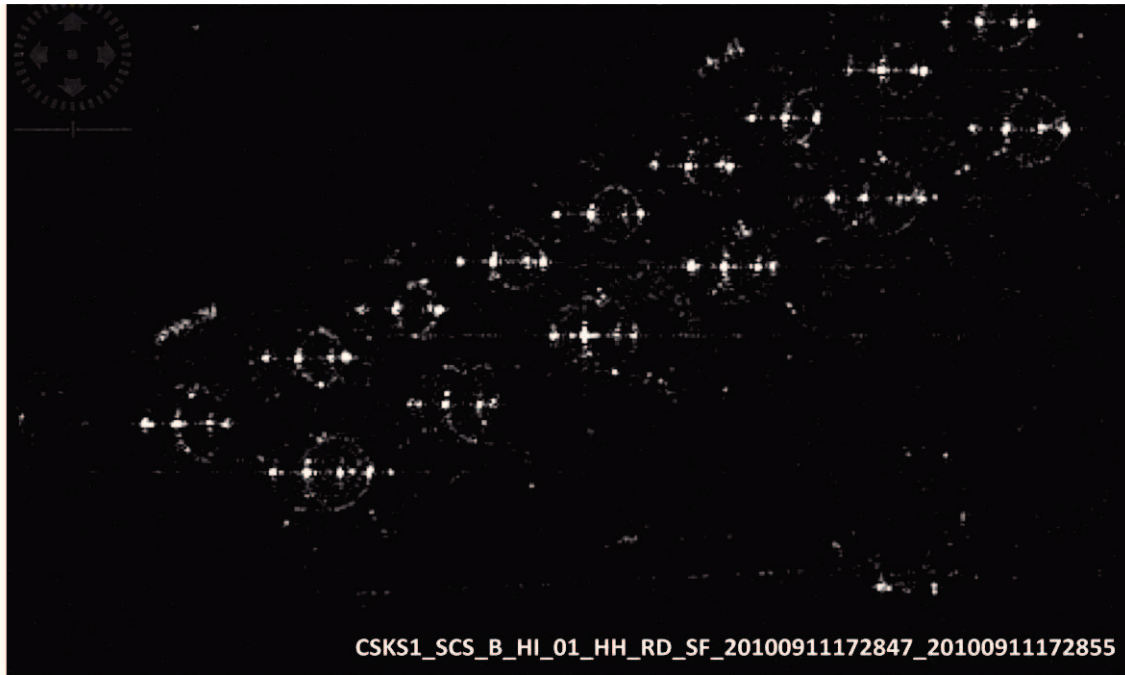


Fig. 81 – A CSK® Stripmap image of the test area

4.1.2.1 Ground truth

In this test site, the following ground truths are available:

- geoid height (sea level), from the national geodetic information system;
- cylinder height (measured with other remote sensing sources) with an accuracy of less than 0.4 m;
- high resolution pictures of the cylinder (Bing Maps©).

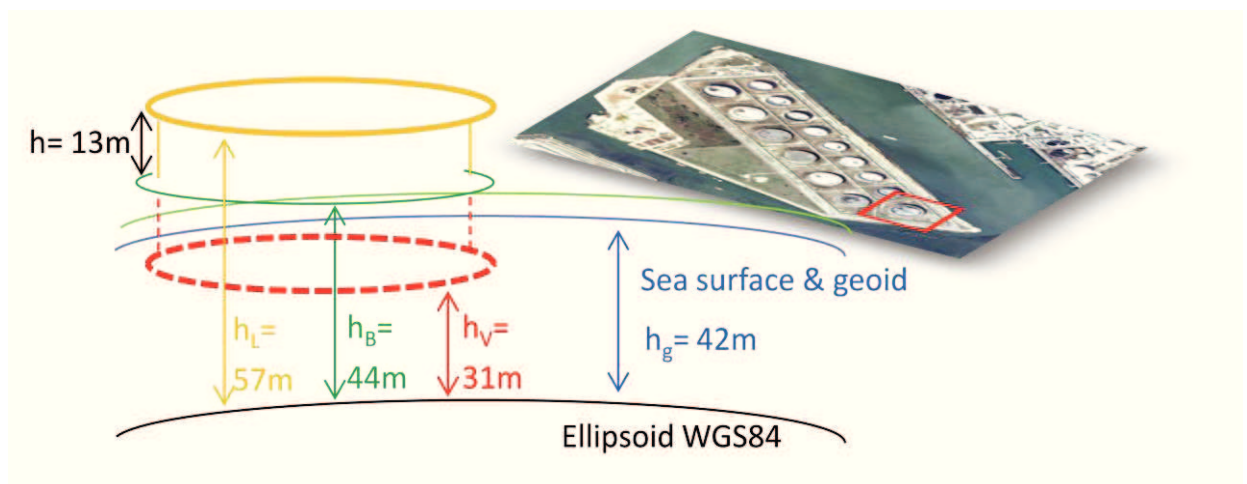


Fig. 82 – Ground truth of the “Venice” test case

4.1.3 PHENOMENOLOGY: CONFIRMATION OF THE PROPOSED MODEL WITH MEDIUM GEOMETRIC RESOLUTION IMAGES

In paragraph 3.3.1.1 (page 72) a geometrical model to describe the possible scattering mechanisms of a cylindrical tank has been introduced. As already mentioned, the aim of

this test case is to verify the adherence of the model to the real scattering mechanism and to show the applicability of space intersection techniques as a support to the imagery analysts for the understanding of the scattering mechanisms in case of complex scenarios.

Fig. 83 represents the association of the backscattering points with the features of the model. The complexity of the problem is worsened by SAR image resolution: in fact, the images, being acquired with 3 meters geometric resolution, do not give a complete understanding of the cylindrical geometry, while only the main backscattering points can be detected.

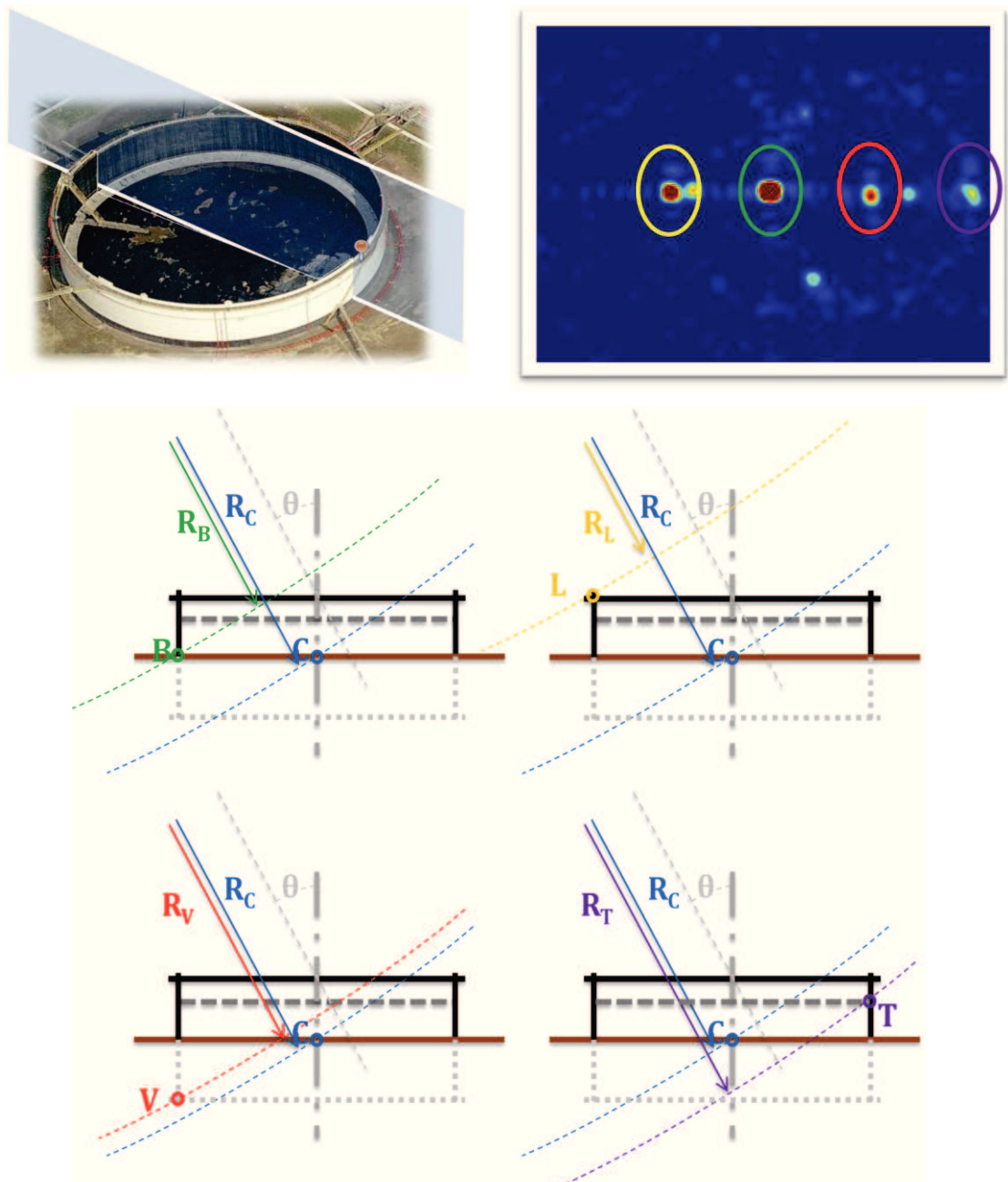






Fig. 83 – From the top left: an image of the target cylindrical tank (Bing maps©), the identification of the relevant backscattering point in the SAR image, the model that describe the cylindrical geometry

In order to validate the associations, and thus the model, the n-images stereo model is employed for each one of the 4 scattering points, exploiting 4 images acquired from the same look side and with different incidence angles, in order to:

- evaluate the residuals of the model, for having a confirmation that the scattering effects associated among images are due to the same features;
- estimate the geospatial coordinates and verify:
 - the correspondence of the latitude and longitude of the L, B and V points (all referring to features which are on a vertical line, therefore they have the same latitude and longitude);
 - the height of the 3 aforementioned points with respect to the ground truths.

The achieved results confirm the correctness of the association and of the validity of model. In fact, the residuals are in the order of magnitude of less than half pixel dimensions, while the satisfaction of the other conditions is reported in Tab. 15, from which it is possible to notice that:

- the latitudes and longitudes of the L, B and V points differ, one with respect to the other, of less than the geometric resolution (see Fig. 84 for a geospatial plot of the results);
- the height measurements have a good accordance with ground truths; even in this case the measurement accuracy is less than the geometric resolution (see measures of Fig. 82).

Sym.	Feature	Latitude [°]	Longitude [°]	Ellipsoidal height [m]
	<u>L point</u> upper single bounce scattering point	45.448854°N	12.271553°E	57.56m
	<u>B point</u> external double bounce scattering point	45.448855°N	12.271530°E	44.77m
	<u>V point</u> virtual triple bounce scattering point	45.448863°N	12.271525°E	31.52m
	<u>T point</u> internal double bounce scattering point	N.A.	N.A.	N.A.

Tab. 15 – The results of the space intersection performed with images acquired with the same viewing geometry



Fig. 84 – The geospatial position of B (green), L (orange) and V (red) points (Google Earth© image and sw)

On the other hand, it is not possible to determine the position of the T point exploiting the space intersection method. Considering that the cover of the tank is a floating roof, it is possible to understand from the negative results that the roof itself moved during the time span of the acquisitions. Images of Fig. 85, acquired on the target cylinder with the same geometrical parameters, show the movement of the T point. This movement can obviously be linked to the movement of the floating roof in the period between two subsequent acquisitions.

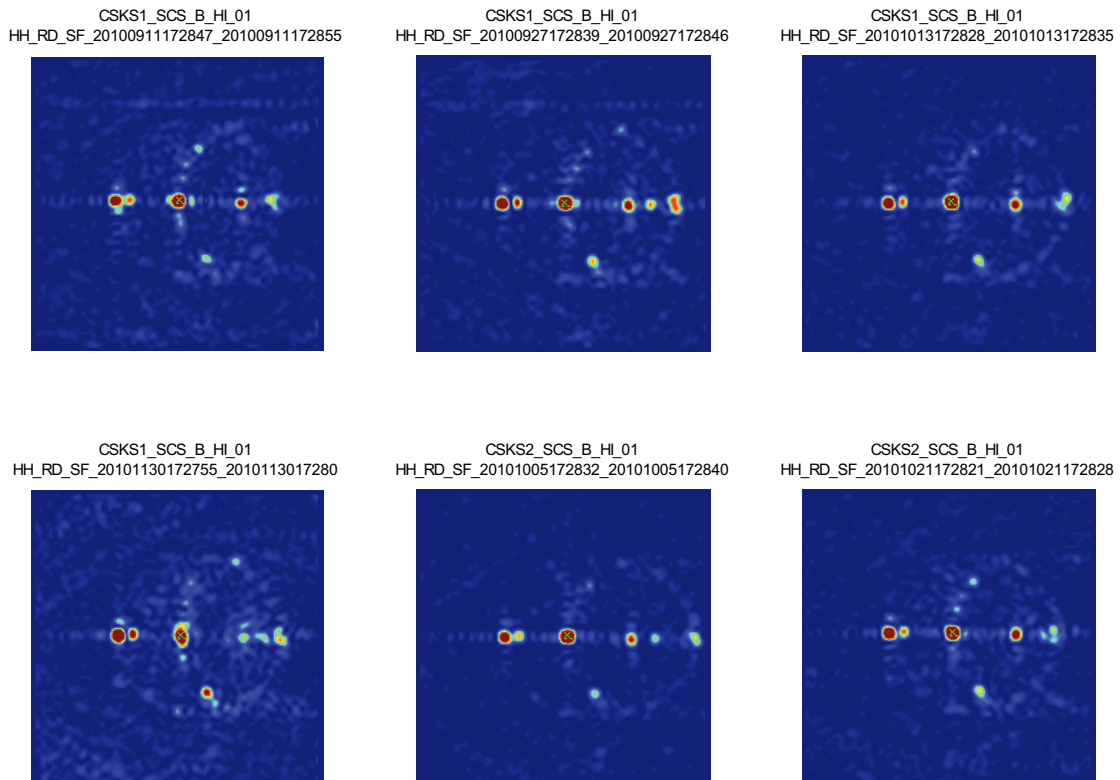


Fig. 85 – A set of images acquired on the cylinder with the same geometrical parameters, show the movement of the T point due to the movement of the floating roof

4.1.4 PHENOMENOLOGY: CONFIRMATION OF THE PROPOSED MODEL WITH HIGH GEOMETRIC RESOLUTION IMAGES

Exploiting high resolution images it is possible to better understand the scattering mechanisms and validate the proposed model (see Fig. 86 and Fig. 87):

1. direct scattering of the elements on the top of the external surface;
2. double bounce of the electromagnetic wave caused by the subsequent reflections from the ground and the external surface. The backscattering is concentrated in correspondence of the bottom of the external surface because all the double bounce paths have the same length of the single scattering at the bottom of the external surface;
3. triple bounce of the electromagnetic wave caused by the subsequent reflections from the ground, from the elements on the top of the external surface and again from the ground. The backscattering is concentrated in correspondence of a virtual point, symmetric with respect to the ground of the elements on the top of the external surface (the triple bounce paths have the same length of the single scattering at the bottom of the virtual external surface);

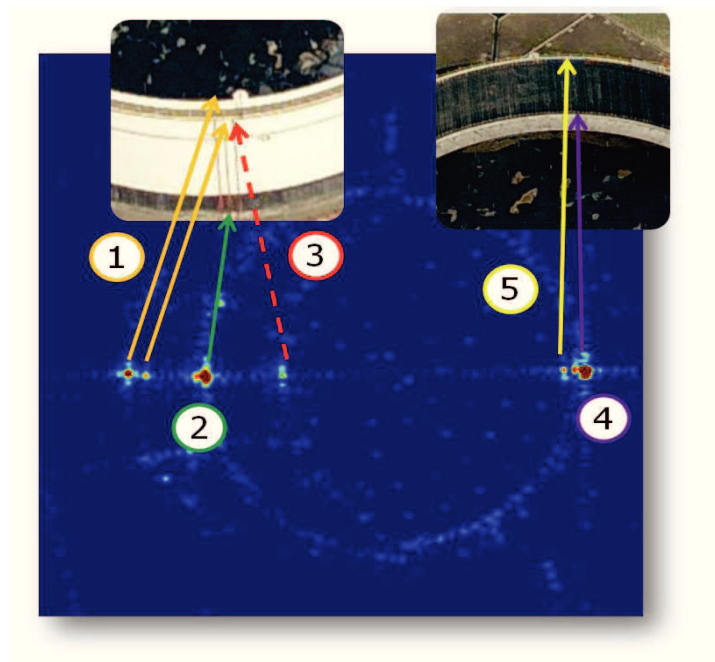


Fig. 86 – High resolution image of the target cylinder, that highlight the scattering phenomenology

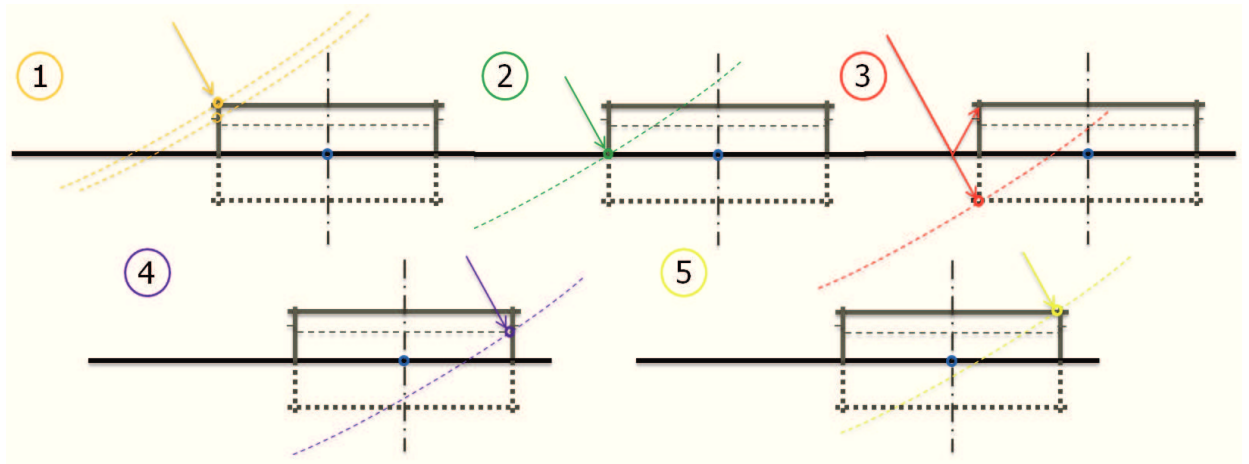


Fig. 87 – Cylinder scattering phenomenology

4. double bounce of the electromagnetic wave caused by the subsequent reflections from the roof and the internal surface;
5. direct scattering of the elements on the top of the internal surface.

4.1.5 THE LOCAL TERRAIN INFLUENCE ON TRIPLE BOUNCE LOCATION

The analysis of the subset of images of the “Venice” test case of Fig. 88 shows a displacement of the V points with respect to the doppler plane of the other pGCPs (B, L, T). This displacement would probably be caused by the local inclination of the ground, which creates a dihedral angle with the vertical wall of the cylindrical tank, as depicted in Fig. 89.

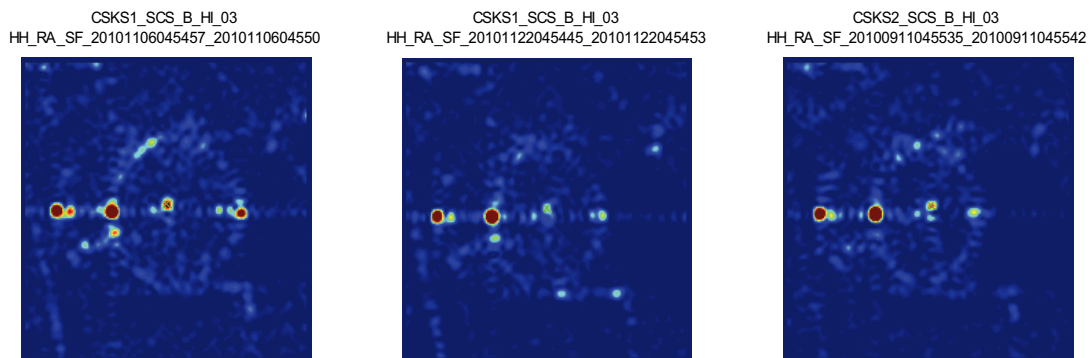


Fig. 88 – A set of CSK images that shows a displacement of the V point w.r.t. the doppler plane of the other pGCPs.

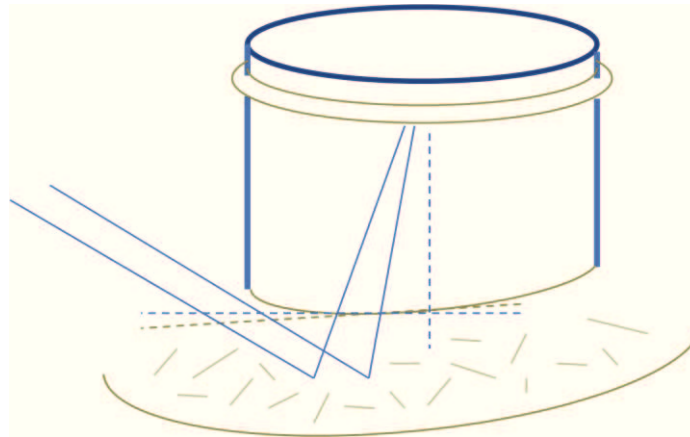


Fig. 89 – A possible explanation of the displacement of the V points with respect to the doppler plane of the other pGCPs

4.1.6 DISCUSSION & POSSIBLE IMPROVEMENTS

The results of “Venice” test case show that:

- the phenomenology is in perfect accordance with the proposed geometric model;
- a complex backscattering phenomenology, characterized by triple bounce reflections, is present in case of flat ground around the cylinder and in case of presence of circular structures around the external surface;
- the space intersection technique is useful to understand the peculiarity of the scattering mechanism, highlighting the presence of the triple bounce reflection.

4.2 “NAPLES AND SOLFATARA” CASE STUDY

4.2.1 AIM OF THE CASE STUDY

The aim of this case study is to:

- experimentally validate the model proposed in paragraph 3.3.1;
- estimate the accuracy of the technique applied.

4.2.2 TEST SITE AND DATASET

The test site encompass Naples, with a particular focus on the Industrial area (the right box of Fig. 90) and its surroundings, and the Solfatara volcano crater in Pozzuoli (the left box of Fig. 90).

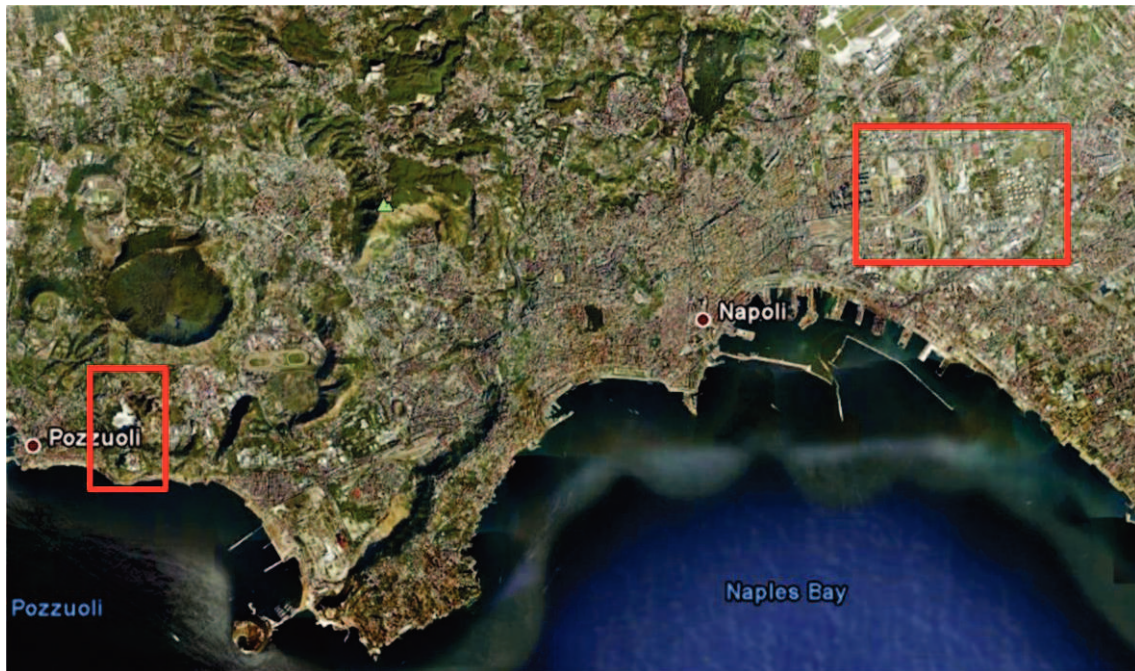


Fig. 90 – The test area of Naples and its surroundings (Google Earth© image)



Fig. 91 – A Google Earth© image of the industrial area of Naples, chosen to be a suitable test site



Fig. 92 – The target building for the experimental studies (Google Earth© image on the left, Bing Maps© image on the right)

For this case study, Tab. 16 shows the 18 COSMO-SkyMed images that were used, 16 acquired in the nominal Stripmap mode (COSMO-SkyMed Stripmap Himage) and 2 acquired in the nominal Spotlight 2 mode (COSMO-SkyMed Spotlight Enhanced).

Within this dataset, 5 images were acquired with VV polarization, 11 images with HH polarization and 2 images with HV one. The incidence angle spans the whole system capability, while the sensing geometries are:

- 2 Left looking – Ascending orbit (LA);
- 3 Left looking - Descending orbit (LD);
- 3 Right looking - Descending orbit (RA);
- 10 Right looking - Ascending orbit (RA).

N°	Satellite	Sensor mode	Beam	Pol	Geometry	Date of acquisition
1	COSMO-1	Stripmap	HI_0B	VV	LA	2008/02/11 04:34:36
2	COSMO-1	Stripmap	HI_05	HH	LA	2008/05/22 04:27:38
3	COSMO-1	Stripmap	HI_06	VV	RD	2010/11/29 17:11:00
4	COSMO-1	Stripmap	HI_16	HH	RA	2010/10/11 05:06:00
5	COSMO-1	Stripmap	HI_16	HH	RA	2010/10/27 05:05:49
6	COSMO-1	Stripmap	HI_16	HH	RA	2010/11/28 05:05:27
7	COSMO-1	Stripmap	HI_23	VV	LD	2008/05/13 18:21:19
8	COSMO-2	Stripmap	HI_0B	HH	RA	2010/11/03 04:47:40
9	COSMO-2	Stripmap	HI_04	HV	LD	2010/07/18 17:48:36
10	COSMO-2	Stripmap	HI_06	VV	RD	2010/11/05 17:11:17
11	COSMO-2	Stripmap	HI_16	HH	RA	2010/10/19 05:05:54
12	COSMO-2	Stripmap	HI_16	HH	RA	2010/11/04 05:05:44
13	COSMO-2	Stripmap	HI_20	HH	RA	2008/03/30 05:22:15
14	COSMO-3	Stripmap	HI_06	VV	RD	2010/10/21 17:11:29
15	COSMO-3	Stripmap	HI_09	HV	LD	2010/09/16 17:53:53
16	COSMO-3	Stripmap	HI_16	HH	RA	2010/10/20 05:05:56
17	COSMO-1	Spotlight	S2_22	HH	RA	2009/01/09 05:13:12
18	COSMO-2	Spotlight	S2_16	HH	RA	2009/05/30 05:05:41

Tab. 16 – Dataset of CSK images for the “Naples” test case

4.2.2.1 Ground truth

As ground truths for this experiment, the following data have been collected:

- the position of a corner reflector inside the Solfatara crater (this place has been exploited by ESA and ASI as a calibration site for SAR sensors because of the flat terrain which allows to reach the Signal Noise Ratio required by SAR quality assessment). The corner reflectors are useful both to conduct Impulse Response Function analysis and to measure the geolocation accuracy of the

system. Fig. 93 shows an image of the crater and of the corner reflectors placed inside;

- the diameter and the position of a cylindrical tank in the industrial area of Naples, as depicted in Fig. 94. The accuracy of the measures is of about 10 cm, an accuracy acceptable for the aims of this study.



Fig. 93 – A corner reflector inside the Solfatara crater exploited as a Ground Control Point

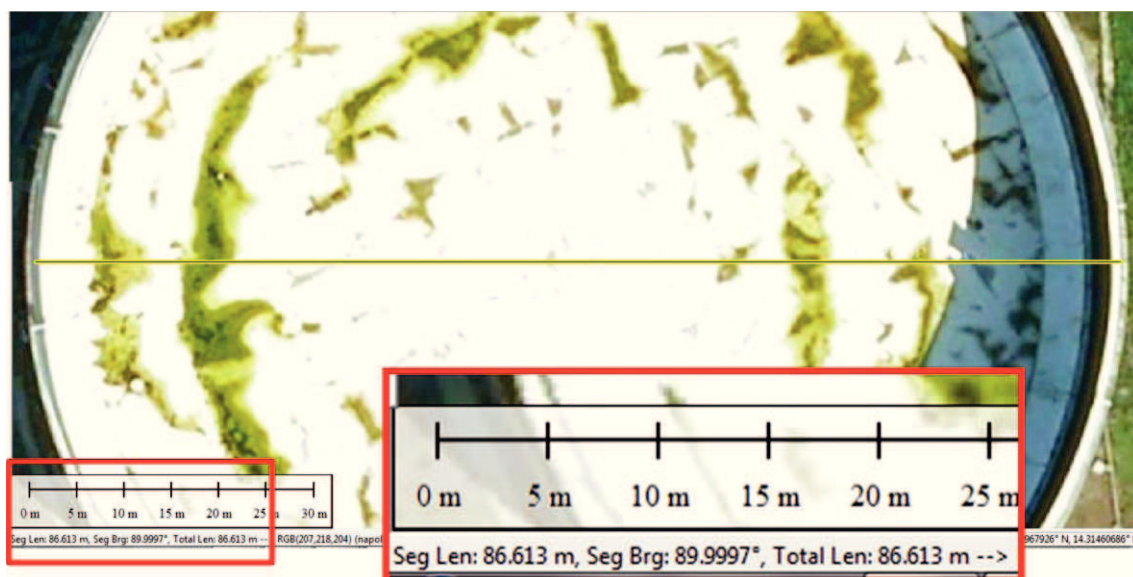


Fig. 94 – The measurement of the diameter of the chosen cylinder (Globalmapper® sw, Google Earth image)

4.2.3 RESULTS OF MULTI-ASPECT SPACE INTERSECTION

With respect to the practical scheme proposed in paragraph 3.3.1.6, the following results were obtained:

4.2.3.1 1st step

The first step requires the identification of at least one pGCP. In this case, first of all a supervised attempt to identify a suitable object is performed exploiting Google Earth (or another open source optical image provider). The utility pole of Fig. 95 is chosen for being easily detectable in an empty parking area.



Fig. 95 – pGCP detection in Google Earth©

The rough coordinates of the utility pole, extracted from Google Earth, are used to locate the target in SAR images (exploiting a inverse georeferencing routine) and to extract the 16 snapshots of Fig. 96. The snapshots are only 16 of 18 images because the backscattering point B is not present in the 2 images taken with a HV polarization. In fact, because of the scattering mechanisms, at the B point in a HV or VH image corresponds no backscattering signal (the experimental results obviously confirm the theory).

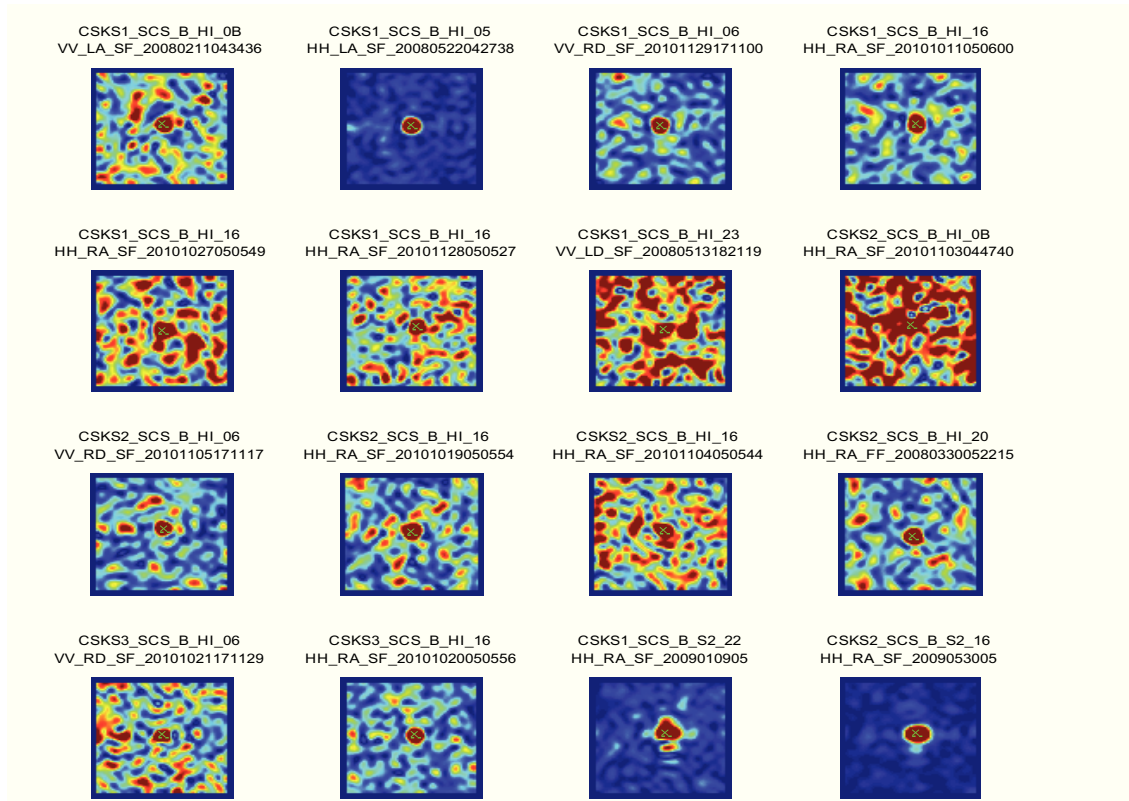


Fig. 96 – pGCP identification in the COSMO-SkyMed® images of the dataset

From Fig. 96 it is possible to notice that only 2 images do not allow to detect a double bounce scattering in correspondence of the base circle of the utility pole (B point). It is not easy to understand the reason of such behaviour: from a match of the acquisition times with an open source weather archive¹ it is possible to say that in both occasions there was some rainfall (classified as light rain); in any case it is not possible to say exactly that this was the cause of the absence of backscattering, considering that in other raining days the double bounce scattering is perfectly visible. Probably a combination of geometrical configuration and soil properties (presence of water, humidity, etc.) or the presence of objects close to the pole have created the aforementioned conditions.

It is interesting to note that the first 14 snapshots are extracted from Stripmap images, with a geometric resolution of 3 meters. This means that the pole was perfectly identified within images with a geometric resolution 10 times greater than the object itself.

Merging all the 14 available information, exploiting the model described by the Eq. 33, the final geospatial position of the pGCP representing the C point was deduced:

utility pole pGCP (point “C”) → 40.859939° N, 14.286643° E, 51.99 m

¹ The historical weather data of Naples airport has been downloaded from the website www.ilmeteo.it

4.2.3.2 2nd step

The second step of the procedure aims at calibrating all the images with respect to the extracted pGCP. That means that all the azimuth and range “first times” of all the images were calibrated in order to allow a perfect matching in correspondence of the pGCP. After the geometric calibration, if the Eq. 33 is applied to the 14 datasets, the residuals of the solution are equal to zero.

In this case, it is interesting to assess the positioning accuracy of the pGCP exploiting a ground truth. The Ground Control Point is the one introduced in paragraph 4.2.2.1.

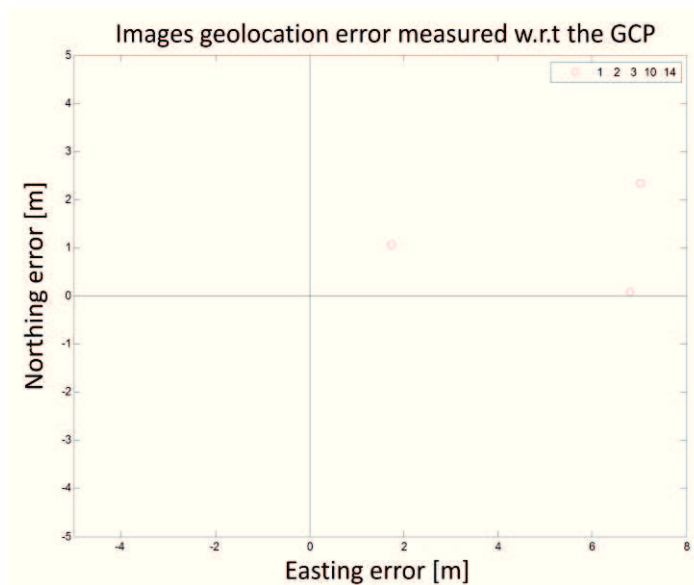


Fig. 97 – The figure shows the images geolocation error measured w.r.t. a known GCP before the geometric calibration

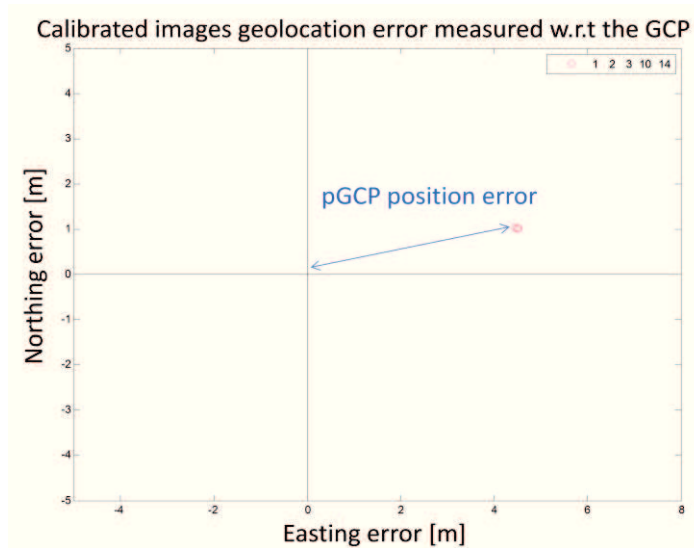


Fig. 98 – The figure shows the images geolocation error measured w.r.t. a known GCP after the geometric calibration.

At the scope of evaluating the pGCP position error, the pGCP was extracted only from images n° 1, 2, 3, 10 and 14 because they were the only ones in which the corner reflector was visible.

The obtained position accuracy is consistent with the error budget, taking into account that the verified system geolocation accuracy is of about 6 meter, (57) and (43).

For the following analysis the is removed.

4.2.3.3 3rd step

The third step requires the identification of the relevant points for the model. In this case, it is enough identifying all the external double bounce points, i.e. B points. Fig. 99 shows the results of the identification for a subset of images: the B point is easily detectable in every image. Among the proposed images, it is possible to note that the 5th one presents some peculiar scattering effects that cause a displacement of the scattering point.

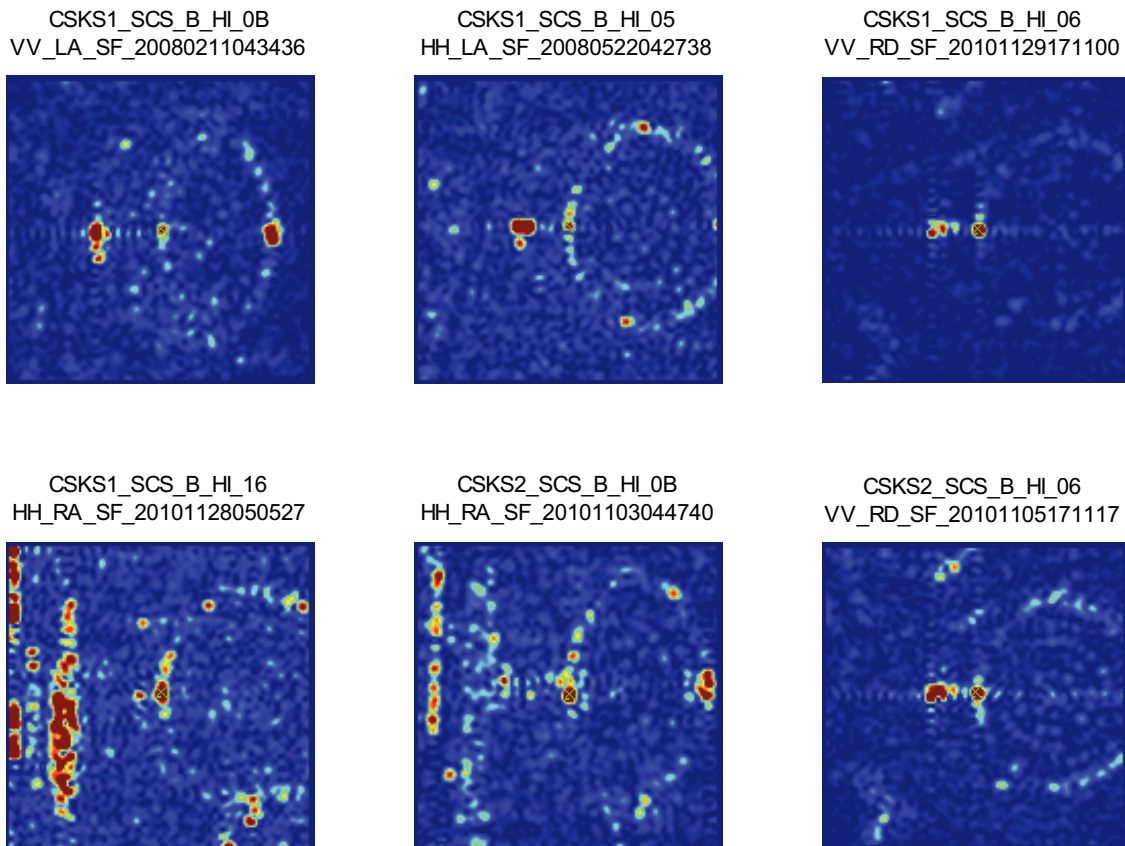


Fig. 99 – Identification of the external double bounce points B for a possible subset of the input image

With respect to Fig. 99, other considerations can be made:

- the exploitation of the “upper single bounce scattering point”, i.e. L point, is not robust: in fact, close to the L point and, in certain images, merged with its scattering, there is the scattering of another circular ring. Being this second feature too close to the upper side of the wall, especially in images with high incidence angle, it cannot be distinguished from the L point. Therefore, the location accuracy of the L points worsens;
- even if there is an external ring, it did not determined a triple bounce scattering point, i.e. V point; this absence is probably due to the presence of grass in front of the cylindrical tank preventing the double bounce.

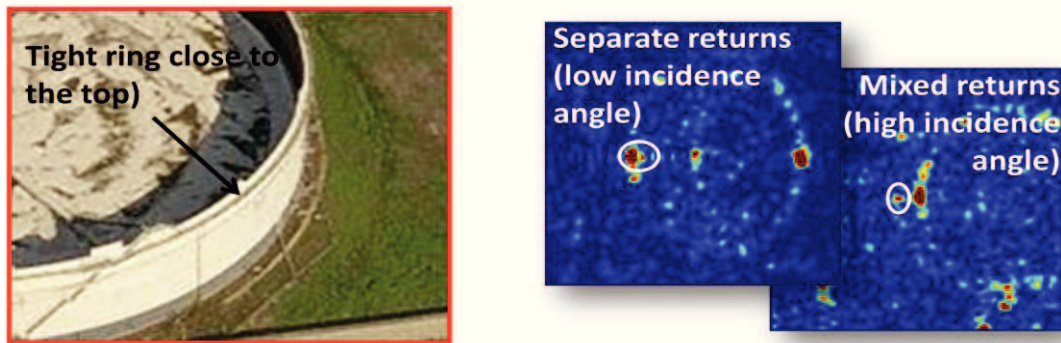


Fig. 100 – The tight ring highlighted in the left image (Bing Maps©) cause a double bounce scattering close to the upper side of the wall

4.2.3.4 4th step

Applying the simplified model of the Eq. 33, it is possible to estimate:

- the diameter of the cylinder, that is one of the unknown of the system. Tab. 17 shows the results obtained for different combinations of input images; the obtained results show a variability that strongly depends on the:
 - accuracy of the identification of the “B point”;
 - geometrical configuration of the input images;
- the position of the centre of the cylinder, shown in Fig. 101. Increasing the number of images and taking into account the good configurations suggested by the Montecarlo simulation, the geolocation accuracy of the cylinder centre, i.e. point “C”, improves.

Input images	Estimated diameter
1 2 3 4 6 8 10	86,68
1 2 3 4 5 6 8 10 11 12 14 17 18	86,32
'1 2 3 4 5 6 8 10 18	86,75
'2 3 4 5 6 8 10 18	86,78
'1 2 3 6 10	86,53
'1 3 18	86,09

Tab. 17 – The estimated diameter of the cylinder

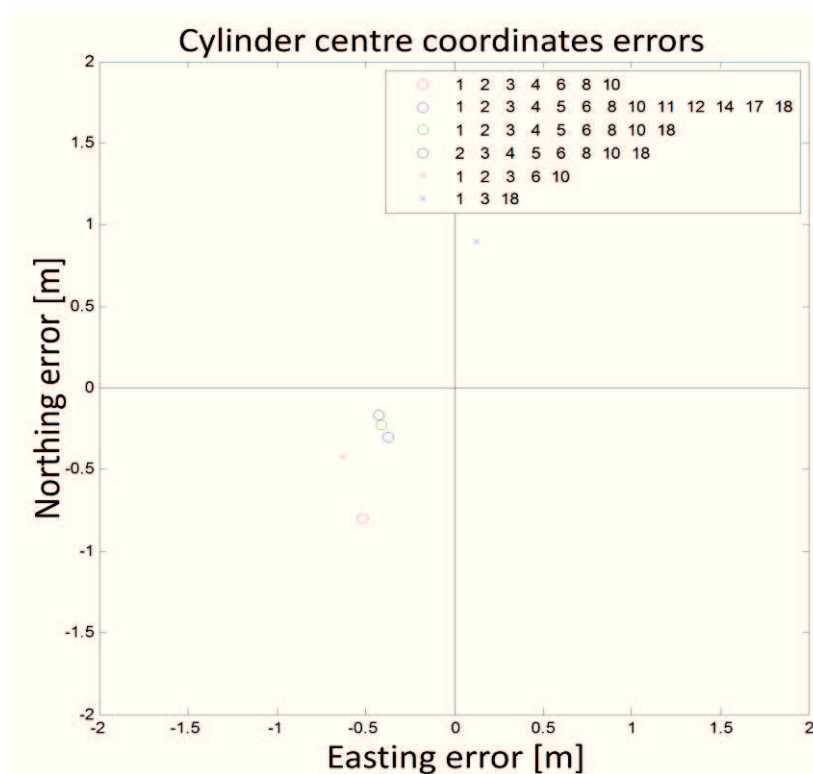


Fig. 101 – The estimated position of the cylinder virtual centre “point C”

4.2.4 DISCUSSION & POSSIBLE IMPROVEMENTS

The analysis performed with the proposed test case confirms the validity of the proposed approach. In particular, the “Naples” test case shows that:

- “feature based pGCPs” are applicable for calibration purposes; as expected, cylinder poles are easily detectable and exploitable, as well as every feature or object with a geometry easily modelled with the circular geometry;

- the following accuracies were achieved:
 - 1/5 of pixel for the diameter estimation;
 - 1/5 of pixel for the relative location accuracy of the base circle centre;
 - absolute location accuracy of the base circle centre of the same order of magnitude of the certified absolute geolocation accuracy of COSMO-SkyMed images;
- images with small incidence angles contribute to reach good results in height determination, while for the diameter estimation it is necessary at least 1 image acquired with high incidence angle.

4.3 “PALAZZO REALE” CASE STUDY

4.3.1 AIM OF THE CASE STUDY

The aim of this case study is to:

- experimentally validate, through a qualitative evaluation, the “Hyperboloid space intersection” model proposed in paragraph 3.3.2.2.

4.3.2 TEST SITE AND DATASET

The test site encompass the “Palazzo Reale” of Naples, as shown by Fig. 102.

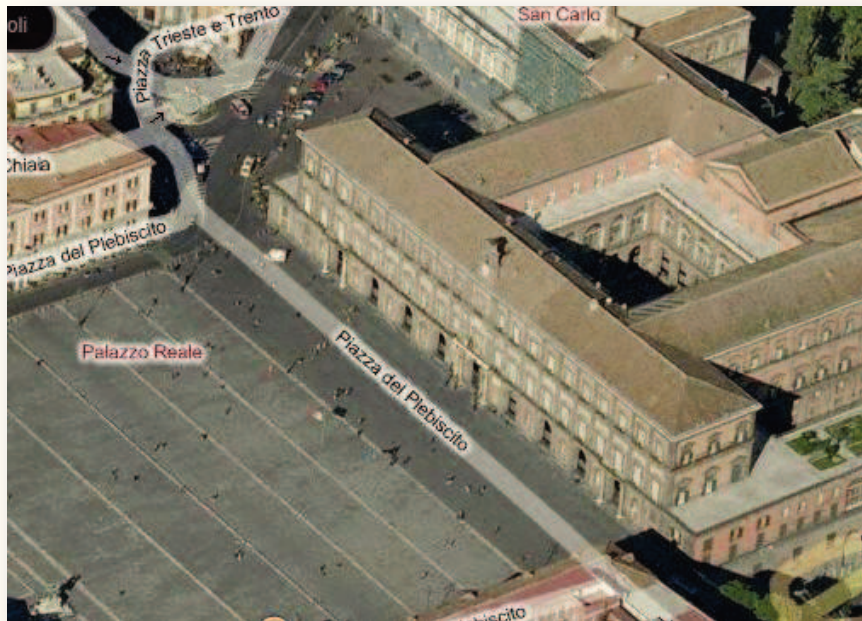


Fig. 102 – Palazzo Reale in Naples

For this case study, Tab. 18 shows the 2 COSMO-SkyMed images that were used, both acquired in the nominal Spotlight 2 mode (COSMO-SkyMed Spotlight Enhanced).

N°	Satellite	Sensor mode	Beam	Pol	Geometry	Date of acquisition
1	COSMO-2	Spotlight 2	S2_08	HH	RA	2011/08/29 04:50:34
2	COSMO-3	Spotlight 2	S2_22	HH	RA	2011/08/04 05:02:51

Tab. 18 – Dataset of CSK images for the “Palazzo Reale” test case

4.3.2.1 Ground truth

The ground truth exploited for this experiment is the 3D model of the “Palazzo Reale” available in Google Earth and displayed in Fig. 103.

Obviously, as the accuracy of this model is not certified, the validation would be only qualitative. The quantitative validation is addressed in paragraph 4.4.



Fig. 103 – The 3D model of Palazzo Reale available in Google Earth

4.3.3 *RESULTS OF HYPERBOLOID SPACE INTERSECTION*

While Fig. 104 shows the correspondence between an optical and a SAR image of the “Palazzo Reale” and Fig. 105 depicts the 3 linear features detected on the first and second image, the results are summarized by Fig. 106 and Fig. 107:

- the plot of the 3 lines, seen from the top, shows the optimal parallelism of the 3 segments; this is a measure of the quality of the reconstruction because the 3 lines correspond to features belonging to the facade of the palace, that must be parallel. The maximum discrepancy is of about 0.75 m, below the geometric resolution of the sensor and corresponding to 0,5% of the length of the palace;
- the 3D plot of the 3 lines inside the Google Earth environment highlights the good correspondence between the 3D features and the 3D model of the palace

available inside Google Earth. In order to make an effective relative comparison between the extracted 3D features and the reference 3D model, the calibration point, instead of being a pGCP created by means of the 2 SAR images, was extracted from Google Earth in correspondence of a streetlamp close to the palace, visible both in the Google Earth image and in the COSMO-SkyMed ones.

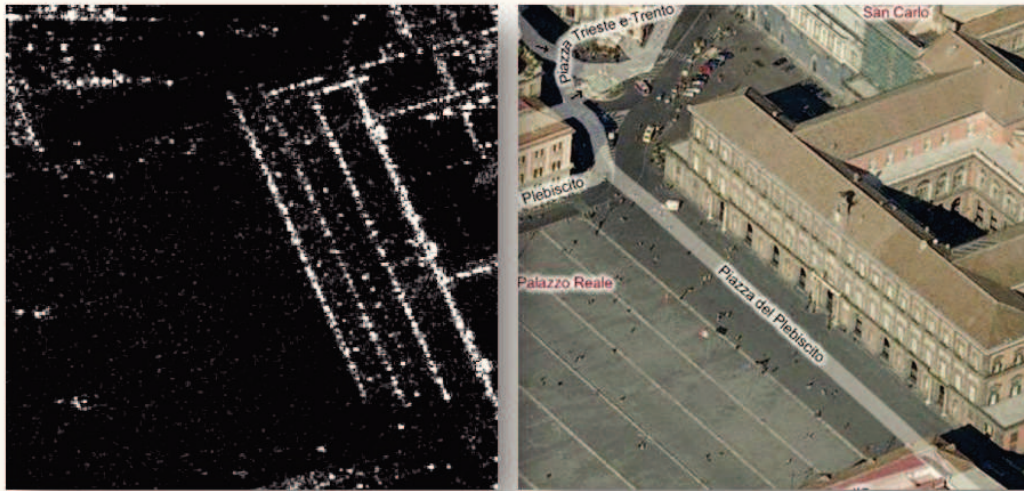


Fig. 104 – Comparison between a SAR and an optical image of “Palazzo Reale”

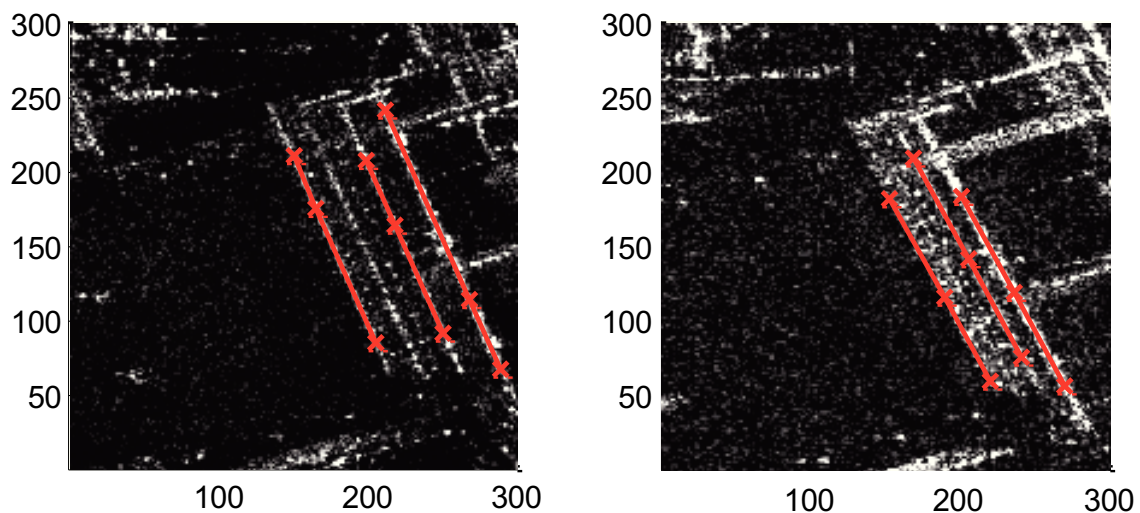


Fig. 105 – 3 lines detected and associated between the 2 images regarding “Palazzo Reale”

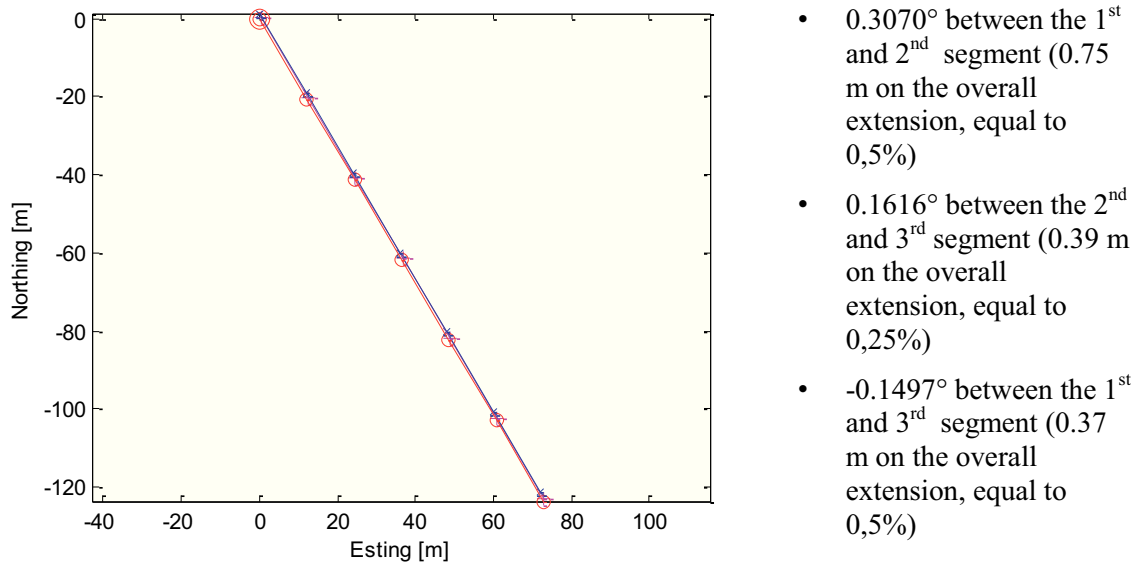


Fig. 106 – Horizontal plot of the 3 lines

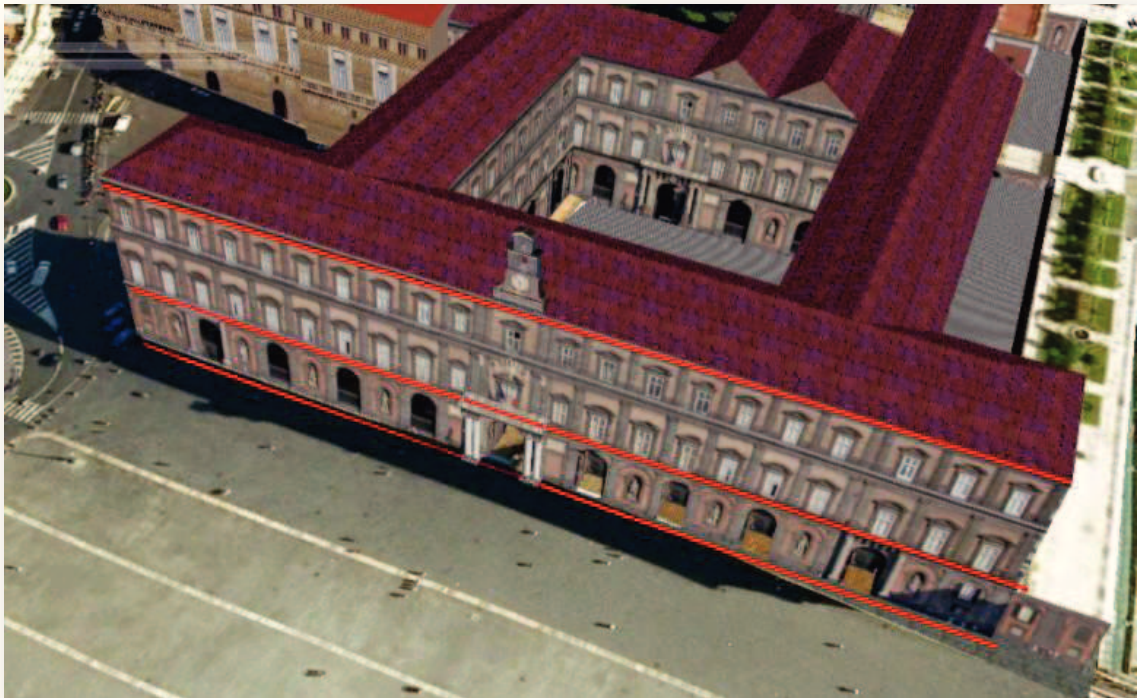


Fig. 107 – A plot of the 3 linear features in the Google Earth® environment

4.3.4 DISCUSSION AND POSSIBLE IMPROVEMENT

This test case shows the possibility to extract 3D linear features employing the “Hyperboloid space intersection”. The matching between the 2 images is based on the detection of different segments (different lengths, different points), thus confirming the possibility not to be obliged to choose corresponding points.

4.4 “BASILICATA” CASE STUDY

4.4.1 AIM OF THE CASE STUDY

The aim of this case study is to:

- experimentally validate, through a quantitative evaluation, the “Hyperboloid space intersection” model proposed in paragraph 3.3.2.2.

4.4.2 TEST SITE AND DATASET

The test site encompasses 4 corner reflectors located in the south of Basilicata, as shown by Fig. 108.



Fig. 108 – The test area in the south of Basilicata

For this case study, Tab. 19 shows the 16 COSMO-SkyMed images that were used, 8 acquired in the nominal Stripmap (COSMO-SkyMed Stripmap Himage) and 8 in the Spotlight 2 mode (COSMO-SkyMed Spotlight Enhanced).

N°	Satellite	Sensor mode	Beam	Pol	Geometry	Date of acquisition
1	COSMO-1	Stripmap	HI_14	HH	RA	2011/03/30 04:51:52
2	COSMO-1	Stripmap	HI_14	VV	RA	2011/01/25 04:52:28
3	COSMO-1	Stripmap	HI_14	VV	RA	2011/02/26 04:52:07
4	COSMO-2	Stripmap	HI_14	VV	RA	2011/01/17 04:52:35
5	COSMO-2	Stripmap	HI_09	VV	RA	2011/02/23 04:46:08
6	COSMO-2	Stripmap	HI_08	HH	RA	2009/08/12 04:52:35
7	COSMO-2	Stripmap	HI_03	HH	RA	2009/07/16 04:46:53
8	COSMO-2	Stripmap	HI_03	HH	RA	2009/09/02 04:46:21
9	COSMO-4	Spotlight 2	S2_33	HH	RA	2010/12/10 05:05:21
10	COSMO-1	Spotlight 2	S2_19	VV	RA	2008/09/13 05:02:14
11	COSMO-3	Spotlight 2	S2_12	HH	RA	2008/11/30 04:55:24
12	COSMO-2	Spotlight 2	S2_12	HH	RA	2008/11/29 04:55:26
13	COSMO-3	Spotlight 2	S2_12	HH	LD	2009/04/16 17:47:45
14	COSMO-2	Spotlight 2	S2_05	VV	RA	2008/07/29 04:50:41
15	COSMO-2	Spotlight 2	S2_05	HH	RA	2009/02/22 04:48:27
16	COSMO-2	Spotlight 2	S2_05	HH	RA	2009/04/27 04:47:48

Tab. 19 – Dataset of CSK images for the “Basilicata” test case

4.4.2.1 Ground truth

The ground truths exploited for this experiment are the geographic coordinates of the ground control points depicted in Fig. 108.

4.4.3 RESULTS OF HYPERBOLOID SPACE INTERSECTION

The available data in the dataset were used for 2 parallel analysis:

- the Stripmap images were exploited to conduct a quantitative analysis of the relative location accuracy;
- the Spotlight images were exploited to conduct a quantitative analysis of the absolute location accuracy.

4.4.3.1 Relative location accuracy assessment

The relative location accuracy was evaluated with the following procedure (reference to Fig. 109), exploiting the 8 Stripmap images in which all the 4 corner reflectors can be detected:

- GCP_1 is the reference point, exploited to perform the geometric calibration;
- GCP_2, GCP_3 e GCP_4 are available as Control Points (CPs);
- the 3 red lines (that do not represent any real feature) are extracted from a series of different couples of images in the hypothesis of one linear feature passing through the measured point scatterers corresponding to the CPs;
- the distances between the CPs and the estimated linear features are evaluated.

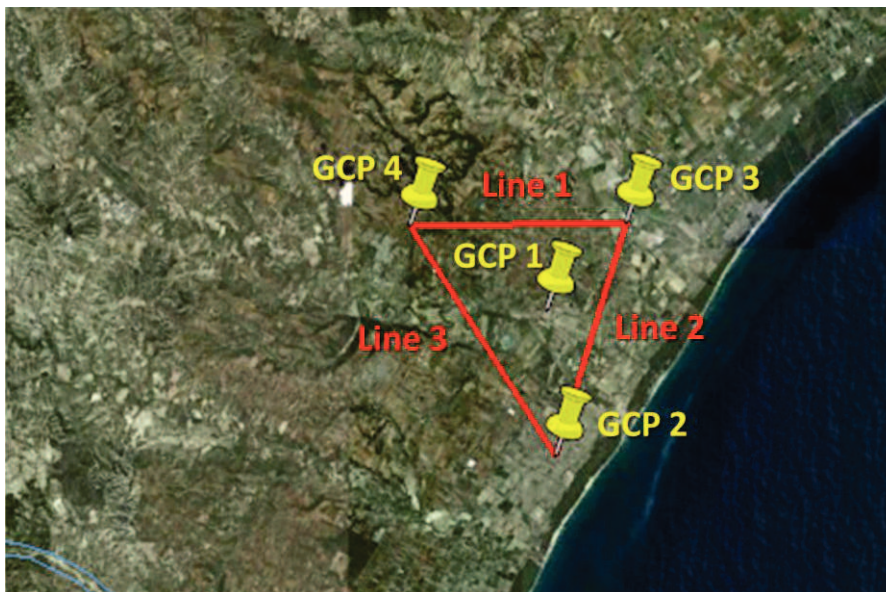


Fig. 109 – Results of the hyperboloid space intersection

CHAPTER 4 - Case studies and Experimental Results

Fig. 110, Fig. 111 and Fig. 112 show the location accuracy figures for the 3 lines, with the different colours aiming at distinguishing between the distances measured with respect to the left or the right Control Point for each line.

Line 2 and line 3 are characterized by very accurate location estimation, while for Line 1 the values are worse than for the other cases due to the non optimal observation conditions: Line 1 is more perpendicular to the flight path (nearly 70°) while line 2 and Line 3 have an azimuth angle minor than 20° . These results are in line with the error budget indication of par. 3.3.2.3, just taking into account that the error budget was developed for a Spotlight sensor mode while the experiment was performed with Stripmap images. In this regard, the performances are really good, largely below the geometric resolution.

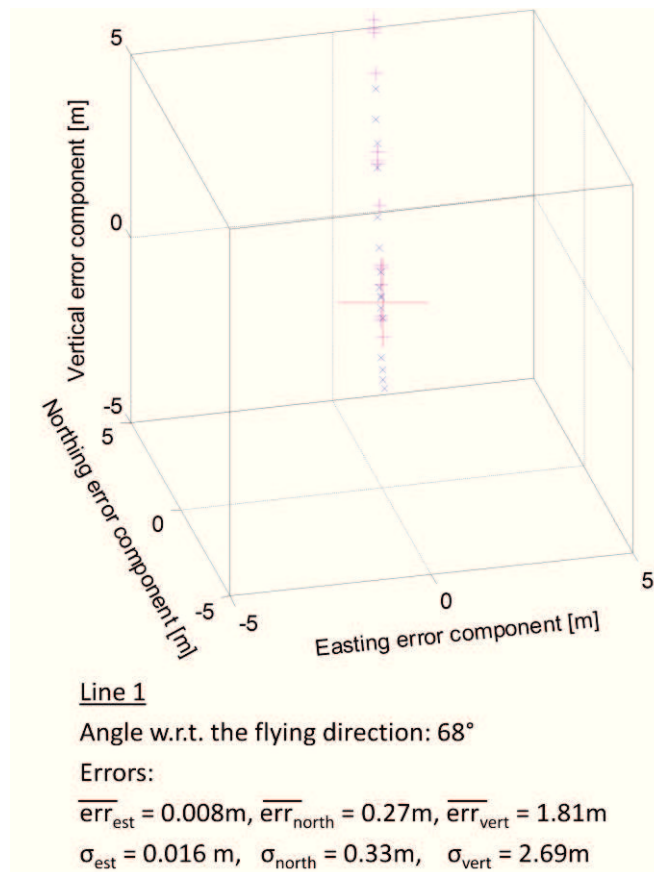


Fig. 110 – Relative accuracy in the estimation of Line 1

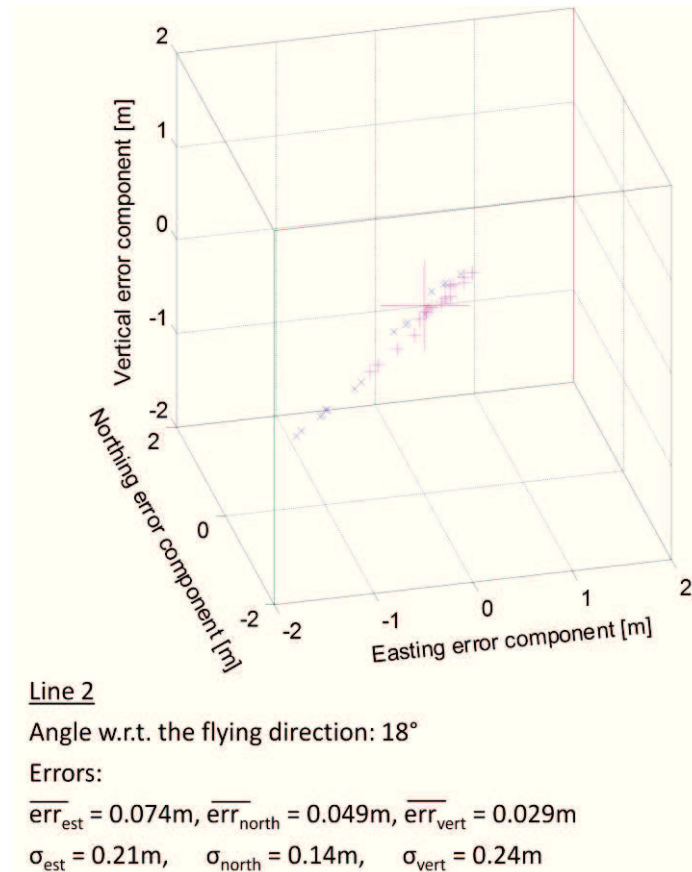


Fig. 111 – Relative accuracy in the estimation of Line 2

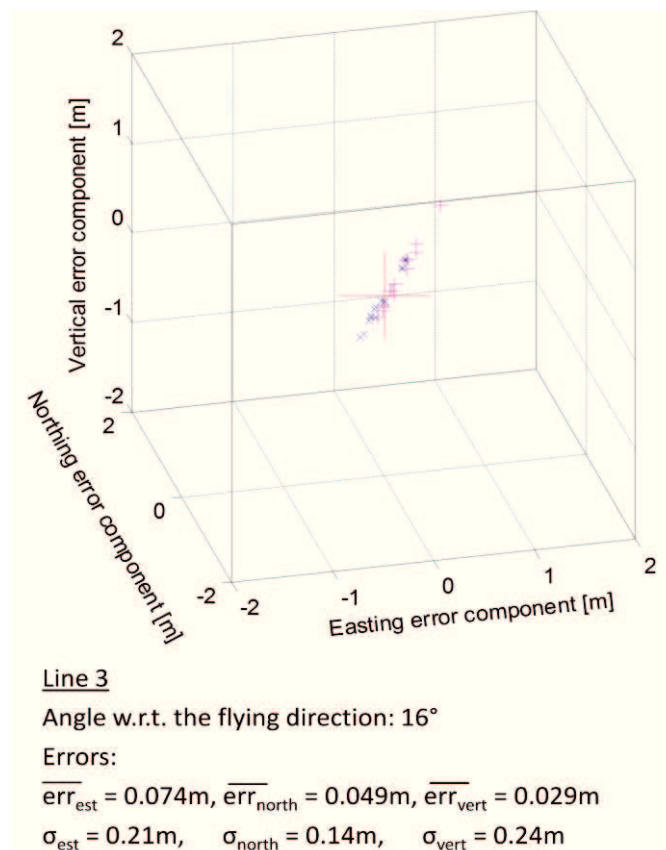


Fig. 112 – Relative accuracy in the estimation of Line 3

4.4.3.2 Absolute location accuracy assessment

The absolute location accuracy was evaluated with the following procedure (reference to Fig. 113), exploiting the 8 Spotlight 2 images in which only 2 corner reflectors can be detected:

- no reference point is selected to perform the geometric calibration;
- GCP 1 & GCP 3 are available as Control Points (CPs);
- the red line (that do not represent any real feature) is extracted from a series of different couples of images in the hypothesis of a linear feature passing through the measured point scatterers corresponding to the CPs;
- the distances between the CPs and the estimated linear features are evaluated.



Fig. 113 – Results of the hyperboloid space intersection

Fig. 114 shows the results obtained with 20 different combinations of the input images. The experienced accuracies are obviously higher than those obtained adopting one calibration point, but perfectly in line with the expected location accuracy of the COSMO-SkyMed images taking into account its certified geolocation error, (57). It is important to highlight that the error budget model was designed taking into account average values deduced from the main operational system, including not only COSMO-SkyMed, but also TerraSAR-X and other SAR systems.

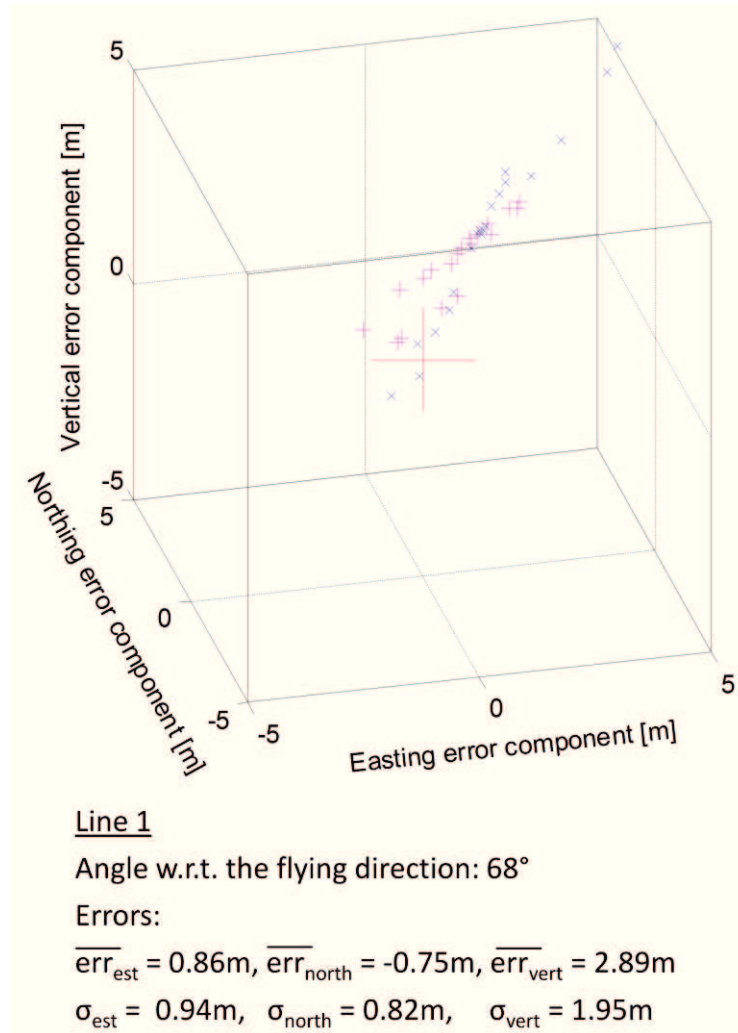


Fig. 114 – Absolute accuracy in the estimation of Line 1

4.4.4 DISCUSSION AND POSSIBLE IMPROVEMENTS

The Hyperboloid Space Intersection proved to be an effective space intersection technique, whose promising results pave the way to new possible applicative developments. This method is able to overcome the difficulties in the matching of linear features, exploiting the feature based approach.

The location accuracy estimations are in good accordance with the outcomes of the numerical simulation devoted to assess the error budget; the final accuracies are comparable to those obtained with the other space intersection techniques in the same matching condition.

Another strength, interesting to be analyzed as a future development, will be the implementation of a multi-image Hyperboloid space intersection, with an approach similar to that one proposed for the circular geometry.

4.5 “MATERA” CASE STUDY

4.5.1 AIM OF THE CASE STUDY

The aim of this test case is to preliminary demonstrate the possible implementation of an automated feature extraction technique based on the multi-aspect space intersection and, in particular, on the Hyperboloid Space Intersection.

4.5.2 TEST SITE AND DATASET

The test site encompasses an industrial building in the surroundings of Matera, in the south of Italy, as depicted in Fig. 115.

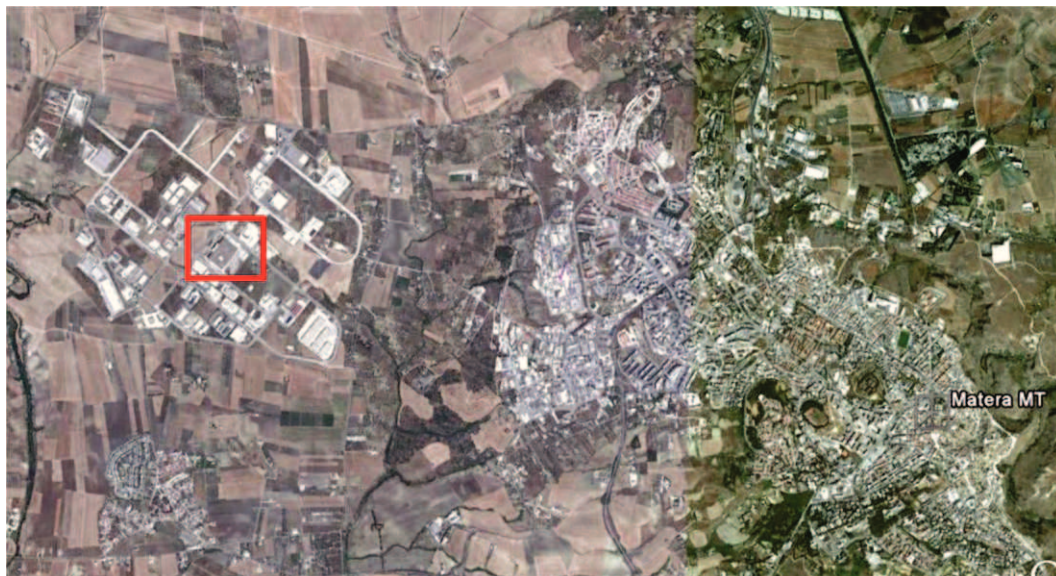


Fig. 115 – A building in the Matera area

For this case study, Tab. 20 shows the 2 COSMO-SkyMed images that were used, both acquired in the nominal Spotlight 2 mode (COSMO-SkyMed Spotlight Enhanced).

N°	Satellite	Sensor mode	Incidence angle	Pol	Geometry	Date of acquisition
1	COSMO-3	Spotlight 2	30°	HH	RD	2009/06/17 17:10:58
2	COSMO-3	Spotlight 2	46°	HH	RD	2009/05/10 16:59:23

Tab. 20 – Dataset of CSK images for the “Matera” test case

4.5.3 RESULTS OF THE AUTOMATIC 3D FEATURE EXTRACTION TECHNIQUE BASED ON MULTIASPECT SPACE INTERSECTION

In the following, the procedure explained at 3.4.2 is applied to the aforementioned dataset and the relevant results are reported.

4.5.3.1 1st and 2nd step

The first step foresees the extraction of the Area of Interest, manually executed.

The aim of the second step is to reduce the speckle fluctuation by means of a speckle filter. In this case, the PPB filter was applied, with the filtering parameters specified in Fig. 116; for deeper details about these parameters refer to (58). These parameters were chosen trying to optimize the detection step. Other filters were applied to the same input images, but the results obtained were less interesting.

Even through visual inspection, the dissimilarity between patches belonging to different surfaces can be appreciated, giving more contrast to transition edges. On the other hand, double bounce scatterings are preserved.

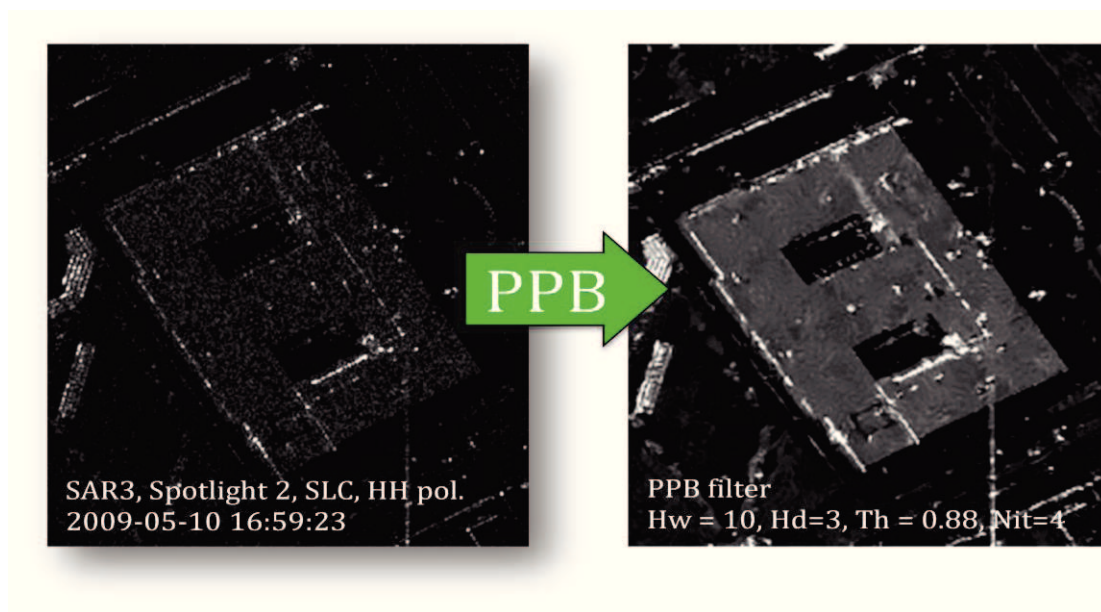


Fig. 116 – Probabilistic Patch Based (PPB) speckle filtering

4.5.3.2 3rd and 4th step

The 3rd step aims at detecting the linear edges in the two input images. For this task, among the detectors introduced in paragraph 3.4.2, the following choice was made:

- a “canny” filter to detect the transition between the target and the shadow areas (green segments of Fig. 117);

- a CFAR edge detector for the dihedral backscattering (red segments of Fig. 117).



Fig. 117 – Edge detection and Hough transform

By means of a visual inspection of the two resulting images, the following considerations arise:

- edges, usually, do not have the same length; therefore it is crucial to exploit a method, such as the “Hyperboloid space intersection”, accepting in inputs different points belonging to the same features;
- there are “broken” edges, that need a post processing in order to be identified as unique features;
- the results are really sensitive to the selection of the filtering parameters;
- the Hough transform performs well in translating the detected edges into oriented segments.

4.5.3.3 5th, 6th and 7th step

The final steps of the extraction procedure firstly require the post-processing of the Hough transformed lines:

- if the edge thinning is not good enough, it could happen that the Hough transform detects more than one segment; in this case the post-processing has to select the best segment to represent the feature;

- union of collinear and close segments.

Then, the matching between the segments has to be performed. In this work I have followed these criteria for the match:

- similarity of specific properties of the feature (length, orientation, etc.);
- similarity of the mutual relations with the other segments, with a graph-based approach (match of segments which have similar graph).

Finally, the space intersection problem is solved by means of the “Hyperboloid space intersection”. The results are those displayed in Fig. 118.

In case more than 2 images are available, the match is confirmed or discarded by means of a cross-comparison of the results obtained with different couple of images (or by applying a control on the residual of the space intersection problem).

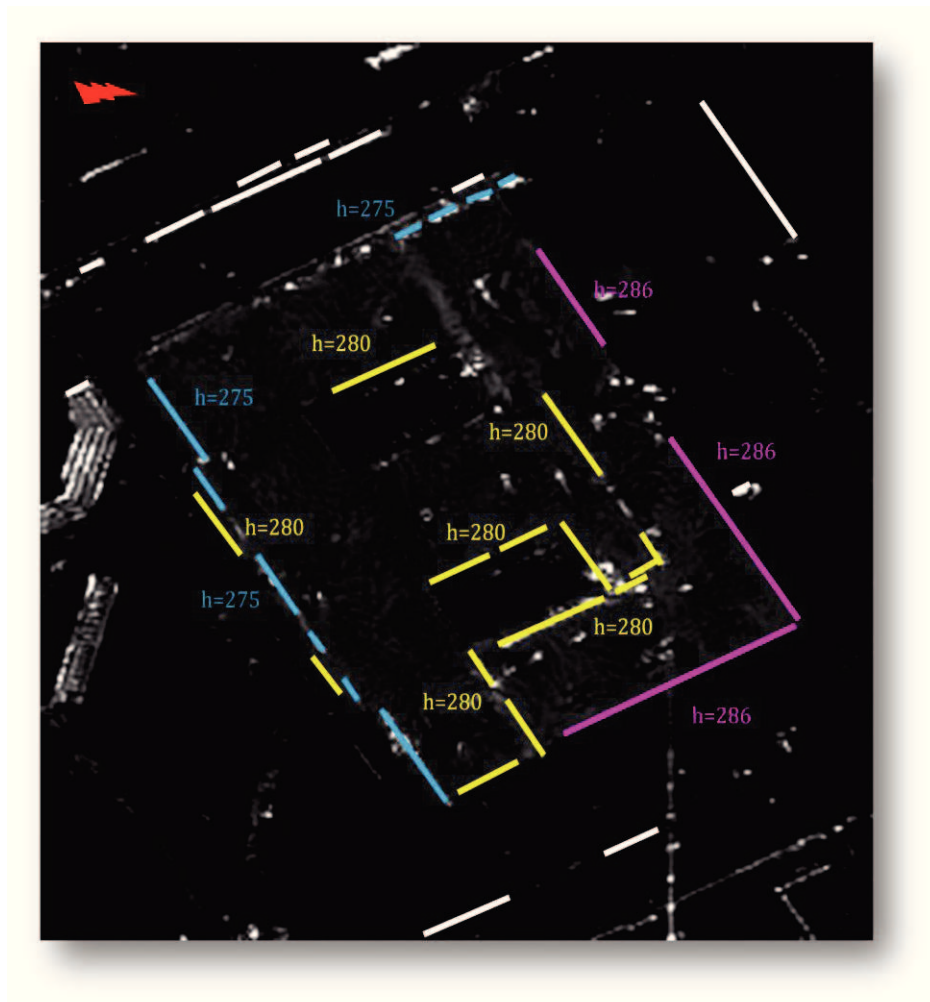


Fig. 118 – Results obtained performing the matching based on Hyperboloid Space Intersection

4.5.4 DISCUSSION & POSSIBLE IMPROVEMENTS

This test case allows to draw the following considerations:

- pre-processing: the PPB despeckle filter gives better results with respect to other filters, such as Frost or Lee; for the future, other filters, e.g. BM3D, could be investigated and compared;
- edge detection: an interesting number of features can be extracted from the input images, even if the number of this features is not enough to allow a complete 3D reconstruction of complex buildings if only based on automated technique; on the other hand, if the edge detection is supervised, these automatic approach strongly enhance the visual interpretation and understanding of the target;
- Hough transform: viable solution to convert raster edge detection mask into 2D segments;
- line post-processing: critical step for the overall automation of the process; the human interpreter performs much better than any unsupervised technique in this step, therefore, at this stage, a supervised review of the results can significantly improve the final accuracies and performances;
- Hyperboloid space intersection: this is the most innovative contribute, because allows to overcome the problem regarding the not exact match of the segments end points. In fact, usually, detected edges corresponding to the same features, as demonstrated by Fig. 117, are one different with respect to the other (one is longer than the other, one is broken into 2 segments, etc);
- space-intersection-based matching feedback: provided that more than 2 input images with different incidence angles are available, it is possible to assess the reliability of the matching by comparing the results obtained combining 2 images per time or measuring the residuals of the n-images space intersection problem.

In conclusion, it is possible to say that this test case demonstrates that SAR images, with the increase of sensor geometric resolution, will become more and more mature for 3D model generation, without any need to exploit other sources of data. On the other hand, a concrete effort will be necessary in order to find robust algorithm to improve the building edges detection, especially in case of acquisition performed from a single viewing aspect.

CHAPTER 5 - PRACTICAL APPLICATIONS AND LESSONS LEARNED

5.1 PRACTICAL APPLICATION OF THE ACHIEVED RESULTS

5.1.1 SUPPORTING IMAGE INTERPRETATION

As stated in the introduction of this thesis, the final aim of this work is to develop new theories in order to enhance the interpretation of SAR images through the improvement of the 3D understanding of the observed SAR scene. According to these principles, this paragraph will show some interesting applicative case studies that will be analyzed by means of the proposed theories and methodologies.

5.1.1.1 Static image interpretation: the case study of the Giza Pyramids

As proposed in this thesis work, pGCP and multi-aspect space intersection can be useful to understand and interpret SAR images. In the following I propose the case of the Great Pyramid of Giza (see Fig. 119). This case was already studied and interpret by means of SAR interferometry, (59), therefore an interesting comparison can be made between the two techniques, analysing the process and the results.



Fig. 119 – The Great Pyramids of Giza



Fig. 120 – The Great Pyramids of Giza in a CSK Stripmap image

From a first glimpse of Fig. 120, the interpretation of the geometric effects seems not easy. In fact an imagery interpreter expects to see the illuminated face of the pyramid affected by the foreshortening or layover effect (depending on the incidence angle), caused by the single bounce backscattering of the aforementioned face, the same effect explained for Fig. 18. Therefore he expects to find the vertex of the Pyramid on the left (the far left point); instead, a second backscattering of the illuminated face seems to be visible “inside the Pyramid”.

Now, I will try to exploit the pGCP generation technique to understand the phenomenology. First of all, it is necessary to collect more than 2 images in which it is possible to identify the same effect.

In this case, 3 CSK images showing the same phenomenology are available in the archive (again it is useful to stress that this technique allows to fully exploit the images already acquired).

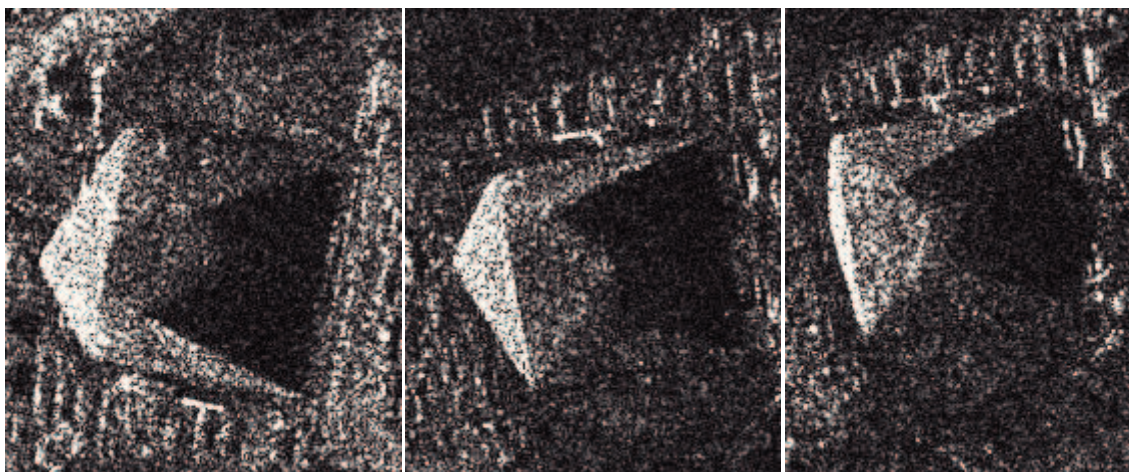


Fig. 121 – 3 CSK Stripmap images available in the CSK archive, acquired with different sensing geometries

Having the necessary dataset, the further step is the identification of the same features or points in the 3 images. As illustrated in Fig. 122, it is possible to recognize:

- the vertex of the “layover” face, which is also the vertex of the other 3 faces (the two lateral faces have a low backscattering while the rear face is in the shadow region), marked with a yellow circle;
- the vertex of the triangle which seems “inside” the Pyramid, marked with a cyan circle.

Fig. 122 shows the generated multi-aspect feature based pGCPs. The locations of these points are validated by comparison with those of the points obtained as intersection of the edges created with the Hyperboloid Space Intersection techniques.

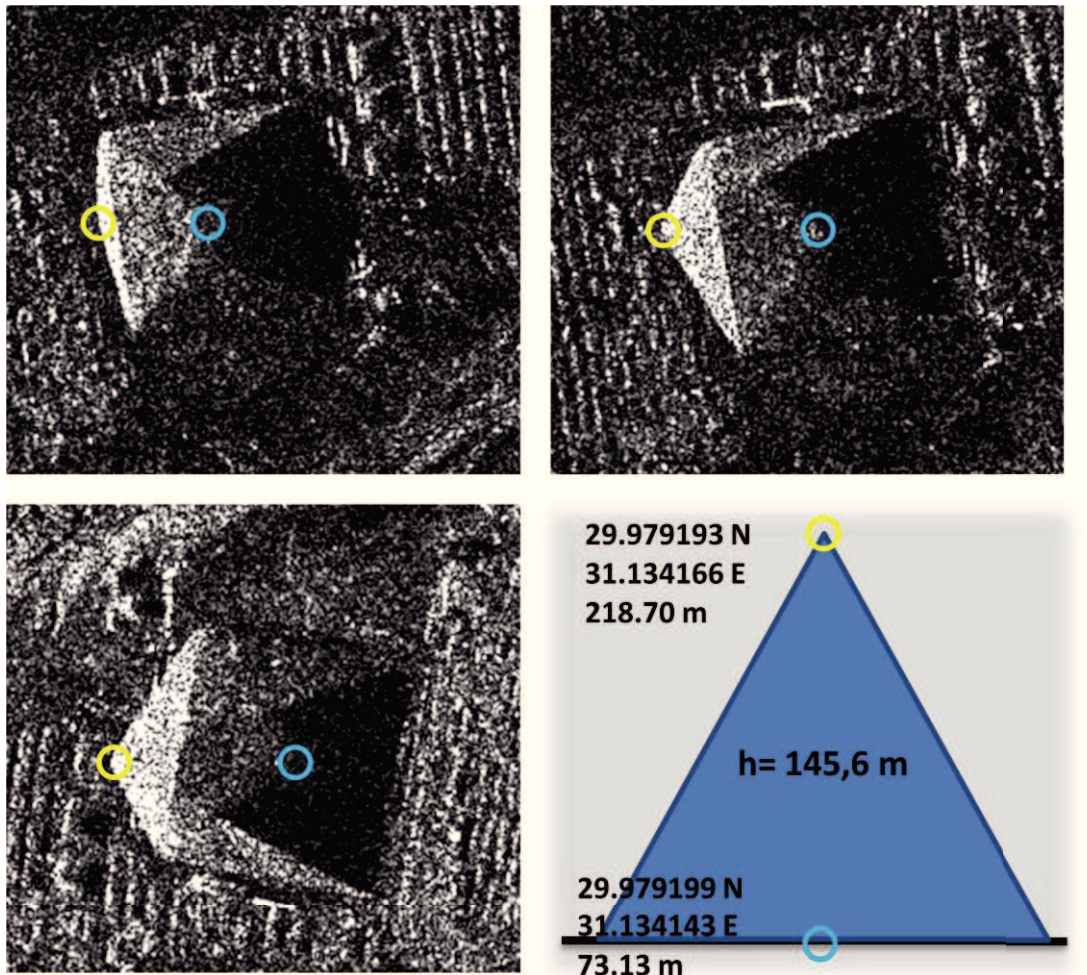


Fig. 122 – Pyramids backscattering interpretation by means of multi-aspect space intersection

The heights reported in Fig. 122 are ellipsoidal heights, relative to WGS84 ellipsoid. Considering that the base of the Great Pyramid is about 73 m w.r.t. the WGS84, it is possible to say that the cyan pGCP is located in correspondence of the base of the Pyramid. On the other hand, the yellow pGCP is about 145 m over the ground, that

would be the nominal height of the Great Pyramid without considering the erosion, that has caused a decrease of the height at 138 m. What does it mean? Referring to the scattering mechanisms summarized in Fig. 30, it is possible to affirm that:

- the yellow pGCP is due to the direct/single bounce scattering in proximity of the vertex of the Pyramid;
- the cyan pGCP is related to a dihedral/double bounce with a dihedral angle composed by a vertical surface close to the vertex of the Pyramid and by the ground.

If we carefully take into account Fig. 119, it is noticeable that the faces of the Great Pyramid are not flat, but are composed by a succession of small steps. Therefore the simplified model of Fig. 123 can be introduced. The cyan path represents the “large double bounce” backscattering mechanism, equivalent to the virtual dotted one: the length equivalence of the two paths explains the existence of a backscattering information in the position marked by the cyan circle. The yellow “local double bounce” path, really close to the single bounce scattering of the ideal flat surface, is responsible for the backscattering characterized by the layover effect.

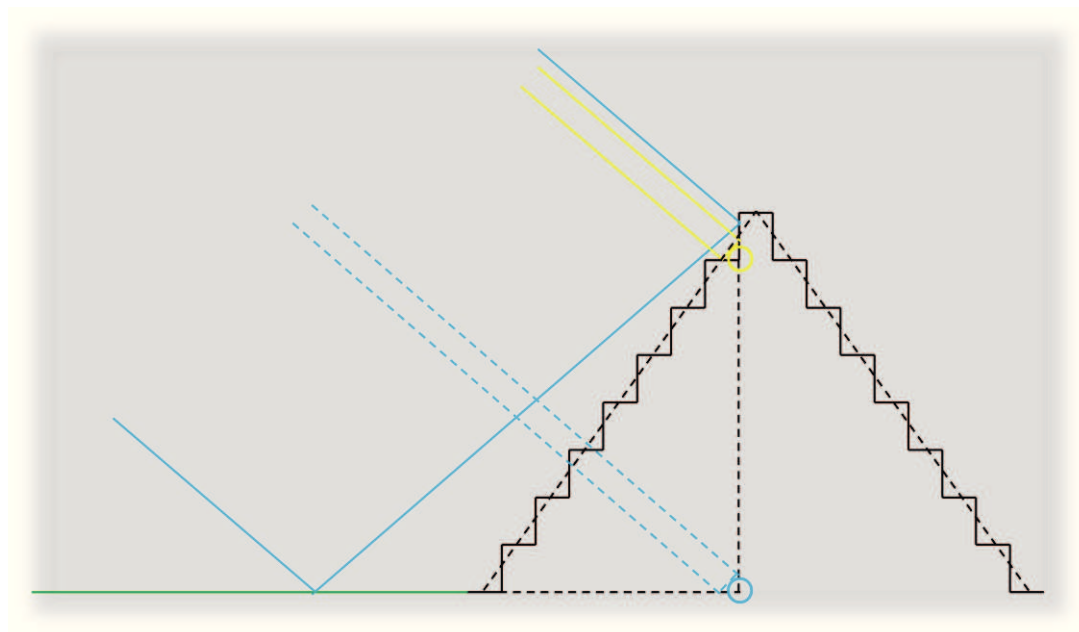


Fig. 123 – Simplified model of the Great Pyramid with the trace of the possible backscattering mechanisms

In conclusion it is possible to state that:

- 2 pGCPs were created in correspondence of two analogues features; the low residuals of the space intersection model applied to the 3 input images confirm the rightness of the association;

- the position of one pGCP inside the Pyramid, at the same height of the base, suggest the existence of a possible double bounce mechanism responsible of such behaviour; the upper pGCP can be easily related to a surface scattering;
- the introduction of a simplified model of the Pyramid, composed by a succession of small steps, confirms that the lower pGCP is caused by a double bounce scattering effect, with a dihedral angle composed by the vertical surface of the last step and the horizontal surface of the ground surrounding the Pyramid. Therefore the direct illuminated side of the pyramid can be seen two times:
 - one brighter backscattering on the left, caused by the layover effect of the “local double bounces” (yellow path of Fig. 123);
 - one weaker return, generated by the “large double bounces” that involves part of the vertical surface of the steps and the surrounding terrain (cyan path of Fig. 123);
- it exists a minimum incidence angle under which the “large double bounce” effect cannot exist. This explains why in Fig. 18 this phenomenon is not visible.

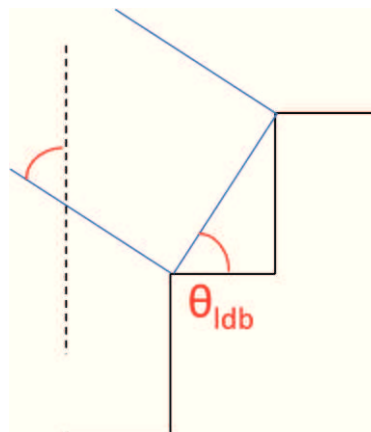


Fig. 124 – Relation between the minimum incidence angle and the steps geometry to have the “large double bounce” backscattering phenomenon

5.1.1.2 Static image interpretation: understanding 3D geometries

Fig. 125 and Fig. 126 show classical examples of SAR image interpretation. If Fig. 126, representing a nice SAR view of the building of the University of Studies of Naples “Federico II” at Piazzale Tecchio, characterized by a clear layover effect, could be not so difficult to interpret, the other is more challenging. Fig. 125, in fact, represents a building very familiar to Air Force Officers who spent a long period of their lives in the Academy: the “Istituti Scientifici”, a building characterized by a circular central body and 2 V shaped wings. The choice not to provide the corresponding optical images is

aimed at creating a case similar to the one in which the analyst is asked to extract intelligence information without any other reference. Obviously, this case would be very rare, possible only if the building is recent and no optical reference images are available. Feeling as an imagery analyst who can only rely on SAR images for the interpretation, it is easier to understand the importance of an instrument able to allow to match, one by one, the corresponding features; in fact, this capability gives an important contribute to the understanding of the 3D shape of the target. From this knowledge, the interpretation begins.

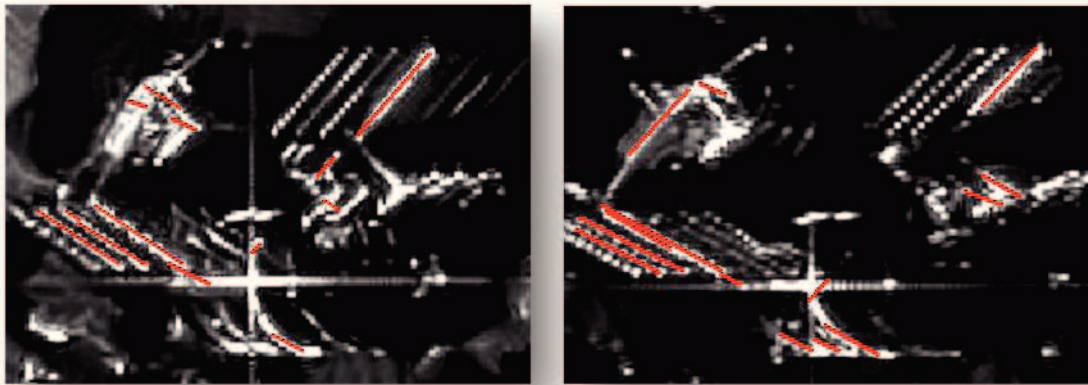


Fig. 125 – The building “Istituti Scientifici” of the Air Force Academy in Pozzuoli

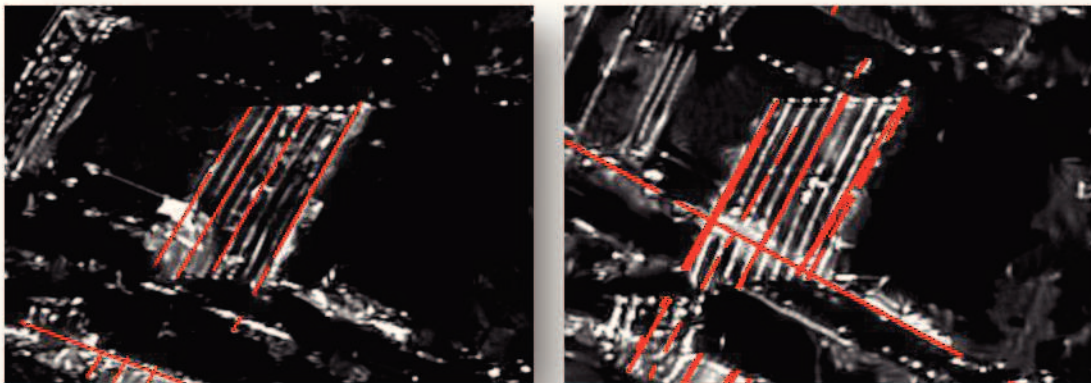


Fig. 126 – The building of the University of Studies of Naples “Federico II” at Piazzale Tecchio

5.1.1.3 Dynamic image interpretation: monitoring the oil content of cylindrical storage tank

The “circular feature based” pGCP and the multi-aspect space intersection for circular geometries are techniques perfectly suitable to monitor the content level of cylindrical tanks devoted to fuel storage.

The schema of Fig. 127 gives an idea of a possible practical implementation:

- first of all, an oil storage facility, characterized by several oil tanks with floating roofs, is modelled by means of multi-aspect space intersection; hence, each tank is catalogued in terms of the central point coordinates and diameter;
- all the information relative to the tanks are stored in a DB;
- an automated software routine, searching the DB, performs a geospatial interrogation of the input images to extract the roofs height;
- a synthesis report is generated over a predetermined period of time.

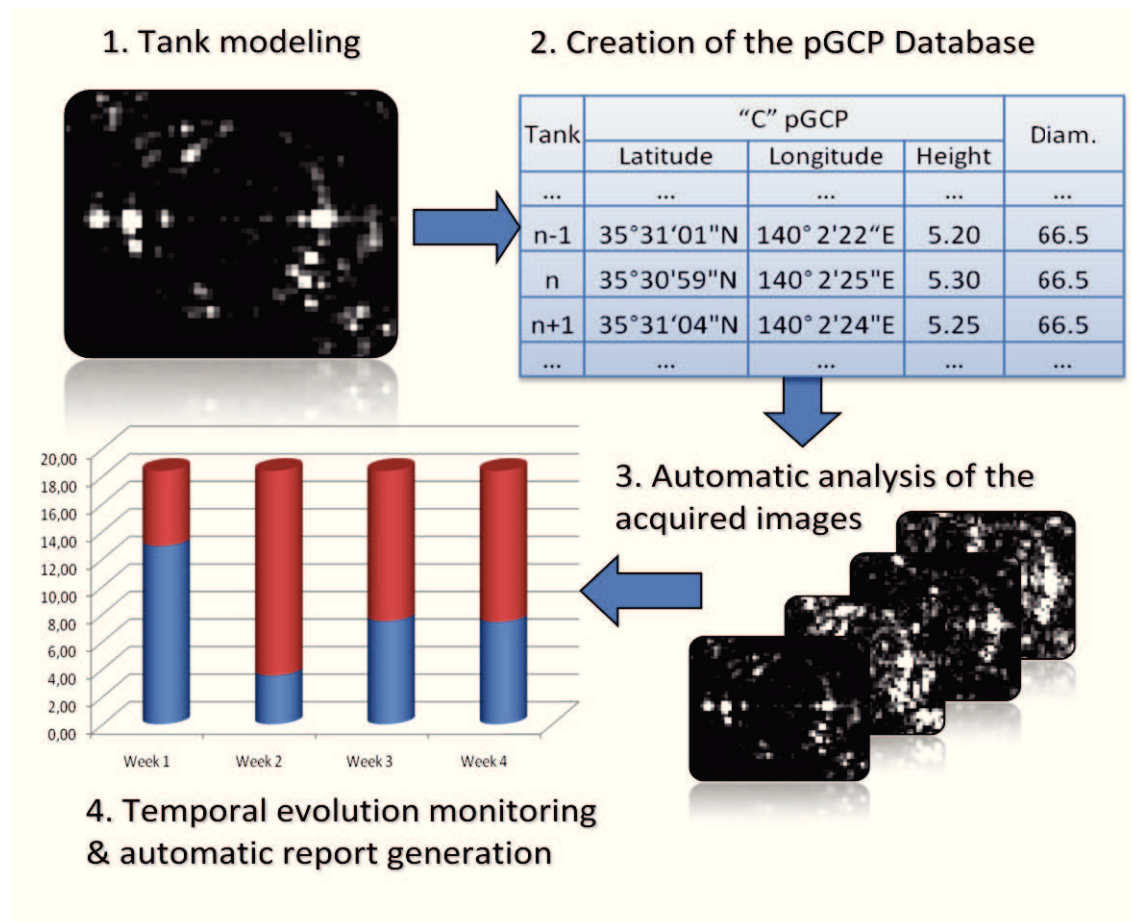


Fig. 127 – Automating the monitoring of an oil storage field

Other references and material about the monitoring of the oil tanks performed with COSMO-SkyMed in this end-to-end approach are available in (60).

5.1.2 CREATING 3D GEOSPATIAL INFORMATION

The pGCP generation is a powerful tool to generate 3D features. These features could represent useful information as they are, or could be further exploited to generate complex objects and information.

5.1.2.1 Replacing GCP with pGCP for electro-optical image precise geolocation

The first and most obvious application of pGCP is the replacement of GCP. As already stated in paragraph 3.3.1.5, pGCP generated adopting the multi-aspect space intersection are:

- robust and characterized by an high accuracy;
- more easily recognizable in electro-optical images.

The second advantage is clearly linked to the concept of “feature based pGCP”. As Fig. 128 shows, the matching, based on the virtual point “C” and the diameter of the base circle, is precise, robust and allows to exploit the high geolocation accuracy of the pGCPs for the registration of the optical data. If the optical image is open source, it is possible to exploit the pGCP for validation purposes (see paragraph 5.1.3).

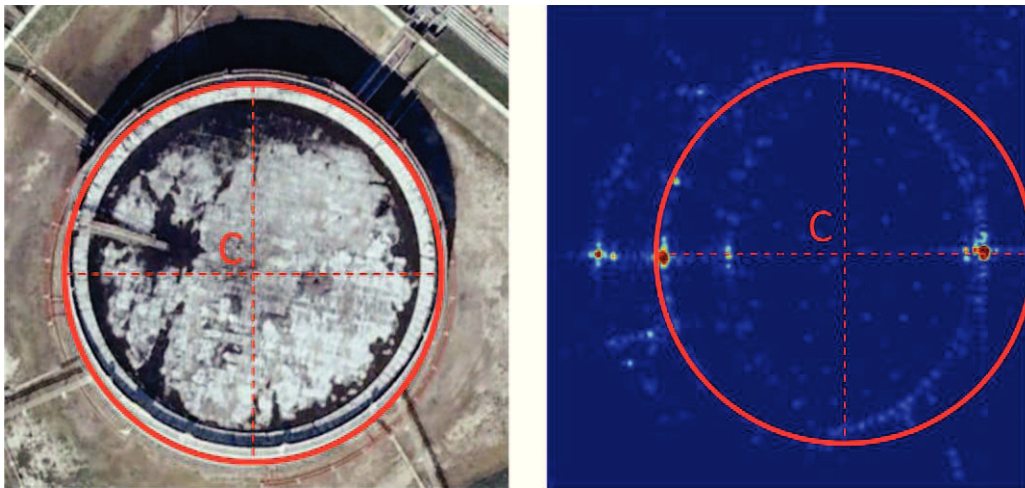


Fig. 128 – Recognizing pGCP both in an optical and in a SAR data (left image: Google Earth©, right image CSK©)

5.1.2.2 3D building extraction

Space intersection techniques and more specifically the “Hyperboloid Space Intersection” are theories perfectly suitable for the generation of 3D information and 3D models. Obviously, while the complete automation of the process needs further researches and investigation, the exploitation of the proposed methods as tools “in the hands” of an imagery interpret is more mature. In this example, the results of a 3D building reconstruction based on Hyperboloid Space Intersection is provided. Fig. 129 shows the results of building 3D interpretation based on the results of 4.5.3.3.

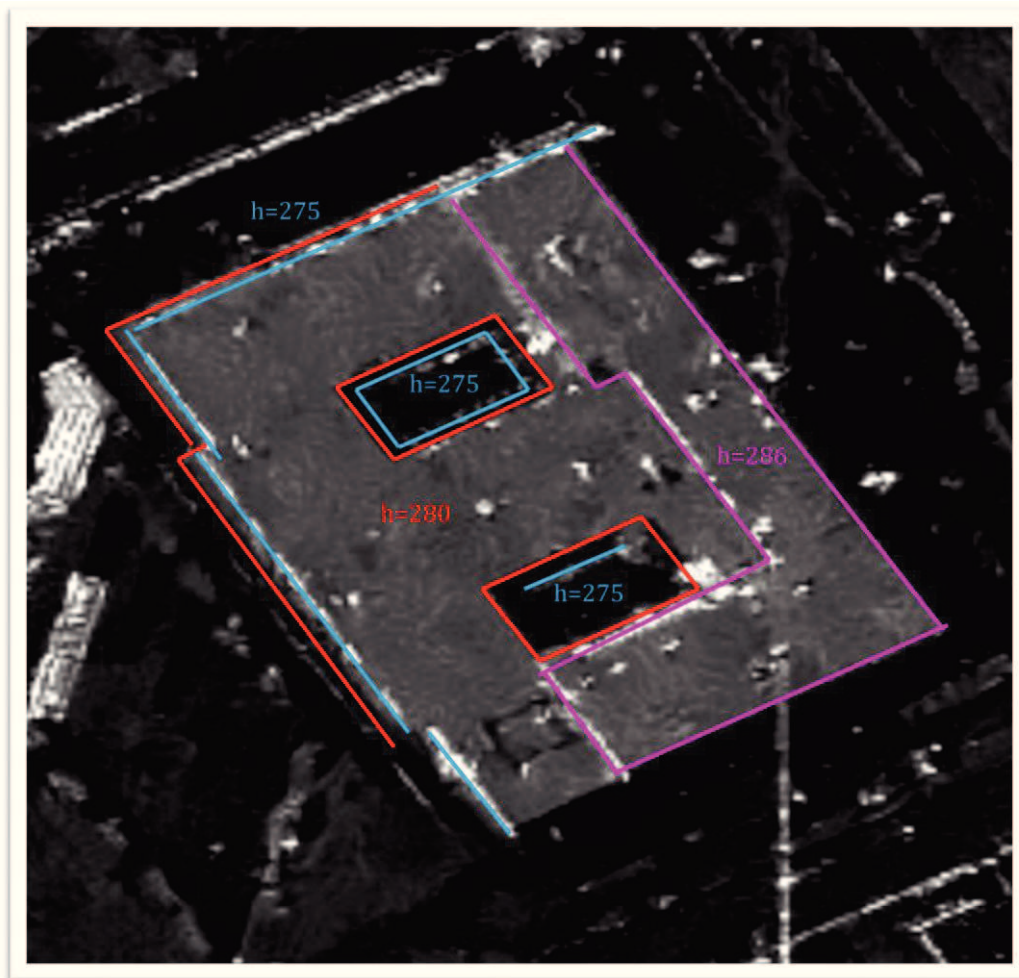


Fig. 129 – 3D interpretation by means of space intersection



Fig. 130 – Validating the 3D interpretation by means of open source ground truth.

The qualitative ground truth data of Fig. 130 confirm the correct understanding of the geometry of the building.

Having compared these results with those of an interpretation of the same building without the 3D information provided by space intersection, the improvement, especially in terms of confidence, is relevant.

5.1.3 *VALIDATING OPEN SOURCE DATA*

SAR systems, as COSMO-SkyMed, have the possibility to acquire a large number of images worldwide, with very short response time. This is important in case of humanitarian relieves and for all the aforementioned military and civilian applications (paragraphs 1.2 and 2.3.3). In certain cases, it is necessary to validate the information provided by the open source image provider in terms of:

- geolocation (measuring the local geolocation accuracy), because sometimes the open source images have geolocation performances far from the average figures;
- image content (correspondence of the open source image content with respect to reality), in order to achieve a strong confidence that the image content has not been modified for unknown purposes;
- information age (if the open source image is not time referenced), that means giving an age to the open source images by means of a comparison with an historical database of SAR images.

All these applications are examples of what it is possible to define, with an open mind, “content fusion” analysis for validation purposes.

5.1.3.1 Validating Google Earth© data

This test case gives a direct and simple example of the validation needs and outcomes. Considering Fig. 131, four historical open Google Earth images are provided, superimposing a pGCP corresponding to the bottom of the external surface. While the first and second images exhibit a good accordance with the pGCP, the two oldest images show big geolocation errors. Therefore, pGCP can give a direct and fast validation. Last but not the least, pGCP can allow to refine the elevation information, that is usually linked to the DEM information available, usually DTED Level 2 or, if not available, Level 1, characterized by vertical accuracies (respectively 30m and 16 m) that are 1 order of magnitude worse than the elevation information it is possible to extract from COSMO-SkyMed data.



Fig. 131 – A series of Google Earth image: validating the geolocation through pGCP

5.1.4 MONITORING TEMPORAL EVOLUTION OF MAN-MADE ACTIVITIES

Space intersection techniques are well suited for the monitoring of building construction or of every kind of phenomenon characterized by a fast increase of the height (for subsidence monitoring, instead, the interferometric techniques are more suitable). During the target construction phase, in fact, acquiring stereo images with the shortest time gap within them (the COSMO-SkyMed system usually allows to acquire a stereo couple or in the morning or in the afternoon window), it is possible to monitor and track the height evolution. The same results cannot be achieved with interferometric techniques, that usually need images acquired with a fixed geometry, usually available in longer time span.

5.2 LESSONS LEARNED

Finishing this work, at the conclusion of three years of research in the domain of SAR data exploitation, I feel I have learnt a large number of lessons. These lessons learned are the outcomes of a theoretical and experimental hard work aiming at developing new theoretical methodologies.

These “lessons learned” are important because they give a roadmap for the future, as they allow not to commit again the same errors and, on the other hand, give the right confidence to find again the same good results you obtained before.



Fig. 132 – Lessons learned, a virtuous approach

First of all, I want to highlights some errors, difficulties, “holes” I have faced in my activities:

- the time wasted in data handing, since the request till the study, is critical. A good initial planning could give better results, but it is absolutely necessary to build a working environment interconnected with the data provider, avoiding data aging and wasting of time;
- radar data and images, as well as COSMO-SkyMed data, are supported by a lot of COTS software; despite this opportunity, rarely these software are provided with user guides for specific source data management (e.g. for CSK, TerraSAR-X, etc), to explain how to use the software in order to manage that kind of data;

CHAPTER 5 - Practical Applications and Lessons Learned

- some important remote sensing systems do not provide open sample images, accessible from internet. That would be useful to make the innovative applications support and manage the data; furthermore, it would increase the cross-check test and comparison between new applications and assessed SW suites;
- some “free routines”, developed in C++, Matlab or IDL programming languages and devoted to basic SAR operations (such as image reading, treating, geocoding, etc.) would be useful in order to ease the development of free applications.

On the other hand, lots of opportunities can be maximized and exploited for the development of applications. Among these:

- the use of open formats, such as the HDF5 format used for the COSMO-SkyMed one, ease the development of new applications;
- the availability of open source software, such as NEST (Next ESA SAR Toolbox), developed by ESA.

5.3 NEEDS FOR NEXT GENERATION SYSTEMS

The results obtained with this thesis and the possible applications based on them give the opportunity to highlight the needs to be fulfilled by future systems. In the following, these needs will be organized with respect to the temporal feasibility.

5.3.1 GOING TOWARDS NEXT GENERATION SYSTEMS

CSG will represent the next generation Italian SAR system; nowadays its development is ongoing. In this regard, the following items, instead of being requirements, are important aspects to be taken into account during the development phase in order to enhance the applicative follow-on:

- resolution improvement: the geometric resolution improvement will enhance the image interpretation, the features extraction step and the capability to perform data fusion with optical data;
- polarimetric acquisition mode: the polarimetric data availability will enhance the feature extraction step;
- single pass stereo data: the platform agility would possibly allow to acquire a stereo couple on the same orbit passage; another possibility would be to perform a bistatic real-time acquisition, having two satellites flying in bistatic configuration (e.g. one CSK and one CSG satellite);
- moving target relocation: multichannel techniques or enhanced processing can support the detection and correct relocation of the moving targets, displaced in the image during the processing phase;
- free sample data: they are required to allow the development of free and innovative applications, especially in the university domain.

5.3.2 NEAR FUTURE GENERATION SYSTEMS

A revolution in SAR images interpretation would be represented by the generation of 3D images. The development of satellite SAR sensors, or constellation of SAR sensors, capable to generate 3D images would represent a remarkable advantage in image interpretation, giving a definitive solution to the layover ambiguity and reducing dramatically the complexity of the analysis.

CONCLUSIONS

This thesis was developed with a specific focus on the necessities regarding SAR image interpretation and 3D object reconstruction. To cope with these needs, it introduces original contributions to extend the potentialities and the field of application of the space intersection theory. These new models can be considered as a “bridge” between the research in the stereo and space intersection domains, mainly carried out for the generation of digital elevation model, and the works regarding the building features extraction.

The main innovations introduced by this work regard:

- the adaptation of the space intersection model to manage multi-aspect views of “circular objects” in order to extract the main features (i.e. 3D location of the centre, diameter) of their circular/cylindrical geometries;
- the introduction of a new space intersection model, called “Hyperboloid Space Intersection”, specifically designed to reconstruct 3D linear segments.

The general benefit of both formulations is that they do not require stereo-viewing nor to find corresponding points within the input images for the matching task; instead, the matching is based on the identification of points belonging to corresponding features, i.e. circular or linear features. Consequently, this approach is more suitable for high resolution SAR images than the other state-of-art space intersection techniques, which do not show significant improvements in accuracy with the increase of geometric resolution. Another clear advantage consists in having the possibility to exploit the full set of available images, without any specific constraint regarding the sensor and the viewing geometries: this is the pre-requisite for the complete exploitation of archive images, usually acquired with non homogeneous viewing geometries and sensor mode.

By introducing the space intersection problem, the scattering behaviour of circular and linear features was deeply analyzed by means of civilian COSMO-SkyMed high resolution images. This phenomenological understanding was translated into geometrical models. For the modelling of circular features, the range-doppler rigorous space intersection model was adapted; on the other hand, for linear features, a completely new space intersection theory was developed, foreseeing the intersection of

CONCLUSIONS

two hyperboloids virtually obtained revolving the target linear feature around the flight paths of the observing SAR sensor.

Models and algorithms accuracy was analyzed in detail by means of numerical simulations carried out with the Montecarlo methodology. The input parameters were opportunely tuned in order to represent the COSMO-SkyMed system performances. By means of an extensive simulation activity, the best geometric configurations were identified, as well as the methodology to be followed in order to select the best combination of input images, in case a large dataset of historical images is already available on the area of interest.

A practical implementation scheme, useful to conduct experimental analysis and to develop operational algorithms and software, was conceived. This schema takes into account, at the same time, the current need to provide the analyst with a useful procedure to understand the 3D scattering mechanisms and the future requirement to automate the process.

An extensive experimental campaign was performed exploiting civilian, not-classified, SAR images of the COSMO-SkyMed system acquired over several test sites in Italy. Both the aforementioned techniques were validated by experimental campaigns. The proposed approaches were demonstrated to hold a dramatic improvement in location accuracy of the extracted features with respect to state-of-art techniques. The experimental analysis were carried out working with high and medium resolution images (respectively 1 and 3 meters of geometric resolution). The relative location accuracy of the extracted features was proved to be below the pixel resolution of the input images in case of strong dihedral returns. On the other hand, experimental results show that the absolute location accuracy is in line with the systems geolocation accuracy.

One of the possible direct follow-on of the multi-aspect space intersection technique applied to circular features is the possibility to generate “circular feature-based pseudo Ground Control Point (pGCP)”. Cylindrical objects, such as utility poles, are detected within a set of multi-aspect images and exploited for the generation of pGCPs. These ones can be used for the registration of a set of SAR/optical images as well as for all the other known applications of GCP.

The Hyperboloid Space Intersection shows the most interesting opportunities; it has the potentiality to represent a suitable theory for the high resolution 3D reconstruction of

CONCLUSIONS

buildings and man-made objects. It synthesizes the advantage of the space intersection theory and of the features extraction techniques. Furthermore, the performance of this approach increases with improved geometric resolutions. Next improvements of this formulation will be the implementation of a multi-image approach, similar to the one proposed for circular geometries, and its integration in a full multi-sensor space intersection method.

Future developments will regard the automation of the 3D reconstruction problem and the integration and combination of the proposed approaches in order to describe complex objects.

Last but not the least, this work has tried to translate the proposed theories and algorithms into accessible and useful tools for the Defence users. With respect to the needs of SAR imagery analysts, an approach to improve and ease the understanding of the scattering mechanism has been proposed. As shown for the test case of the pyramids, important evidences about the scattering behaviour can be obtained exploiting the space intersection methods. Other possible applications enabled by the new formulations are:

- pGCP generation for image registration and data fusion;
- 3D building interpretation and reconstruction;
- 3D features extraction and geospatial information generation;
- validation of open source information and 3D models.

BIBLIOGRAPHY

1. *State-of-the-art of elevation extraction from satellite SAR data*. **Toutin, T and Gray, L.** 2000, ISPRS Journal of Photogrammetry & Remote Sensing , Vol. 55, pp. 13–33.
2. **Leberl, F.** *Radargrammetric image processing*. s.l. : Artech House, 1990.
3. *Opposite side ERS-1 SAR stereo mapping over rolling topography*. **Toutin, T.** 2, 1996, IEEE Transactions on Geoscience and Remote Sensing, Vol. 34, pp. 543 - 549.
4. *Rectangular building extraction from stereoscopic airborne radar images*. **Simonetto, E., Oriot, H. and Garello, R.** 2005, IEEE Transactions on Geoscience and Remote Sensing , Vol. 43, pp. 2386-2395.
5. *Automatic Reconstruction of Building Objects From Multiaspect Meter-Resolution SAR Images*. **Xu, Feng and Jin, Ya-Qiu.** 7 - Part 2, 2007, IEEE Transactions on Geoscience and Remote Sensing, Vol. 45, pp. 2336 - 2353.
6. **ERDAS.** Radar Mapping Suite - Product literature. *www.erdas.com*. [Online] [Cited: 16 10 2011.] <http://www.erdas.com/products/erdasimagine/imagineradarmappingsuite/ProductLiterature.aspx>.
7. **ITT Visual Information Solutions.** SARscape modules for ENVI. <http://www.itvis.com>. [Online] [Cited: 16 10 2011.] http://www.itvis.com/portals/0/pdfs/envi/ENVI_SARscape_Brochure.pdf.
8. **BAE.** SOCET GXP - Geospatial Analysis Capabilities. *socet-gxp-geospatial-analysis-capabilities*. [Online] [Cited: 16 10 2011.] <http://www.socetgxp.com/content/products/socet-gxp/socet-gxp-key-capabilities/socet-gxp-geospatial-analysis-capabilities>.
9. **Array.** Next ESA SAR Toolbox. <http://nest.array.ca>. [Online] [Cited: 16 10 2011.] <http://nest.array.ca/web/nest>.
10. —. GEOINT SAR Toolbox. <http://nest.array.ca>. [Online] [Cited: 16 10 2011.] <http://nest.array.ca/web/array/geoint>.
11. **GAMMA.** <http://www.gamma-rs.ch>. *GAMMA Software*. [Online] [Cited: 16 10 2011.] http://www.gamma-rs.ch/uploads/media/gamma_soft_08.pdf.

BIBLIOGRAPHY

12. **Lillesand, T. M. and Kiefer, R. W.** *Remote Sensing and Image Interpretation*. s.l. : John Wiley and Sons, Inc., 1979.
13. **Curlander, J.C. and McDonough, R.N.** *Synthetic Aperture Radar, Systems and Signal Processing*. s.l. : Wiley Interscience, 1991.
14. **Sarmap**. The SAR guide-book. [Online] September 2008. [Cited: 20 May 2009.]
15. *A study of the RPC model of TerraSAR-X and COSMO-SkyMed SAR imagery*. **Guo Zhang, Xiaoyong Zhu**. Beijing : s.n., 2008, The International Archives Of The Photogrammetry, Remote Sensing And Spatial Information Sciences, Vol. XXXVII. Part B1.
16. **H.J. Buiten, J.G.P.W. Clevers**. Land observation by remote sensing: theory and applications. *Gordon and breach science publishers*. 1993.
17. **Natural Canada Centre for Remote Sensing**. Fundamentals of remote sensing.
18. **Italian Space Agency**. COSMO-SkyMed System Description and User Guide.
19. —. COSMO-SkyMed SAR Product Handbook.
20. **e-GEOS**. e-GEOS Applications. <http://www.e-geos.it>. [Online] [Cited: 05 11 2011.] <http://www.e-geos.it>. <http://www.e-geos.it/applications/applications.html>.
21. —. Rapid Mapping Service for Haiti Earthquake - Free downloadable Data and Products. <http://spatial.telespazio.it>. [Online] [Cited: 05 11 2011.] http://spatial.telespazio.it/gmosaic_haiti/.
22. *COSMO-SkyMed Second Generation Satellite Challenges: Paylooad, Data Handling, Attitude Control*. **Scorzafava, E, et al**. Palermo : s.n., 2011. Proceeding of 17th Ka-Band Conference.
23. *Synthetic interferometer radar for topographic mapping*. **Graham, L. C.** June 1974, Proc. IEEE, Vol. 62, pp. 763–768.
24. *Accuracy of topographic maps derived from ERS-1 interferometric radar*. **Zebker, H. A., et al**. July 1994, IEEE Transactions on Geoscience and Remote Sensing, Vol. 32, pp. 823–836.
25. *DEM Generation by Means of ERS Tandem Data*. **Rufino, Giancarlo, Moccia, Antonio and Esposito, Salvatore**. 6, November 1998, IEEE Transactions on Geoscience and Remote Sensing, Vol. 36, pp. 1905-1912.

BIBLIOGRAPHY

26. *Performance of the Shuttle Radar Topography Mission, X-band radar system.* **Werner, M., Klein, K.-B. and Haeusler, M.** 2000. Proceedings of IEEE Geoscience and Remote Sensing Symposium. Vol. 6, pp. 2590 – 2592.
27. *Quantitative analysis of stripmap and spotlight SAR interferometry with COSMO-SkyMed constellation.* **Nitti, D.O., et al.** Proceedings of 2009 IEEE Geoscience and Remote Sensing Symposium. Vol. 2, pp. II-925 - II-928.
28. *COSMO-SkyMed constellation configurations: current status and possible evolutions.* **Caltagirone, F., et al.** Palermo : s.n., 2011. Proceeding of 17th Ka-Band Conference.
29. *TanDEM-X: A Satellite Formation for High-Resolution SAR Interferometry.* **Krieger, G., et al.** 2007. Geoscience and Remote Sensing, IEEE Transactions on. Vol. 45, pp. 3317 - 3341.
30. *High-Accuracy Urban DEM Using Permanent Scatterers.* **Perissin, Daniele and Rocca, Fabio.** 11, November 2006, IEEE Transactions on Geoscience and Remote Sensing, Vol. 44, pp. 3338-3347.
31. *From the expected scientific applications to the functional specifications, products and performance of the SABRINA missions.* **Renga, A., et al.** 2008. Proceedings of 2008 Radar Conference. pp. 1 - 6 .
32. *Imaging geodesy with TerraSAR-X.* **Eineder, M., et al.** 25-30 July 2010. Geoscience and Remote Sensing Symposium (IGARSS), 2010 IEEE International. pp. 4827-4830.
33. *Building Recognition From Multi-Aspect High-Resolution InSAR Data in Urban Areas.* **Thiele, A., et al.** 2007, IEEE Transactions on Geoscience and Remote Sensing, Vol. 45, pp. 3583-3593.
34. *Spatiotriangulation with multisensor VIR/SAR images.* **Toutin, T.** 10, October 2004, IEEE Transactions on Geoscience and Remote Sensing, Vol. 42, pp. 2096-2103.
35. *Three-dimensional focusing with multipass SAR data.* **Fornaro, G., Serafino, F. and Soldovieri, F.** 3, 2003, IEEE Transactions on Geoscience and Remote Sensing, Vol. 41, pp. 507 - 517.

BIBLIOGRAPHY

36. *Three-dimensional multipass SAR focusing: experiments with long-term spaceborne data.* **Fornaro, G., Lombardini, F. and Serafino, F.** 4, 2005, IEEE Transactions on Geoscience and Remote Sensing, Vol. 43, pp. 702 - 714.
37. **Schreier, G.** *SAR Geocoding.* s.l. : Wichmann, 1993.
38. *A weighted Least Squares Solution for Space Intersection of Spaceborne Stereo SAR Dara.* **Chen, Pu-Huai and Dowman, Ian J.** 2, 2001, IEEE Transaction on Geoscience and Remote Sensing, Vol. 39.
39. *Application of radar space triangulation to the calibration of interferometric DEM.* **Belgued, Y., et al.** 1998. Geoscience and Remote Sensing Symposium Proceedings. Vol. 5, pp. 2665-2667.
40. *"Nonlinear Least-Squares" State of the Art in Numerical Analysis.* **Dennis, J.E.** [ed.] D. Jacobs. s.l. : Academic Press, 1977, pp. 269-312.
41. *Geometric precision in space radar imaging: results from TerraSAR-X.* **Ager, T. P. and Bresnahan, P.C.** Baltimore, Maryland : s.n., 2009. ASPRS 2009 Annual Conference.
42. *TerraSAR-X Precise Trajectory Estimation and Quality Assessment.* **Yoon, Y.T., et al.** 6, June 2009, IEEE Transactions on Geoscience and Remote Sensing, Vol. 47, pp. 1859-1868.
43. **Bresnahan, P. C.** Geolocation Accuracy Re-Evaluation of COSMO-SkyMed Spotlight and Stripmap imaging modes products. <http://calval.cr.usgs.gov/>. [Online] 31 March 2011. [Cited: 24 August 2011.] http://calval.cr.usgs.gov/JACIE_files/JACIE11/Presentations/ThurPM/300_Bresnahan_JACIE_11.006.pdf.
44. —. Absolute Geolocation Accuracy Evaluation of TerraSAR-X-1 Spotlight and Stripmap Imagery – Study Results. <http://calval.cr.usgs.gov/>. [Online] 2 April 2009. [Cited: 20 September 2011.] http://calval.cr.usgs.gov/JACIE_files/JACIE09/ThursPM/BresnahanNGACCAPTSX1.pdf.
45. *Building feature extraction via a deterministic approach: application to real high resolution SAR images.* **Franceschetti, G., et al.** 23-28 July 2007. IEEE International Geoscience and Remote Sensing Symposium. pp. 2681-2684.

BIBLIOGRAPHY

46. *Building extraction and 3D reconstruction in urban areas from high-resolution optical and SAR imagery.* **Sportouche, H., Tupin, F. and Denise, L.** Shangai : s.n., 20-22 May 2009. Urban Remote Sensing Event, 2009 Joint. pp. 1-11.
47. *Radargrammetric Extraction of Building Features from High Resolution Multi-aspect SAR Data.* **Soergel, U., et al.** 2006. IEEE International Conference on Geoscience and Remote Sensing Symposium. pp. 3635-3638.
48. *Radargrammetric processing for 3-D building extraction from high-resolution airborne SAR data.* **Simonetto, E., et al.** 2003. IEEE International Geoscience and Remote Sensing Symposium . Vol. 3, pp. 2002- 2004.
49. *The extraction of Building Dimensions from High Resolution SAR imagery.* **Bennet, A.J. and Blacknell, D.** 2003. Proceedings of the International Radar Conference.
50. *Assessment of TerraSAR-X Products with a New Feature Extraction Application: Monitoring of Cylindrical Tanks.* **Guida, R., Iodice, A. and Riccio, D.** February 2010, IEEE Transactions on Geoscience and Remote Sensing, pp. 930-938.
51. *A Computational Approach to Edge Detection.* **Canny, J.** 6, 1986, IEEE Transactions on Pattern Analysis and Machine Intelligence, Vols. PAMI-8, pp. 679-698.
52. *Digital Image Enhancement and Noise Filtering by Use of Local Statistics.* **Lee, J. S.** 2, March 1980, IEEE Transactions on Pattern Analysis and Machine Intelligence, Vols. PAMI-2, pp. 165-168.
53. *A model for radar images and its application to adaptive digital filtering of multiplicative noise.* **Frost, V.S., et al.** 1982 , IEEE Transactions on Pattern Analysis and Machine Intelligence, Vol. 4, pp. 157-166.
54. *Image denoising by sparse 3D transform domain collaborative filtering.* **Dabov, K., et al.** 8, August 2007, IEEE Transaction on Image Processing, Vol. 16.
55. *Iterative Weighted Maximum Likelihood Denoising with Probabilistic Patch-Based Weights.* **Deledalle, C.A., Denis, L. and Tupin, F.** 12, December 2009, IEEE Transaction on Image Processing, Vol. 18.
56. *Bright line detection in COSMO-SkyMed SAR images of urban areas.* **Brett, P.T.B. and Guida, R.** 11-13 April 2011. 2011 Joint Urban Remote Sensing Event (JURSE). pp. 253-256.

BIBLIOGRAPHY

57. **Bresnahan, P. C.** Absolute geolocation accuracy evaluation of COSMO-SkyMed Spotlight and Stripmap Imagery - Study results. *http://calval.cr.usgs.gov/*. [Online] 2 April 2009. [Cited: 24 August 2011.] *http://www.google.it/url?sa=t&source=web&cd=2&ved=0CCIQFjAB&url=http%3A%2F%2Fcalval.cr.usgs.gov%2FJACIE_files%2FJACIE09%2FThursPM%2FBresnahanNGACCAPCSM.pdf&ei=6VtVTrPxHYeYOoS0gJsG&usg=AFQjCNFwzGvd1d6D6wQ573kRfStumCEfrw*.
58. *Effects of compression on SAR image interpretability*. **Greco, A., et al.** Livorno : s.n., 2010. 2010 IEEE GOLD Remote Sensing Conference.
59. *The Pyramids of Gizeh Seen by TerraSAR-X - A Prime Example for Unexpected Scattering Mechanisms in SAR*. **Bamler, R. and Eineder, M.** 3, July 2008, IEEE Geoscience And Remote Sensing Letters, Vol. 5.
60. *Estimation of tanks roofs height by means of single COSMO-SkyMed images*. **Galasso, M., et al.** Livorno : s.n., 2010. 2010 IEEE GOLD Remote Sensing Conference.
61. *The Extraction of Building Dimensions from High Resolution SAR Imagery*. **Bennet, A.J. and Blacknell, D.** 2003. Proceedings of the International Radar Conference 2003. pp. 182-187.
62. **Brunner, D.** Advanced Methods For Building Information Extraction From Very High Resolution SAR Data To Support Emergency Response. *PhD Thesis*. November 2009.
63. *Reconstruction of Man-Made Objects from High Resolution SAR Images*. **Bolter, R.** 2000. 2000 IEEE Aerospace Conference Proceedings. Vol. 3, pp. 287-292.
64. **Lim, J. S.** Two-Dimensional Signal and Image Processing. Englewood Cliffs : Prentice Hall, pp. 478-488.
65. **Spilker, J.** Satellite Constellation and Geometric Dilution of Precision. *Global Positioning System: Theory and Applications*. Washington, D.C. : American Institute of Aeronautics and Astronautics, Inc., 1996, Vol. 1, 5.

Le immagini COSMO-SkyMed presentate in questo lavoro di tesi sono state impiegate nel pieno diritto di utilizzo dell'Amministrazione Difesa, in quanto di proprietà della Difesa o acquisite dall'archivio dell'Agenzia Spaziale Italiana in accordo a quanto stabilito nel documento “Politica nazionale dei dati, prodotti e condivisione delle risorse”, e sono state elaborate presso il Centro Interforze Telerilevamento Satellitare dello Stato Maggiore della Difesa.

Le immagini, i dati e le informazioni pubblicate in questa tesi sono non classificate e non attengono specificamente a know-how acquisito a livello nazionale ovvero ad informazioni che sono di vietata divulgazione ai sensi delle norme vigenti.

The COSMO-SkyMed images presented in this thesis work were used according to the licensing of the Italian Ministry of Defence, since they belong to the Italian Ministry of Defence or they were acquired from the Italian Space Agency archive following the rules stated in the document “*Politica nazionale dei dati, prodotti e condivisione delle risorse*”, and they were treated and elaborated in the *Centro Interforze Telerilevamento Satellitare* premises of the Italian Ministry of Defence.

The images, information and data published in this thesis are not classified and do not regard any specific national know-how nor information that cannot be divulged in accordance to the applicable laws.